Magnetic Circular Dichroism in the Transmission Electron Microscope

dott. **Stefano Rubino**
Institute for Solid State Physics,
Vienna University of Technology,
A-1040 Vienna, Austria
email: stefanorubino@yahoo.it

December 16^{th}, 2007

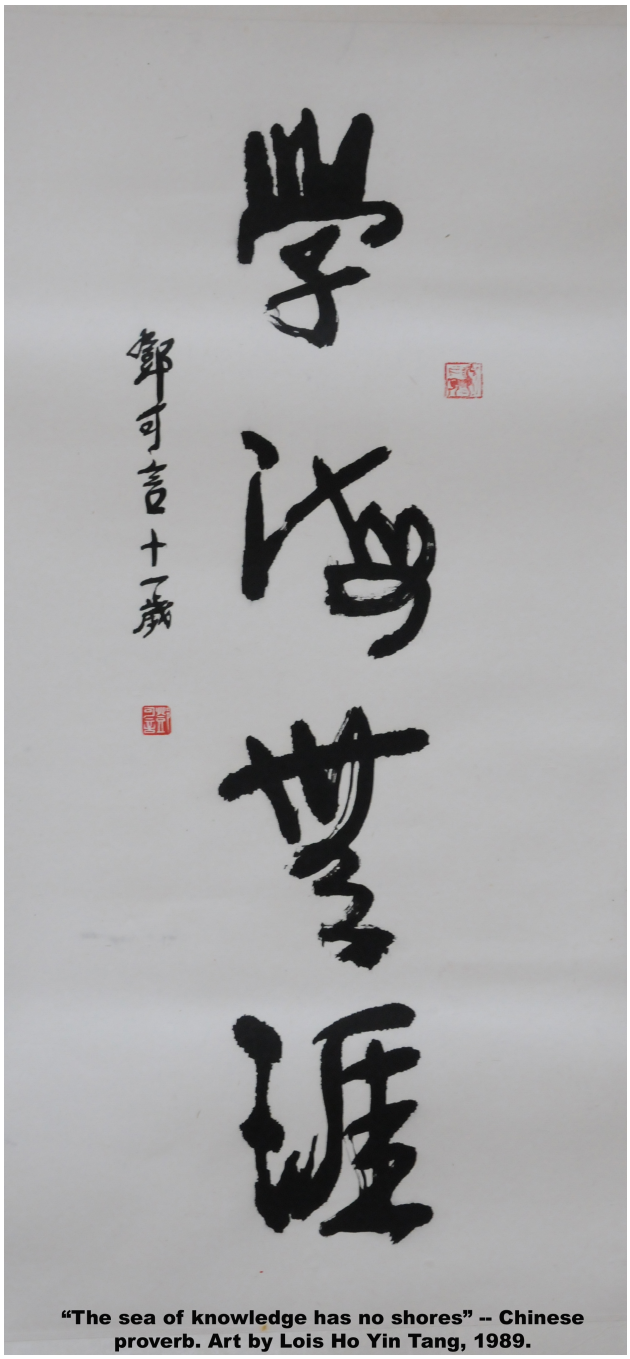

“The sea of knowledge has no shores” -- Chinese proverb. Art by Lois Ho Yin Tang, 1989.

Contents

List of acronyms

AFM:	Atomic Force Microscope;
CBED:	Convergent Beam Electron Diffraction;
CCD:	Charge-Coupled Device;
CD:	Circular Dichroism;
DDSCS:	Double Differential Scattering Cross Section;
DFF:	Dynamic Form Factor;
DFT:	Density Functional Theory;
DoS:	Density of States;
EDX:	Energy Dispersive X-ray;
EELS:	Electron Energy Loss Spectrometry;
EFS:	Energy Filtered Series;
EFTEM:	Energy-Filtered Transmission Electron Microscopy;
ELNES:	Energy Loss Near Edge Structure;
EMCD:	Energy-loss Magnetic Chiral Dichroism;
ESD:	Energy Spectroscopic Diffraction;
FWHM:	Full Width at Half Maximum;
HOLZ:	High Order Laue Zone;
LACDIF:	Large Angle Convergent DIFfraction;
LCC:	Laue Circle Center;
LCP:	Left-hand Circular Polarization;
MCD:	Magnetic Circular Dichroism;
MOKE:	Magneto-Optic Kerr Effect;
MDFF:	Mixed Dynamic Form Factor;
ORD:	Optical Rotatory Dispersion;
PEEM:	Photo Emission Electron Microscopy;

RCP:	Right-hand Circular Polarization;
SAA:	Selected Area Aperture;
SEA:	Spectrometer Entrance Aperture;
SEM:	Scanning Electron Microscope;
SNR or S/N:	Signal-to-Noise Ratio;
STEM:	Scanning Transmission Electron Microscope;
STM:	Scanning Tunneling Microscope;
STXM:	Scanning Transmission X-ray Microscope;
TEM:	Transmission Electron Microscope;
XAS:	X-ray Absorption Spectrometry;
XMCD:	X-ray Magnetic Circular Dichroism;
XNCD:	X-ray Natural Circular Dichroism;
ZLP:	Zero Loss Peak;

Chapter 1

Introduction

Dichroism is the property of certain materials that their photon absorption spectrum depends on the polarization of the incident radiation. In the case of X-Ray Magnetic Circular Dichroism (XMCD) the absorption cross section of a ferromagnet or a paramagnet in a magnetic field changes when the helicity of a circularly polarized probing photon is reversed relative to the magnetization. Although the similarities between X-ray Absorption Spectrometry (XAS) and Electron Energy Loss Spectrometry (EELS) in the Transmission Electron Microscope (TEM) have long been recognized, it was presumed that extending such equivalence to circular dichroism would require a beam of spin polarized electrons. Recently, it was argued on theoretical grounds that this is actually wrong [1]. In this Thesis I report the first direct experimental proof [2, 3] of magnetic circular dichroism in the TEM by comparing what has been named electron Energy-loss Magnetic Chiral Dichroism (EMCD) spectra with XMCD spectra, from the same specimen, together with theoretical calculations [4]. The experiment shows that chiral atomic transitions in a specimen are accessible with inelastic electron scattering under particular scattering conditions. The specimen itself is used as beam splitter and phase locker to obtain the equivalent in the TEM of circularly polarized photons. A broad range of experimental conditions is explored and the effect of several experimental parameters is studied and compared with *ab initio* simulations. A few alternative scattering conditions are detailed, together with their advantages and disadvantages, and demonstrated on $3d$ ferromagnets (Fe, Co and Ni single crystals). A theoretical justification of the effect is provided within the Bloch theory framework with the use of the Mixed Dynamic Form Factors (MDFFs). This result bears dramatic consequences

for the study of magnetism at high resolution. Whereas circular dichroism of many magnetic materials has been studied with synchrotron radiation for twenty years already [5], there is a number of technical limitations related to the spatial resolution and the signal depth with this technique. Circular dichroic experiments in the TEM, on the other hand, offer the potential of spatial resolutions down to the nanometer scale and provide depth information. The technique can therefore be of great help in the study of problems where magnetic information is needed on the nanometer scale, such as for interfaces or domain boundaries and in spin-torque based phenomena. Applications may be of benefit to electronic systems (miniaturization and characterization of magnetic recording media, spintronics, quantum size magnetic effects, etc.).

Chapter 2

Microscopy

Microscopy, from the Greek *micron* (small) and *skopein* (to look at), is the science of investigating objects that are too small to be seen by the unaided eye. The instruments used for such investigations are called microscopes and can be divided in two classes: optical theory microscopes and scanning probe microscopes. In the first case, an image is generated by the passage of a wave through the sample and magnified using lenses. In scanning probe microscopy, a probe (either a beam of particles or a tip in close contact to the sample) is scanned across the sample; by measuring the interactions between the probe and the sample a micrograph is generated.

2.1 A short history of microscopy

The ancient Greeks and Romans had already knowledge of lenses, mirrors and their power to affect light: Archimedes' burning glasses, used during the Roman siege of Syracuse in 212 BC, are probably the most famous example; they were mirrors and lenses used to focus the sun's rays to set fires on the enemy ships and siege machines.

Lenses are mentioned as early as the 424 BC as burning-glasses in Aristophanes' play *Nephelae (The clouds)*. The first mention of their use to help human vision can be found in the *Historia Naturalis* of Pliny the Elder (23–79), where Nero is said to have used an emerald to watch the gladiatorial games. The magnifying effects of a glass globe filled with water are also described there and in the writings of Seneca the Younger.

Widespread use of lenses did not occur until the use of *reading stones*

in the 11^{th} century and the invention of spectacles, probably in Italy in the 1280s. But it is only in the 16^{th} or 17^{th} century that the first light microscope was invented; the exact date and the name of the inventor are still a matter of debate. It is possible to distinguish between *simple microscopes*, composed by only one lens, or *compound microscopes*, when many lenses are used in succession to increase the magnification. It is impossible to say who invented the compound microscope. Dutch spectacle-maker Zacharias Janssen claimed to have invented it in 1590 together with his father Hans, but it was later shown that Zacharias was actually born around 1590. Another contender for the title of *inventor of the microscope* was Galileo Galilei. He developed an *occhiolino* or compound microscope with a convex and a concave lens in 1609. The first microscopic figure ever published is Francesco Stelluti's drawing of three bees, part of the seal of pope Urban VIII. An important contribution to microscopy was given at the end of the 17^{th} Century by Christiaan Huygens, another Dutchman. His two-lens ocular system was the first achromatically corrected and therefore a huge step forward in image quality.

Even though magnifying lenses had already been produced for over a century, it is Antony van Leeuwenhoek (1632-1723) and his simple microscope that first attracted the attention of biologists. He discovered how to create a very small, high-quality glass sphere with which he could make a very strong, single lens microscope (with claims that he was able to magnify up to several hundreds times). Since a single lens does not suffer the lens faults that are doubled or even multiplied when using several lenses in combination, it took about 150 years of optical development before the compound microscope was able to provide the same quality image as van Leeuwenhoek's simple microscopes. Armed with this unique instrument, he pioneered the exploration of the microscopic world. He was the first to observe and describe, among others, single celled organisms, muscle fibers, bacteria, spermatozoa and blood flow in capillaries. His discoveries helped overturn many of his time theories such as spontaneous generation of life and therefore, if not the father of the modern microscope, he has well deserved the title of father of microbiology.

The limits of the early optical (or light) microscope were mainly due to the aberrations caused by imperfections in the manufacturing of the lenses. As the lens-making technology improved further and further, an intrinsic limit was reached because of the phenomenon known as diffraction: when light passes through an aperture whose size is comparable to its wavelength, it acquires a typical angular and spatial distribution in amplitude. This pattern in the intensity of a diffracted wave arises from the interference between parts

of the wave that reached the point of observation by different optical paths. The diffraction pattern for a circular aperture consists of a series of concentric rings and the radial distribution of the intensity is given by a Bessel function (whose first zero is at 1.22 and defines the *Airy disk*).

Diffraction determines the theoretical resolution limit res for an aberration-free microscope [6]:

$$res = \frac{\lambda}{2n\sin(\theta_{ob})} \tag{2.1}$$

where θ_{ob} is the half angle of the cone of light accepted by the objective lens, n is the refraction index of the medium around the lens and object (typical values are 1 for air, 1.33 for pure water, and up to 1.56 for oils), and λ is the wavelength of light (550 nm for green light). Related to this is the Rayleigh criterion which gives the limit of the angular resolution θ_r due to diffraction of light through a circular aperture of radius r_{ob} as [7]:

$$\sin(\theta_r) = 1.22\frac{\lambda}{2nr_{ob}}. \tag{2.2}$$

The criterion is derived by assuming that two separate point-like light sources cannot be resolved if the first minimum of the radial intensity of one is located at the second maximum (the first maximum is at $\theta = 0$) of the other.

Even with oil, details finer than 200 nm cannot be distinguished in a light microscope. As the human eye can resolve points 0.1 mm apart at a distance of 10 cm, magnifications higher than x500 already reach the diffraction limit. There are several alternatives able to circumvent this limit and reach a resolution of a few nanometers. Eq. 2.1 shows that the wavelength of the radiation propagating through the sample is the limiting factor for optical theory microscopes. If rays with shorter wavelength, *e.g.* electromagnetic radiation (x-ray microscopy) or electron beams (transmission electron microscopy) are used, the intrinsic resolution limit can be pushed by several order of magnitude. For scanning probe microscopes, the resolution is limited only by the ability to manufacture small tips or produce fine beams of particles.

2.2 X-ray microscopy

X-rays (or Röntgen rays, from the name of the discoverer) have a wavelength comprised between 0.01 and 10 nm, covering the spectral frequencies between

extreme ultraviolet and gamma rays. They are sometimes further divided into soft x-rays (with lower energy and longer wavelength) and hard x-rays. The distinction with gamma radiation comes from their physical origin: x-ray photons are generated by energetic electron processes, gamma rays by transitions within atomic nuclei.

Given their wavelength, x-rays can be used in microscopes to image objects in the nanometer range. However, while lenses for visible light are made of a transparent material with an index of refraction substantially different from 1, there is no equivalent material for x-rays: for common solids and x-rays of general practice, refractive indices differ from unity by a value of the order of 10^{-5}. Therefore the only methods of x-ray manipulation are through reflection, diffraction and interference effects. Moreover, as x-rays are invisible to the human eye, indirect imaging methods have to be used, such as exposing films or charge-coupled device (CCD) detectors to measure the radiation passing through the specimen.

Early x-ray microscopes [8] used grazing-incidence reflective optics to focus the x-rays, with parabolic curved metallic mirrors and very high angles of incidence. Fresnel zone plates provide an alternative based on diffraction. A zone plate consists of a set of radially symmetric rings, known as Fresnel zones, which alternate between transparent and opaque. Waves hitting the zone plate will diffract around the opaque zones. The spacing of the zones is chosen so that the diffracted wave constructively interferes at the desired focus f, creating an image there. To obtain constructive interference at the focus, the zones should switch from opaque to transparent at radii r_n where

$$r_n = \sqrt{n\lambda f + \frac{n^2\lambda^2}{4}} \tag{2.3}$$

For the interference to be completely constructive at the focus, the amplitude of the diffracted waves from each zone in the zone plate must be the same. This means that for an evenly illuminated zone plate, the area of each zone must be equal. This implies that the width of the zones must decrease farther from the center. The maximum possible resolution of a zone plate depends on the smallest zone width, and, because of this, the smallest object that can be imaged is limited by how small the outermost ring can be reliably produced.

Zone plates are frequently manufactured using lithography as concentric gold or nickel rings on a silicon dioxide substrate. As lithography technology improves and the size of features that can be manufactured decreases,

the possible resolution of zone plates manufactured with this technique can improve and is today at the 25 nm limit [9].

The resolution of X-ray microscopy lies between that of the optical microscope and the electron microscope. It has an advantage over conventional electron microscopy in that it can view biological samples in their natural state. Electron microscopy is widely used to obtain images with nanometer level resolution but the relatively thick living cell cannot be observed as the sample has to be sliced thinly and then dried to get the image. Moreover organic samples are prone to outgas in the high vacuum needed for the operation of a TEM and this can alter their structure or even prevent the TEM from operating. However, it should be mentioned that cryo-electron microscopy allows the observation of biological specimens in their hydrated natural state. Until now the highest resolution is obtained by using the soft x-rays emitted from a synchrotron. Recently, more researchers have begun to use the soft x-rays emitted from laser-produced plasma rather than synchrotron radiation.

Additionally, x-rays cause fluorescence in most materials, and these emissions can be analyzed to determine the chemical composition of an imaged object. Another use is to generate diffraction patterns, a process used in X-ray crystallography. By analyzing the internal reflections of a diffraction pattern, the three-dimensional structure of a crystal can be determined down to the placement of individual atoms within its molecules. Often models of the structure can be verified or disproved by comparing a measured diffraction pattern with a simulated one.

2.3 Transmission electron microscopy

The TEM is a powerful investigation instrument and one of the most successful applications derived [10] from the wave-particle duality of matter *i.e.* that all particles also have a wave nature. The first proof of electron diffraction [11] was an important contribution to the establishment of the theory of quantum mechanics. Like all matter, electrons have both wave and particle properties (as theorized by Louis-Victor de Broglie [12]), and their wave-like properties mean that a beam of electrons can in some circumstances be made to behave like a beam of light. The wavelength is dependent on their energy, and so can be tuned by adjustment of accelerating fields, and can be much smaller than that of light, yet they can still interact with the sample

due to their electrical charge. Electrons are generated either by thermionic discharge (similar to a cathode ray tube) from a tungsten or lanthanum hexaboride (LaB_6) filament or by field emission; they are then accelerated by an electric field and focused by electrical and magnetic fields (produced by electromagnetic lenses) onto the sample, providing a resolution far better than with light microscopes, and with improved depth of vision. Most modern TEMs are operated with beam energies in the 100-300 keV range (but 1 MeV microscopes exist). For a 200 keV beam the relativistic wavelength is then:

$$\lambda = \frac{h}{m\gamma\beta c} = \frac{hc}{\sqrt{E(E+2mc^2)}} = 2.51\ pm \tag{2.4}$$

with $m\gamma$ being the relativistic electron mass, β the speed of the electron as fraction of the speed of light c and $h = 4.1357 \cdot 10^{-15}$ eV·s the Planck constant. Eq. 2.4 gives the order or magnitude of the resolution limit (eq. 2.1) for an aberration-free TEM. However a real lens is not free of aberrations. In 1936, just four year after the invention of the TEM, it was realized that electron lenses with rotational symmetry will always suffer from chromatic and spherical aberration [13] and that an additional multipole element has to be used to correct for them [14]. Spherical aberration is a lens flaw in which electrons further out of the optical axis experience an increased bending power. This causes a plane electron wave to be focused on a disk instead than on the focal point. This will of course affect the spatial resolution as a point object will appear in the image plane as a disk, whose radius r_{sph} is:

$$r_{sph} = C_s\theta_{ob}^3 \tag{2.5}$$

where θ_{ob} is again the maximum semiangle of collection of the objective aperture and C_s is the spherical aberration coefficient, a characteristic of the lens, usually equal [15] to the focal length (*i.e.* a few mm, 1.2 mm in the case of the TEM used for most of the experiments detailed in this dissertation). Spherical aberration plays also an important role in STEM (described later) as it determines how small can the beam size be made (finer probes have better spatial resolution). Another imperfection of the TEM lenses is the chromatic aberration, where the lens has different focusing effects on electron with different energies (this same phenomenon is the fundamental principle upon which the EELS spectrometer is built, see paragraph 4.3). As the focusing power of the lens is inversely related to the energy of the electron,

once again a point object emitting non-monochromatic electrons with energy E in the range $E_{min} < E < E_{max}$ will appear as a disk of radius r_{chr}

$$r_{chr} = C_c \frac{E_{max} - E_{min}}{E_{max}} \theta_{ob}^3 \tag{2.6}$$

with C_c being the chromatic aberration coefficient, also approximately equal to the focal length. It is important to note that the electron energy range is determined by the energy spread of the electrons emitted by the gun (which is different for different types of guns) but, more importantly, by the interaction with the specimen (as illustrated in paragraph 4.1).

The spherical aberration is usually the most important factor determining the ultimate spatial resolution of a TEM. The combination of the maximum theoretical limit (eq. 2.1) with eq. 2.5, for a typical value of θ_{ob} (1-10 mrad), yields [15] for the practical resolution res_p:

$$res_p \approx 0.9(C_s \lambda^3)^{\frac{1}{4}} \tag{2.7}$$

which is between 0.1 and 1 nm for most commercial TEMs.

Modern research TEMs may include aberration correctors in the objective lens, to reduce the amount of distortion in the image, allowing information on features on the scale of 0.1 nm to be obtained (resolutions down to 0.08 nm have been achieved, so far [16]) at magnifications of 50 million times. The correctors can be also mounted in the illumination system (some TEM have two correctors) in order to further reduce aberrations and to allow the formation of finer electron probe. Typical field emission guns produce an electron beam with a Gaussian energy spread of 0.7 eV at 200 keV; monochromators may also be used which reduce the energy spread to less than 0.15 eV.

As it was the case for x-rays, electrons are invisible to the human eye and therefore fluorescent screens, photographic films or CCD cameras are used to obtain images. Unlike x-rays, they interact strongly with matter: a few microns of any material would absorb all electrons in the beam. For this reason (and also to avoid electric arcs at the high-voltage gun system) there is the necessity to have high vacuum in a TEM column and to thin the specimens to a thickness of, at most, a few hundreds nm.

The capabilities of the TEM can be further extended by additional stages and detectors, sometimes incorporated on the same microscope. An electron cryomicroscope is a TEM with a specimen holder capable of maintaining the specimen at liquid nitrogen or liquid helium temperatures, allowing the

study of temperature dependent properties (see for example section 6.8). An analytical TEM is one equipped with detectors that can determine the elemental composition of the specimen by analyzing its x-ray spectrum (a spectroscopic technique called Energy Dispersive X-ray EDX) or the energy-loss spectrum of the transmitted electrons (EELS). Indeed any TEM can be equipped with such detectors, the difference being mostly in the configuration of the objective lens.

2.4 Scanning probe microscopy

Several scanning techniques and instruments have been developed. A detailed discussion of each of them goes beyond the purpose of this work, therefore only a short description of the most notable ones is presented.

According to the reciprocity theorem, a TEM can be operated in **Scanning Transmission Electron Microscopy** (STEM) mode by employing a system that scans the beam across the sample to form the image pixel by pixel and measuring the electron-matter interaction with suitable detectors. Indeed originally the *dedicated STEM*, was (and still is) a different kind of microscope built to be used only as scanning probe microscope. However nowadays it is very common for commercial TEM to be equipped with a raster system that enables the STEM mode.

In **Scanning Transmission X-ray Microscopy** (STXM) the X-rays are focused to a point and the sample is mechanically scanned through the produced focal spot. At each point the transmitted X-rays are recorded with a detector such as a proportional counter or an avalanche photodiode.

In both cases the probe must be able to pass through the sample and interact with it (*i.e.* a significant part of the beam must not be absorbed) and measurements provide bulk information. However this does not apply to all microscopy techniques. For example, this is the main difference between a STEM and a **Scanning Electron Microscope** (SEM). In a SEM, when the primary electron beam interacts with the sample, the electrons lose energy by repeated scattering and absorption within a teardrop-shaped volume of the specimen known as the interaction volume, which extends from less than 100 nm to around 5 μm into the surface. The size of the interaction volume depends on the beam energy, the atomic number of the specimen and the specimen's density. The energy exchange between the electron beam and the sample results in the emission of electrons and electromagnetic radiation,

which can be detected to produce an image. The most common imaging mode monitors low energy (< 50 eV) secondary electrons. Due to their low energy, these electrons originate within a few nanometers from the surface. The electrons are detected by an Everhart-Thornley detector which is a type of scintillator-photomultiplier device and the resulting signal is rendered into a two-dimensional intensity distribution that can be viewed and saved as a digital image. This process relies on a raster-scanned primary beam. The brightness of the signal depends on the number of secondary electrons reaching the detector. Using this technique, resolutions in the order of 1 nm or less are possible.

The equivalent synchrotron technique is called **Photo Emission Electron Microscopy** (PEEM). As for STXM, the x-rays are focused on a spot onto the sample surface. The distribution of (photo)electrons being emitted from the surface is then imaged. The technique has particular applications in magnetic domain imaging as with it all three components of the sample's magnetization can be measured (if polarized x-rays are used).

The **Scanning Tunneling Microscope** (STM) is an instrument developed in the 1980s that allows the study of surfaces at the atomic level. It probes the Density of States (DoS) of a material using tunneling current, with 0.1 nm lateral resolution and 0.01 nm depth resolution [17]. The STM can be used not only in ultra high vacuum but also in air and various other liquid or gas ambients, and at temperatures ranging from near 0 Kelvins to a few hundred degrees Celsius.

The STM is based on the concept of quantum tunneling. When a conducting tip is brought very near to a metallic or semiconducting surface, a bias between the two can allow electrons to tunnel through the vacuum between them. For low voltages, this tunneling current is a function of the local density of states at the Fermi level of the sample. Variations in current as the probe passes over the surface are translated into an image. STM can be a challenging technique, as it requires extremely clean surfaces and sharp tips.

Many other microscopy techniques have been developed based upon STM. These include photon scanning tunneling microscopy, which uses an optical tip to tunnel photons; scanning tunneling potentiometry, which measures electric potential across a surface; and spin polarized scanning tunneling microscopy, which uses a ferromagnetic tip to tunnel spin-polarized electrons from a magnetic sample, thus giving information on the polarized DoS.

The **Atomic Force Microscope** (AFM), invented in 1986, can be con-

sidered an evolution of the STM. It consists of a microscopic cantilever with a sharp tip (probe) at its end that is used to scan the specimen surface. The cantilever is typically silicon or silicon nitride with a tip radius of curvature on the order of nanometers. When the tip is brought into proximity of a sample surface, forces between the tip and the sample lead to a deflection of the cantilever according to Hooke's law of elasticity. Depending on the situation, forces that are measured in AFM include mechanical contact force, Van der Waals forces, capillary forces, chemical bonding, electrostatic forces, magnetic forces, Casimir forces, solvation forces, etc. Typically, the deflection is measured using a laser spot reflected from the top of the cantilever into an array of photodiodes. Other methods that are used include optical interferometry, capacitive sensing or piezoresistive AFM cantilevers. These cantilevers are fabricated with piezoresistive elements that act as a strain gage. Using a Wheatstone bridge, strain in the AFM cantilever due to deflection can be measured, but this method is not as sensitive as laser deflection or interferometry.

If the tip were scanned at a constant height, there would be a risk that the tip would collide with the surface, causing damage. Hence, in most cases a feedback mechanism is employed to adjust the tip-to-sample distance to maintain a constant force between the tip and the sample. Traditionally, the sample is mounted on a piezoelectric tube, which can move the sample in the z direction for maintaining a constant force, and the x and y directions for scanning the sample. Alternatively a 'tripod' configuration of three piezo crystals may be employed, with each responsible for scanning in the x,y and z directions. This eliminates some of the distortion effects seen with a tube scanner. The resulting map of the area s = f(x,y) represents the topography of the sample.

Chapter 3

Dichroism

Dichroism has two related but distinct meanings in optics. A dichroic material is either one which causes visible light to be split up into distinct beams of different wavelengths (colors), or one in which light rays having different polarizations are absorbed by different amounts. It is not to be confused with the phenomenon of dispersion in which the phase velocity of light is different for different frequencies, *i.e.* the refractive index is a function of the wavelength.

The original meaning of dichroic, from the Greek *dikhroos*, two-colored, refers to any optical device which can split a beam of light into two beams with differing wavelengths. Such devices include mirrors and filters, usually treated with optical coatings, which are designed to reflect light over a certain range of wavelengths, and transmit light which is outside that range. This kind of dichroic device does not usually depend on the polarization of the light. The term dichromatic is also used in this sense.

The second meaning of dichroic (treated in this thesis) refers to a material in which the absorption depends on the polarization of the incident light. The term came into use from the early observations of this effect in crystals such as tourmaline. In these crystals, the strength of the dichroism varies strongly with the wavelength of the light, making them appear to have different colors when viewed with light having differing polarizations or when viewed from different directions. This is more generally referred to as pleochroism, and this property can be used in mineralogy to identify minerals. In some materials, such as herapathite (iodoquinine sulfate) or Polaroid sheets, the effect is not strongly dependent on wavelength.

Some materials exhibit differing absorption of light of opposite *circular*

polarizations. This phenomenon is known as circular dichroism (CD) and is illustrated in fig 3.1. Optical activity is a related phenomenon where some molecules (said to be optically active) are able to rotate the polarization vector of impinging linearly polarized light. This is due to difference in the refractive index for the two types of circularly polarized light (see section 3.2).

3.1 Polarization of light

Polarization is the property of electromagnetic waves, such as light, that describes the direction of the transverse electric field. More generally, the polarization of a transverse wave describes the direction of oscillation in the plane perpendicular to the direction of propagation. Longitudinal waves such as sound waves do not exhibit polarization, because for these waves the direction of oscillation is along the direction of travel.

All electromagnetic waves propagating in free space or in a uniform material of infinite extent have electric and magnetic fields perpendicular to the direction of propagation. Conventionally, when considering polarization, the electric field vector is described and the magnetic field is ignored since it is perpendicular to the electric field and proportional to it. The electric field vector may be arbitrarily divided into two perpendicular components labeled x and y (with z indicating the direction of travel). For a simple harmonic wave, where the amplitude of the electric vector varies in a sinusoidal manner, the two components have exactly the same frequency. However, these components have two other defining characteristics that can differ. First, the two components may not have the same amplitude. Second, the two components may not have the same phase, that is, they may not reach their maxima and minima at the same time. The shape traced out in a fixed plane (called *polarization plane*) by the electric vector as such a plane wave passes over it (a Lissajous figure) is a description of the polarization state. When the two components are in phase, the ratio of their strengths is constant, so the direction of the electric vector (the vector sum of these two components) is constant. Since the tip of the vector traces out a single line in the polarization plane, this special case is called linear polarization. The direction of this line depends on the relative amplitudes of the two components.

If the two orthogonal components have exactly the same amplitude and are exactly ninety degrees out of phase, then one component is zero when

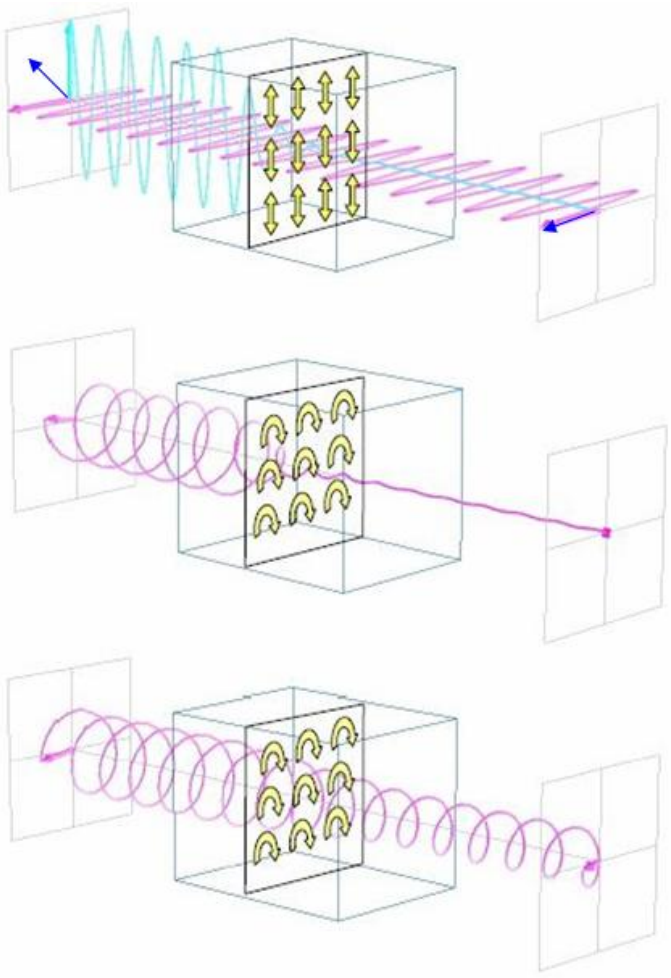

Figure 3.1: Electrical wave vectors of an electromagnetic wave passing a medium from left/back to right/front show the principle of dichroism. a) Linear dichroism: a wave polarized at 45 degrees with the horizontal plane (x and y components having the same amplitude) passes through the medium; the vertical component is attenuated and finally almost completely absorbed by interaction with an eigenmode reacting to vertical electric disturbances (symbolized by arrows). b) a right-handed circularly polarized wave is absorbed by interaction with an eigenmode of the medium showing right-handedness (symbolized by small arrows). c) a left-handed circularly polarized wave passes the medium with minimal attenuation. From Ref. [18].

the other component is at maximum or minimum amplitude. There are two possible phase relationships that satisfy this requirement: the x component can be ninety degrees ahead of the y component or it can be ninety degrees behind the y component. In this special case the electric vector traces out a circle in the polarization plane, so circular polarization is obtained. The direction in which the field rotates depends on the phase. These cases are called Right-hand Circular Polarization (RCP) and Left-hand Circular Polarization (LCP), depending on which way the electric vector rotates.

All other cases, that is where the two components are not in phase and either do not have the same amplitude and/or or the phase shift is not $\pm\pi/2$, are called elliptical polarization because the electric vector traces out an ellipse in the plane (the polarization ellipse).

Full information on a completely polarized state is then provided by the amplitude and phase of oscillations in the two components of the electric field vector in the plane of polarization. The amplitude and phase information can be conveniently represented as a two-dimensional complex vector (the Jones vector):

$$\vec{e} = a_1 e^{i\theta_1} e_x + a_2 e^{i\theta_2} e_y = e^{i\theta_1} \left(a_1 e_x + a_2 e^{i\Delta\theta} e_y \right). \tag{3.1}$$

Here a_1 and a_2 denote the amplitude of the wave in the two components of the electric field vector, while θ_1 and θ_2 represent the phases and $\Delta\theta = \theta_2 - \theta_1$ the relative phase. The product of a Jones vector with a complex number of unit modulus gives a different Jones vector representing the same ellipse, and thus the same state of polarization. The physical electric field, as the real part of the Jones vector, would be altered but the polarization state itself depends only on the relative phase $\Delta\theta$. A few examples are shown in table 3.1.

It is common to normalize Jones vectors such that the sum of the squares of their components is 1 and to constrain the first component to be a real number. However the basis of vectors used to represent the Jones vector need not represent linear polarization states (*i.e.* be real). In general any two orthogonal states can be used, where an orthogonal vector pair is formally defined as one having a zero inner product. A common choice is left and right circular polarizations:

$$\vec{e}_{RCP} \cdot \vec{e}_{LCP} = (1, i) \cdot (1, -i) = [1 \times 1 + i \times (-i)^*] = 0 \tag{3.2}$$

where the definition of inner product for complex vectors was used:

Table 3.1: Examples of polarizations and corresponding Jones vectors. For convenience, the identity $i = e^{i\frac{\pi}{2}}$ is used.

Polarization	**Jones vector**
Linear polarized in the x-direction	$(1, 0)$
Linear polarized in the y-direction	$(0, 1)$
Linear polarized at an angle θ from the x-axis	$(\cos\theta, \sin\theta)$
RCP	$(1, i)$
LCP	$(1, -i)$

$$\vec{z}\cdot\vec{z'} = (z_1, z_2, ..., z_n)\cdot(z'_1, z'_2, ..., z'_n) := [z_1(z'_1)^* + z_2(z'_2)^* + ... + z_n(z'_n)^*] \quad (3.3)$$

This is useful, for example, to model the different propagation of waves in two such components in circularly birefringent media (see figure 3.1) or signal paths of coherent detectors sensitive to circular polarization. In this case, linear polarization forming an angle θ with the x axis (third example in table 3.1) would be represented as:

$$\vec{e_\theta} = a(\vec{e}_{RCP} + e^{i2\theta}\vec{e}_{LCP}) \quad (3.4)$$

A comparison with eq. 3.1 shows that the tilt angle θ is half the phase difference $\Delta\theta$ between the two components. Jones vectors are usually given as two-components vectors because the polarization is always perpendicular to the direction of propagation. A three-component Jones vector would then be enough to completely describe any polarized photon.

In nature, electromagnetic radiation is often produced by a large number of individual radiators, producing waves independently of each other. This type of light is described as incoherent. In general there is no single frequency but rather a spectrum of different frequencies present, and even if filtered to an arbitrarily narrow frequency range, there may not be a consistent state of polarization. However, this does not mean that polarization is only a feature of coherent radiation. Incoherent radiation may show statistical correlation between the components of the electric field, which can be interpreted as partial polarization. In general it is possible to describe an observed wave field as the sum of a completely incoherent part (no correlations) and a completely polarized part. One may then describe the light in terms of the

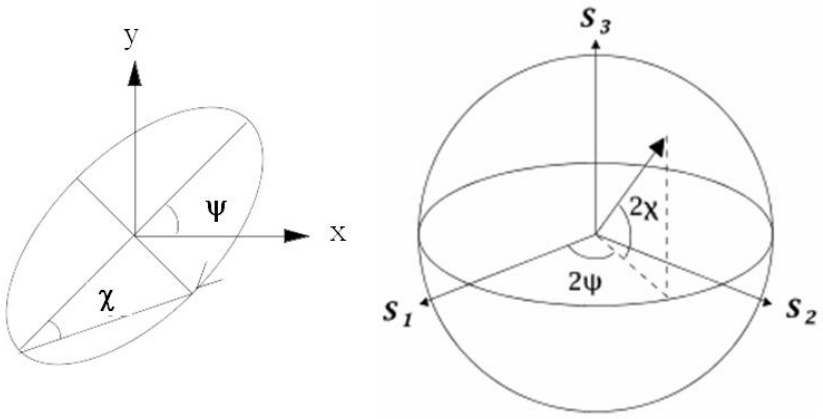

Figure 3.2: The Stokes parameters in relation to the Jones vector (polarization ellipse) in spherical coordinates.

degree of polarization and the parameters of the polarization ellipse. An alternative representation makes use of the *Stokes parameters*, defined as:

$$S_0 = I \tag{3.5}$$
$$S_1 = Ip\cos 2\psi \cos 2\chi \tag{3.6}$$
$$S_2 = Ip\sin 2\psi \cos 2\chi \tag{3.7}$$
$$S_3 = Ip\sin 2\chi \tag{3.8}$$

where I is the total intensity of the radiation, p the fractional degree of polarization and ψ is the angle between the major semi-axis of the polarization ellipse and the x-axis and χ is the arctan of the ratio of the two semi-axes(fig. 3.2). The factor of two before ψ represents the fact that any polarization ellipse is indistinguishable from one rotated by 180 degrees, while the factor of two before χ indicates that an ellipse is indistinguishable from one with the semi-axis lengths swapped accompanied by a 90 degrees rotation.

Table 3.2: Examples of polarizations and corresponding Stokes vectors.

Polarization	**Stokes vector**
Linear polarized in the x-direction	$(1, 1, 0, 0)$
Linear polarized in the y-direction	$(1, -1, 0, 0)$
Linear polarized at an angle θ from the x-axis	$(1, \cos 2\theta, \sin 2\theta, 0)$
RCP	$(1, 0, 0, 1)$
LCP	$(1, 0, 0, -1)$
Unpolarized	$(1, 0, 0, 0)$

The inverse relations are easily derived:

$$I = S_0 \tag{3.9}$$

$$p = \frac{\sqrt{S_1^2 + S_2^2 + S_3^2}}{S_0} \tag{3.10}$$

$$2\psi = \arctan \frac{S_2}{S_1} \tag{3.11}$$

$$2\chi = \arctan \frac{S_3}{\sqrt{S_1^2 + S_2^2}}. \tag{3.12}$$

The Stokes vector can be used to represent fully, partially or non-polarized light, whereas the Jones vector only covers the space of fully polarized light, but is more useful for problems involving coherent light. The four Stokes parameters are used because they can be calculated or measured quite easily. A few examples are shown in table 3.1, assuming light propagating in the z direction.

The concept of polarization of light can be used to understand some property of matter, such as birefringence. When a monochromatic beam of light passing through certain materials is split into two beams, the material is said to be birefringent (or double refracting; this phenomenon is not to be confused with dispersion). Only anisotropic materials can exhibit birefringence and this occurrence is explained by the different values of the refraction index n for light with polarization parallel (n_1) or perpendicular (n_2) to the axis of anisotropy, due to different values of the dielectric constant in the two directions. Referring to eq. 3.1 and assuming e_x to be parallel to the axis of anisotropy, light not traveling in the e_x direction will be split into two waves (called the ordinary ray and the extraordinary ray) because its two

components will propagate with different speed inside the material and will be refracted with different angles. Linearly polarized light passing through such material for a distance L will become elliptically polarized (unless either a_1 or $a_2 = 0$) as the two components acquire a phase shift:

$$\Delta\theta = 2\pi(n_1 - n_2)\frac{L}{\lambda}. \tag{3.13}$$

Therefore, for carefully chosen values of the incident polarization and the length L a sheet of a birefringent material can be used to convert linear into circular polarization and vice versa. In materials with more than one axis of anisotropy trirefringence occurs, which is characterized by three different values of the refractive index.

3.2 Chirality and circular dichroism

In circularly polarized light the electric field vector has a constant length, but rotates about its propagation direction. Hence, it forms a helix in space while propagating. If this is a left-handed helix the light is referred to as left circularly polarized and vice versa for a right-handed helix.

The term *chiral* is used to describe an object which is non-superimposable on its mirror image, that is an object that cannot be made coincident to its mirror image by rotations and translations alone. A chiral object and its mirror image are said to be enantiomorphs. In chemistry, the two mirror images of a chiral molecule are referred to as enantiomers. The word chirality is derived from the Greek *cheir* (hand), the most familiar chiral object; the words enantiomorph and enantiomer stem from the Greek *enantios* (opposite) and *morphe* (form) or *meros* (part). A non-chiral object is called achiral or amphichiral. The letter A is achiral as it is superimposable to its mirror image. Human hands are perhaps the most universally recognized example of chirality. No matter how the two hands are oriented, it is impossible for all the major features of both hands to coincide. This difference in symmetry becomes obvious if someone attempts to shake the right hand of a person using his left hand, or if a left-handed glove is placed on a right hand. Because this difference is universally known and easy to observe, many pairs of enantiomers are designated as right- and left-handed (there are several naming conventions: +/- or R/S or D/L). The helix is another example of a chiral three-dimensional object. The letters S and Z also exhibit chirality,

but only in a two-dimensional space.

Enantiomers have, when present in a symmetric environment, identical chemical and physical properties except for their ability to rotate plane-polarized light by equal amounts but in opposite directions. A mixture of equal parts of an optically active isomer and its enantiomer is termed *racemic* and has a net rotation of plane-polarized light of zero. Two symmetrical enantiomers often have different chemical properties related to other substances that are also enantiomers, hence the need to distinguish them by a prefix before the chemical name of the substance. Since many molecules in the bodies of living beings are enantiomers themselves, there is often a marked difference in the effects of two symmetrical enantiomers on living beings, including human beings.

For example, D-form amino acids tend to taste sweet, whereas L-forms are usually tasteless. Spearmint leaves and caraway seeds respectively contain L-carvone and D-carvone - enantiomers of carvone. These smell different to most people because our olfactory receptors also contain chiral molecules. Penicillin's activity is stereoselective. The antibiotic only works on peptide links of D-alanine which occur in the cell walls of bacteria - but not in humans. The antibiotic can kill only the bacteria, and not us, because we don't have these D-amino acids.

One chiral object that interacts differently with the two enantiomers of a chiral compound is circularly polarized light: an enantiomer will transmit left- and right-circularly polarized light to differing degrees. This is the basis of optical activity and circular dichroism spectroscopy. Usually the difference in absorptivity in the visible light - UV range is relatively small (parts per thousand).

Optical activity is the rotation of linearly polarized light as it travels through certain materials. It occurs in solutions of chiral molecules such as sucrose (sugar), solids with rotated crystal planes such as quartz, and spin-polarized gases of atoms or molecules. It is used in the sugar industry to measure syrup concentration, in optics to manipulate polarization, in chemistry to characterize substances in solution, and is being developed as a method to measure blood sugar concentration in diabetic people.

The rotation of the orientation of linearly polarized light was first observed in 1811 in quartz by French physicist Dominique F. J. Arago. Around this same time, Jean Baptiste Biot (famous for the law, named after him and Félix Savart, which describes the magnetic field generated by a steady current) also observed the effect in liquids and gases of organic substances

such as turpentine and tartaric acid. In 1822, the English astronomer Sir John F.W. Herschel discovered that different crystal forms of quartz rotated the linear polarization in different directions. Simple polarimeters have been used since this time to measure the concentrations of simple sugars, such as glucose, in solution. In fact, one name for glucose, dextrose, refers to the fact that it causes linearly polarized light to rotate to the right (latin: *dexter*) side. Similarly, levulose, more commonly known as fructose, causes the plane of polarization to rotate to the left.

In 1848, Louis Pasteur resolved the problem concerning the nature of tartaric acid [19]. A solution of this compound obtained from living things (specifically, wine lees; the word racemic is derived from the Latin word for grape) rotated the plane of polarization of light passing through it, but tartaric acid derived by chemical synthesis had no such effect, even though its reactions were identical and its elemental composition was the same. Pasteur noticed that the crystals came in two asymmetric forms that were mirror images of one another. Sorting the crystals by hand gave two forms of the compound: solutions of one form rotated polarized light clockwise, while the other form rotated light counterclockwise. An equal mix (racemic) of the two had no polarizing effect on light. Pasteur correctly deduced that the molecule in question was asymmetric and could exist in two different forms that resemble one another as would left- and right-hand gloves, and that the organic form of the compound consisted purely of one type. This was the first time anyone had demonstrated chiral molecules. The discovery deeply impressed in him the belief that asymmetry is a characteristic of life only and chirality differentiates the organic world from the mineral world. This pushed him into the fields of medicine and biology that made him famous.

Optical activity is a type of birefringence. In an optically active material the two circular polarizations experience different refractive indices n. The difference in the indices quantifies the strength of the optical activity and is a characteristic of the material. After traveling through a length L of material the two polarizations pick up a relative phase (referring to eq. 3.4 and defining $\Delta\theta'$ as the phase difference after traversing the sample) of:

$$\Delta\theta' = \Delta\theta + \frac{2\pi L}{\lambda}(n_{RCP} - n_{LCP}) \tag{3.14}$$

where λ is the wavelength of the light in vacuum. Consequently, the final polarization is rotated to an angle $\theta + \Delta\theta'/2$. Optical activity can also occur with achiral compounds when the experimental geometry is chiral [20].

Generally, the refractive index depends on the wavelength. The variation in rotation with the wavelength of the light is called Optical Rotatory Dispersion (ORD). ORD spectra and circular dichroism spectra are related through the Kramers-Kronig relations. Complete knowledge of one spectrum allows the calculation of the other. In a CD experiment, equal amounts of left and right circularly polarized light are sequentially radiated into a (chiral) solution. One of the two types is absorbed more than the other one and this wavelength dependent difference of absorption is measured, yielding the CD spectrum of the sample. It should be noted that, in the case of materials exhibiting CD, linearly polarized light is transformed into elliptical (or circular) polarization as the amplitude of the RCP and LCP component is different after passing through the sample (fig. 3.1).

3.3 Magnetic circular dichroism

In the presence of magnetic fields all molecules have optical activity. A magnetic field aligned in the direction of light propagating through a material will cause the rotation of the plane of linear polarization. This is known as Faraday effect (discovered by Michael Faraday in 1845) and it was the first experimental evidence that light and electromagnetism are related. The effect is identical to the Magneto-Optic Kerr Effect (MOKE, discovered in 1877 by John Kerr) except that MOKE is a measurement of the reflected light, while the Faraday effect is a measurement of the transmitted light. In a magneto-optic material the presence of a magnetic field (either externally applied or because the material itself is ferromagnetic) can cause a change in the permittivity tensor ϵ of the material [21]. The tensor becomes anisotropic, with complex off-diagonal components, depending of course on the frequency of incident light. If the absorption losses can be neglected, ϵ is a Hermitean matrix. The resulting principal axes become complex as well, corresponding to elliptically-polarized light where LCP and RCP components travel at different speeds (analogous to birefringence).

More specifically, for the case where absorption losses can be neglected, the most general form of Hermitean ϵ is:

$$\epsilon = \begin{pmatrix} \epsilon'_{xx} & \epsilon'_{xy} + ig_z & \epsilon'_{xz} - ig_y \\ \epsilon'_{xy} - ig_z & \epsilon'_{yy} & \epsilon'_{yz} + ig_x \\ \epsilon'_{xz} + ig_y & \epsilon_{yz} - ig'_y & \epsilon'_{zz} \end{pmatrix} \tag{3.15}$$

or equivalently the relationship between the displacement field $\vec{D}$ and the electric field $\vec{E}$ is:

$$\vec{D} = \epsilon\vec{E} = \epsilon'\vec{E} + i\vec{E} \times \vec{g} \tag{3.16}$$

where ϵ' is a real, symmetric matrix and $\vec{g}$ is a real pseudovector called the *gyration vector*, whose magnitude is generally small compared to the eigenvalues of ϵ'. The direction of $\vec{g}$ is called the axis of gyration of the material. To first order, $\vec{g}$ is proportional to the applied magnetic field:

$$\vec{g} = \epsilon_0\chi\vec{H} \tag{3.17}$$

ϵ_0 being the permittivity of free space, χ the magneto-optical susceptibility (a scalar in isotropic media, but more generally a tensor). If this susceptibility itself depends upon the electric field, one can obtain a nonlinear optical effect of magneto-optical parametric generation.

The simplest case to analyze is the one in which $\vec{g}$ is a principal axis (eigenvector) of ϵ', and the other two eigenvalues of ϵ' are identical. Then, if $\vec{g}$ is taken to be in the z direction for simplicity, the ϵ tensor simplifies to the form:

$$\epsilon = \begin{pmatrix} \epsilon_1 & ig_z & 0 \\ -ig_z & \epsilon_1 & 0 \\ 0 & 0 & \epsilon_2 \end{pmatrix} \tag{3.18}$$

Most commonly, one considers light propagating in the z direction (parallel to $\vec{g}$). In this case the solutions are elliptically polarized electromagnetic waves with phase velocities $v = [\mu(\epsilon_1 \pm g_z)]^{-\frac{1}{2}}$ (where μ is the magnetic permeability). This difference in phase velocities leads to the Faraday effect.

The matter is quite different in the case of Magnetically induced Circular Dichroism (MCD), that is the differential absorption of RCP and LCP light in the presence of a magnetic field. MCD will only exist at a given wavelength if the atom or molecule has an absorption band at that wavelength. This is distinctly different from the related phenomenon of ORD, which can be observed at wavelengths far from any absorption band. When the absorption occurs (and is probed) in the x-ray wavelength region, the phenomenon is known as X-ray MCD (XMCD) [5, 22, 23, 24, 25] and it should not be confused with X-ray Natural Circular Dichroism (XNCD) [26]. It usually involves ionization of atoms, *i.e.* electronic transitions from core atomic states

to unoccupied states above the Fermi energy. It is a routine investigation technique common to many synchrotron beam lines.

The physical origin of XMCD can be understood when calculating the transition probabilities of an electron from a core state to a free state above the Fermi energy. When a circularly polarized photon with helicity parallel to the magnetization is absorbed, the target atom acquires a quantum of angular momentum. This means that only transitions which obey the $\Delta J = \pm 1$ selection rule are allowed. Of particular interest are the $L_{2,3}$ edges of $3d$ magnetic transition metals, which correspond to electronic transitions from the $2p$ core states to unoccupied s or d valence states. Contributions corresponding to $p \rightarrow s$ transitions can be neglected with respect those which correspond to $p \rightarrow d$ transitions [27].

Photons with +1 and -1 helicity respectively induce the additional selection rule $\Delta m=1$ and $\Delta m=-1$. Moreover the magnetic field lifts the l-degeneracy of the final state through Zeeman splitting (*i.e.* states with different magnetic quantum number m have different energies even if they have the same n and l). One can already deduce that photons with opposite helicity can force transitions to different final states, which may be differently occupied (or have different DoS). The resulting spectral lines will then have different intensities, thereby explaining how polarization affects the shape of the final absorption spectrum.

In order to provide a simple and intuitive picture of the principle of MCD, a two-step model is detailed in the following. MCD can be thought of as composed by two distinct processes: in the first one a photon is absorbed by a core electron, which is thereby excited and polarized; in the second process, the photoelectron is absorbed into an empty state above the Fermi Energy, with a probability proportional to the local DoS. If the two events are assumed independent, so that the photoelectron polarization P_e does not depend on the details of the final states, the absorption spectrum can be described by simple formulas. This two-step picture was developed in analogy with the predictions of Fano [28], who first suggested the possibility of producing spin-polarized electron by exciting ions with circularly polarized photons. Spin-dependent photon absorption is very similar to the Fano effect except that the excited electrons are usually in bound states, some of which may already be populated and therefore unable to participate in the transition. The photoelectron polarization P_e refers to the unobserved intermediate state between the two processes (in which all possible states are available) and therefore it is neither the polarization of the initial core state

(usually zero) nor of the final states. It is then a useful quantity only if the transition probabilities depend at most weakly on the final states. In general, the transition probabilities W (given by the Fermi Golden rule for a perturbation operator V):

$$W \propto |\langle i\,|V|\,f\rangle|^2\,\rho(f) \tag{3.19}$$

depend on the DoS $\rho(f)$ of the final states $|f\rangle$. From this one might deduce that the two abovementioned processes cannot be treated independently because the transition strength depends on the nature of the final state of the photoelectron. However, even if the population of the final state is not known, if all other quantum numbers are given (and most of them are specified by the selection rules), one could calculate the matrix element in eq. 3.19 as the only quantity needed in the first process.

The wave function of a non-relativistic electron moving under the influence of a spherical potential can be separated into two parts, one giving the radial dependence and the other the angular dependence:

$$\left\langle \vec{R}|\psi \right\rangle = \psi(R)\psi(\theta,\phi). \tag{3.20}$$

Substituting in eq. 3.19 one obtains:

$$\left\langle i\left|V(\vec{R}\right|f\right\rangle = \underbrace{\int \psi_i(R)V(R)\psi_f^*(R)R^2dR}_{A_R}\underbrace{\int\int \psi_i(\theta,\phi)V(\theta,\phi)\psi_f^*(\theta,\phi)d\theta d\phi}_{A_\nu}, \tag{3.21}$$

which means that the matrix element in eq. 3.19 can be decomposed into an angular term (A_ν, with ν=+1 for RCP and -1 for LCP) and a radial term A_R. The radial integral A_R is more difficult to calculate as it depends on the detailed radial distributions of the wave functions, which are in turn dependent on the details of the spherical potential V. In the particular case that the differences in the radial integrals are negligible, the relative strength of the transition probabilities can be calculated from the angular integrals alone, which are quite straightforward to calculate. If the initial and final wave functions are states with well defined l and m_l, their angular part is given by spherical harmonics. The angular term is therefore a function of only l, m_l, l' and m_l' [25, 29]:

$$A_{\pm1} = \pm A_{l+1,\pm m_l+1}\delta_{l',l+1}\delta_{m_l',m_l\pm1} \mp A_{l,\mp m_l}\delta_{l',l-1}\delta_{m_l',m_l\pm1} \tag{3.22}$$

with

$$A_{l,m_l} = \sqrt{\frac{(l+m_l)(l+m_l-1)}{2(2l+1)(2l-1)}} \tag{3.23}$$

A calculation of the MCD effect for a ferromagnetic transition metal magnetized in the z direction by an external magnetic field $\vec{B}$ is detailed here as example. The final spin-up and spin-down states have the same DoS shifted in energy with respect to each other because of the magnetic field (spin-up states being lower in energy because parallel to the magnetization), which is the same as saying that the valence band is spin-polarized. For the core states the spin-orbit coupling means that m_l and m_s are no longer good quantum numbers and that only $J = l + s$ and its projection m_j are, because it is the total angular momentum J (and m_j) that determines the energy of the atomic state. Therefore the six $2p$ states that give rise to the $L_{2,3}$ edge can now be divided into two $2p_{1/2}$ states (L_2 edge) and four $2p_{3/2}$ states (L_3 edge) with two different energies (neglecting the small Zeeman splitting between states with the same J but different m_j). Each state can be now uniquely identified as $|j, m_j\rangle$ ($n = 2, l = 1, s = 1/2$ is implied) instead of $|m_l, m_s\rangle$. If one wants to calculate the transition probability to the continuum above the Fermi energy, then the $|j, m_j\rangle$ states should be decomposed into a superposition of $|m_l, m_s\rangle$ states (which have a well defined spin) by making use of the Clebsch-Gordan coefficients. One finds that, for example:

$$\left|\left|j=\frac{1}{2}, m_j=\frac{1}{2}\right\rangle\right|^2 = \frac{2}{3}\left|\left|m_l=1, m_s=-\frac{1}{2}\right\rangle\right|^2 + \frac{1}{3}\left|\left|m_l=0, m_s=\frac{1}{2}\right\rangle\right|^2 \tag{3.24}$$

$$\left|\left|j=\frac{1}{2}, m_j=-\frac{1}{2}\right\rangle\right|^2 = \frac{2}{3}\left|\left|m_l=-1, m_s=\frac{1}{2}\right\rangle\right|^2 + \frac{1}{3}\left|\left|m_l=0, m_s=-\frac{1}{2}\right\rangle\right|^2 \tag{3.25}$$

and similarly for the other $|j, m_j\rangle$ states. The transition probabilities are then easily calculated from the matrix elements between initial and final states with the same spin number because the perturbation (photon absorption) does not act on the spin space. The transition probabilities are shown in fig. 3.3 for positive helicity, *i.e.* Δm=1 and fig. 3.4 for Δm=-1. These probabilities, multiplied by the weights of each $|m_l, m_s\rangle$ state, give for the L_2 edge a polarization of -1/2 for RCP and +1/2 for LCP, which is equivalent to say that the spin down transitions are respectively 75% and 25% of the total. The corresponding calculation for the L_3 gives a value of 1/4 (RCP)

and -1/4 (LCP) for the polarization. P_e for the L_3 edge is half that of the L_2 edge and with opposite sign, therefore the L_3 spectral intensity is expected to be opposite in sign when compared to L_2. Moreover, as there are four core states involved in the L_3 edge (compared to only two for L_2), the absolute dichroism (difference) at L_3 should be equal in value. It is also possible to evaluate, for both helicities and edges, the mean value of the orbital moment of the final excited states which, together with the mean value of the spin, is the origin of the sum rules [23, 24]. In the second process of the two-step model, the polarized photoelectron is absorbed into the final state and the spectral intensity of the transition is determined by the available (spin polarized) DoS. In the example shown in figs. 3.3 and 3.4 there are more unoccupied spin down states than spin up states, therefore the intensity of the L_2 edge will be stronger for RCP than for LCP because for RCP P_e is negative (the opposite is true for the L_3 edge).

3.4 Applications of XMCD

Nowadays, information on orbital and spin magnetization, magnetic ordering and strong electronic correlation in a variety of ferro- and ferrimagnetic compounds is being deduced from XMLD and XMCD with the aid of modern synchrotrons providing highly polarized beams with a brilliance of up to 10^{19} photons per (second mm^2 $mrad^2$) and 0.1% bandwidth. These techniques become increasingly important for the rapidly expanding field of spintronics. In this context, the need for increased spatial resolution is evidenced by two pathways:

a) XMCD-PEEM is based on the photoelectron emission microscope, which was first demonstrated in 1988. This method is restricted to ultrathin surface layers and has been used at several synchrotron beam lines such as PEEM2 at ALS, U2 at BESSY, IS-PEEM at SPring-8 for imaging of magnetic domains. The actual lateral resolution is some ten nm. Next-generation will have improved resolution PEEM2 at ALS, XM-1, or the SMART project) but are unlikely to approach the nm range in the next 5 years. The actual limit of lateral resolution in the magnetic x-ray imaging (with different methodology and optical schemes) is around 100 nm, meaning that routinely many instruments in the world may achieve 0.3/0.5 micron spot, and few of them arrive to 25 nm, also in magnetic contrast. The expected values, within two years, are in the range of 10 nm, with the dream of less than this.

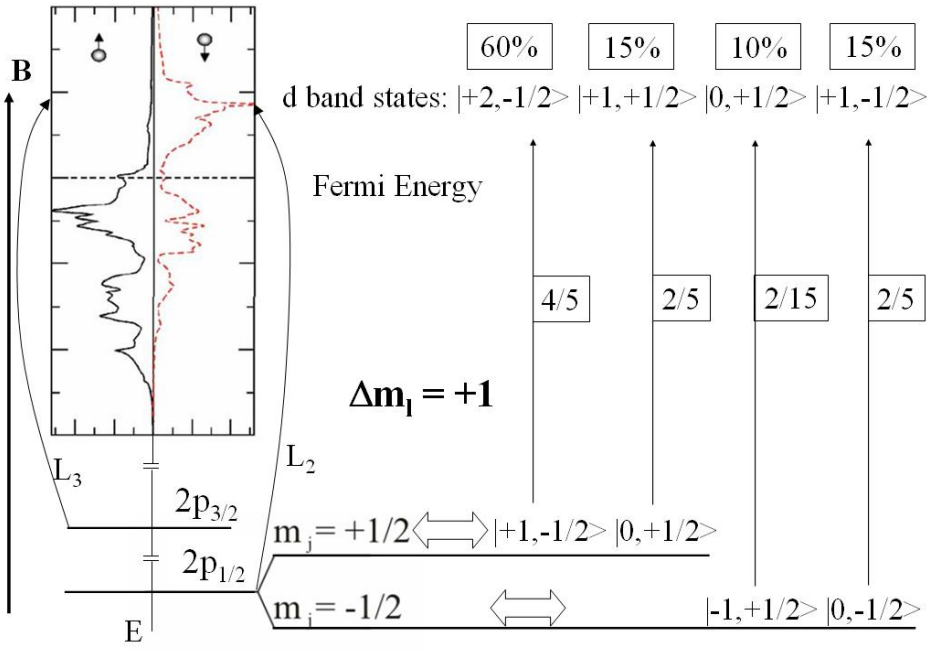

Figure 3.3: Principle of XMCD. When a photon is absorbed, one core electron is excited from a $2p$ state to a d state in the continuum above the Fermi energy. The spin-orbit coupling and an external magnetic field cause the $2p$ core state to split into 2 energy levels, corresponding to two $2p_{1/2}$ states (L_2 edge) and four $2p_{3/2}$ states (L_3 edge; the Zeeman splitting for different values of m_j is negligible). The magnetic field also causes the polarization of the final states, shifting down in energy the DoS (in this example calculated for bcc Fe) of the spin up states (solid line) with respect to the spin down states (dashed line). When a RCP photon is absorbed the selection rule $\Delta m = +1$ applies. Decomposing the core states into $|m_l, m_s\rangle$ states allows for an easy calculation of the relative transition probabilities W from eqs. 3.19, 3.22, 3.23, indicated by the numbers near the transition arrows. These transitions probabilities, multiplied by the weights of the $|m_l, m_s\rangle$ decomposition given in eqs. 3.25, correspond to the photoelectron polarization P_e indicated by the percentages above the final states.

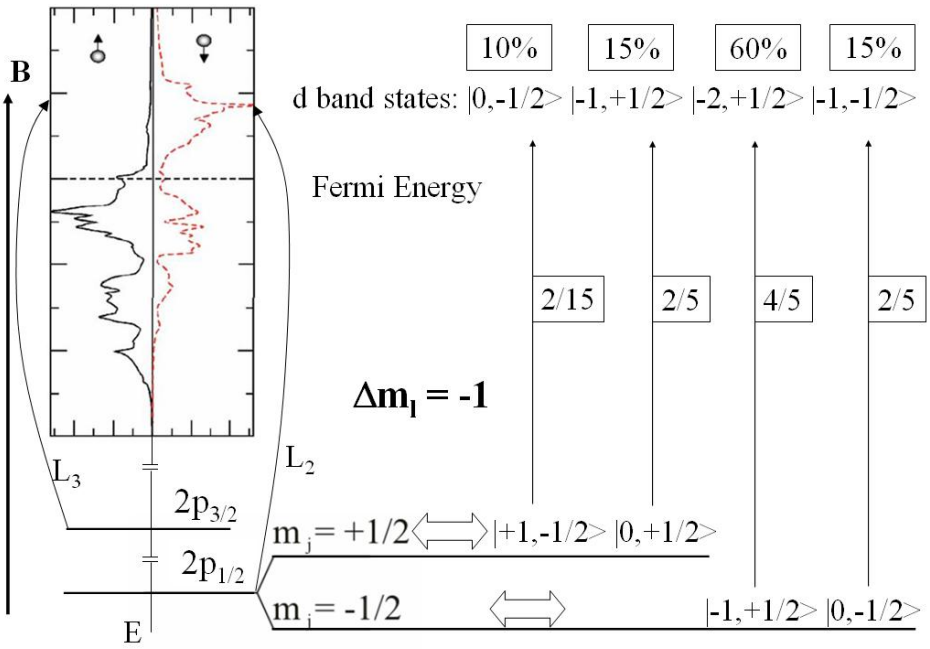

Figure 3.4: Same as fig. 3.3 for the absorption of a LCP photon.

b) X-ray microscopes with Fresnel lenses operate in transmission geometry. They have resolution of the order of 30 nm.

c) X-ray spectro-holography [30] is a new technique able to detect XMCD with 50 nm resolution. It is however limited to sample upon which a holographic mask can be deposited.

Chapter 4

Electron Energy Loss Spectrometry

Electron energy-loss spectrometry is an investigation technique in which a thin sample is exposed to a beam of electrons with a known, narrow range of kinetic energies such as the one produced in a TEM. Some of the electrons will undergo inelastic scattering, which means that they lose energy and have their paths slightly and randomly deflected. The amount of energy loss can be measured via an electron spectrometer and interpreted in terms of what caused the energy loss. Inelastic interactions include phonon excitations, inter and intra band transitions, plasmon excitations, inner shell ionizations, and Cherenkov radiation. The inner shell ionizations are particularly useful for detecting the elemental components of a material.

The technique was developed by James Hillier and R. F. Baker [31, 32] in the mid 1940s but was not widely used over the next 40 years, only becoming more widespread in research in the 1980s due to advances in microscope instrumentation and vacuum technology. With modern instrumentation becoming widely available in laboratories worldwide, the technical and scientific developments from the mid 1990s have been rapid.

There are several basic variants of EELS, primarily classified by the geometry and by the kinetic energy of the incident electrons (typically measured in kilo-electron-volts, or keV). Probably the most common today is transmission EELS, in which the kinetic energies are typically 100 to 300 keV and the incident electrons are detected after passing through the material sample. Usually this occurs in a TEM, although some dedicated systems exist which enable extreme resolution in terms of energy and momentum transfer at the

expense of spatial resolution.

Other variants include *reflection EELS* (including reflection high-energy electron energy-loss spectroscopy, typically at 10 to 30 keV) and *aloof EELS* (sometimes called near-field EELS) in which the electron beam does not in fact strike the sample but instead interacts with it via the long-ranged Coulomb interaction; aloof EELS is particularly sensitive to surface properties but is limited to very small energy losses such as those associated with surface plasmons or direct interband transitions.

Within transmission EELS, the technique is further subdivided into *valence EELS* (which measures plasmons and interband transitions) and *inner-shell ionization EELS* (which provides much the same information as x-ray absorption spectroscopy, but from much smaller volumes of material). The dividing line between the two, while somewhat ill-defined, is in the vicinity of 50 eV energy loss.

4.1 The electron energy-loss spectrum

The addition of an EELS spectrometer enables the TEM to perform microanalysis and characterization of solids by identifying the many different interactions between the electron beam and the sample. In many cases this information can be obtained without losing the high spatial resolution provided by the TEM. Therefore EELS is able to take full advantage of modern aberration-corrected probe-forming systems to attain spatial resolutions down to 0.1 nm, while with a monochromated electron source and/or careful deconvolution the energy resolution can be 100 meV or better. This has enabled detailed measurements of the atomic and electronic properties of single columns of atoms, and in a few cases, of single atoms. As the information is extracted from the entirety of the volume sampled, the highest resolution is achieved in either STEM mode or with Converged Beam Electron Diffraction (CBED) techniques (see paragraph 6.6).

A typical spectrum is shown in fig. 4.1. The maximum of intensity can be found at an energy loss of 0 eV and it is usually referred to as the Zero Loss Peak (ZLP). It represents electrons that have interacted elastically or quasi-elastically with the specimen, *i.e.* they haven't suffered an energy loss measurable within the energy resolution of the spectrometer. These include Bragg scattered electrons and those which have excited phonon modes, for which the energy loss is less than the experimental energy resolution. In-

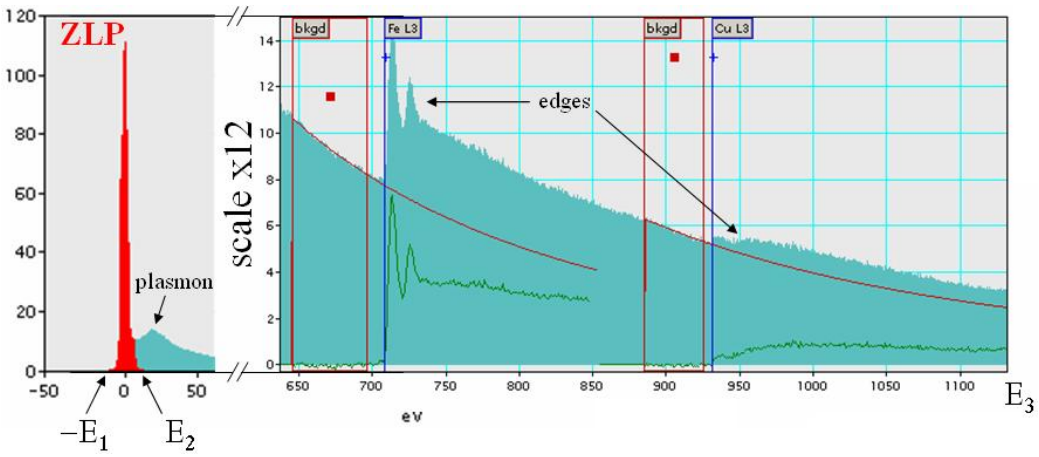

Figure 4.1: Typical electron energy loss spectrum. The most prominent features in the low loss region are the Zero Loss Peak (ZLP) and the plasmon peak. The shaded area under the ZLP is proportional to the number of elastically scattered electrons. For higher energy losses, the background decreases with a power law AE^r and its contribution can be calculated by fitting it in an energy window set immediately before a core-loss edge, so that the ELNES can be obtained, as it has been done here before the Fe and Cu edges. The white lines of Fe can be seen at an energy of 708 and 721 eV.

elastic scattering from outer-shell electrons is visible in the energy region of 5 - 50 eV (the so called *low loss region*) and may involve many atoms of the solid, a collective effect known as plasmon, and transitions among the different valence and conduction bands of the solid and, for materials with high enough refractive index, Cherenkov peaks.

The plasmon is the quasiparticle resulting from the quantization of plasma oscillations just as photons and phonons are quantizations of light and sound waves, respectively. Thus, plasmons are collective oscillations of the free electron gas density, often at optical frequencies. Since plasmons are the quantization of classical plasma oscillations, most of their properties can be derived directly from Maxwell's equations. For example in the Drude model the sample is treated as a three dimensional crystal of positively charged ions, and a delocalized electron gas is moving in the periodic potential of this ion grid.

Plasmons play a large role in the optical properties of metals. Light of frequency below the plasma frequency is reflected, because the electrons in the solid screen the electric field of the light. Light of frequency above the plasma frequency is transmitted, because the electrons cannot respond fast enough to screen it. In most metals, the plasma frequency is in the ultraviolet, making them shiny (reflective) in the visible range. Some metals, such as copper and gold, have electronic interband transitions in the visible range, whereby specific light energies (colors) are absorbed, yielding their distinct color. In doped semiconductors, the plasma frequency is usually in the deep ultraviolet. That is why they are reflective, too.

The plasmon energy can often be estimated in the free electron model as

$$E_p = \hbar \sqrt{\frac{n_v e^2}{m \epsilon_0}} \tag{4.1}$$

where n_v is the valence electron density, e is the elementary charge, m is the electron mass and ϵ_0 the permittivity of free space.

As the optical properties of a solid are determined by the valence electrons, the analysis of this spectral region using the Kramers-Kronig relations is important. In addition to these volume plasmons, which are excited within the specimen, longitudinal waves of charge density travel along the specimen surfaces and cause surface plasmons. They occur at the interface between vacuum or a material with a positive dielectric constant and a material with a negative dielectric constant (for example a metal or doped dielectric).

At higher energy losses, the electron scattering cross section decreases as AE^r where E is the energy loss and A, r are experimental parameters. Superimposed on the decreasing electron intensity are features which represent inner-shell excitations, which are commonly referred to as edges. A sharp rise occurs at the ionization threshold, the spectral position of which is given approximately by the binding energy of the corresponding atomic shell. Since inner-shell binding energies depend on the atomic number of the scattering atom, the ionization edges indicate which elements are present within the specimen. Thus, quantitative elemental analysis is possible. Core-loss spectra recorded from solid specimens show a pronounced fine structure, taking the form of peaks or oscillations in intensity within 50 eV of the ionization threshold and called Energy Loss Near Edge Structure (ELNES). Most of this structure reflects the influence of the surrounding atoms and the local density of free state for the atom being ionized. For crystals, ELNES contains information about the valence and conduction band and can therefore be compared to bandstructure calculations.

Other visible features in the spectrum are relativistic and retardation effects [33, 34]. These effects become important when the electron traverses the solid faster than the speed of light in the specimen. In this case, Cherenkov radiation is emitted by the probe electron. This in turn causes the appearance of additional features in the EELS spectrum. These losses are predominantly observed at an energy range of 0 - 10 eV and make a direct determination of the dielectric function, the optical refractive index, and band gaps difficult or even impossible.

4.2 Multiple scattering

If the energy loss spectrum is recorded from a sufficiently thin region of the specimen, each spectral feature corresponds to a different excitation process. The probability that a transmitted electron will be scattered more than once increases with increasing thickness of the sample, giving a total energy loss that is the sum of the individual losses. In the case of plasmon scattering, the result is a series of peaks at multiples of the plasmon energy (fig. 4.2).

In the low energy response, many-body effects play a dominant role and prevent a straightforward prediction of scattering cross sections by the use of wave mechanics. Thus an alternative description is necessary and the local bulk dielectric function ε, based on Maxwell theory, is employed. Hence ε is

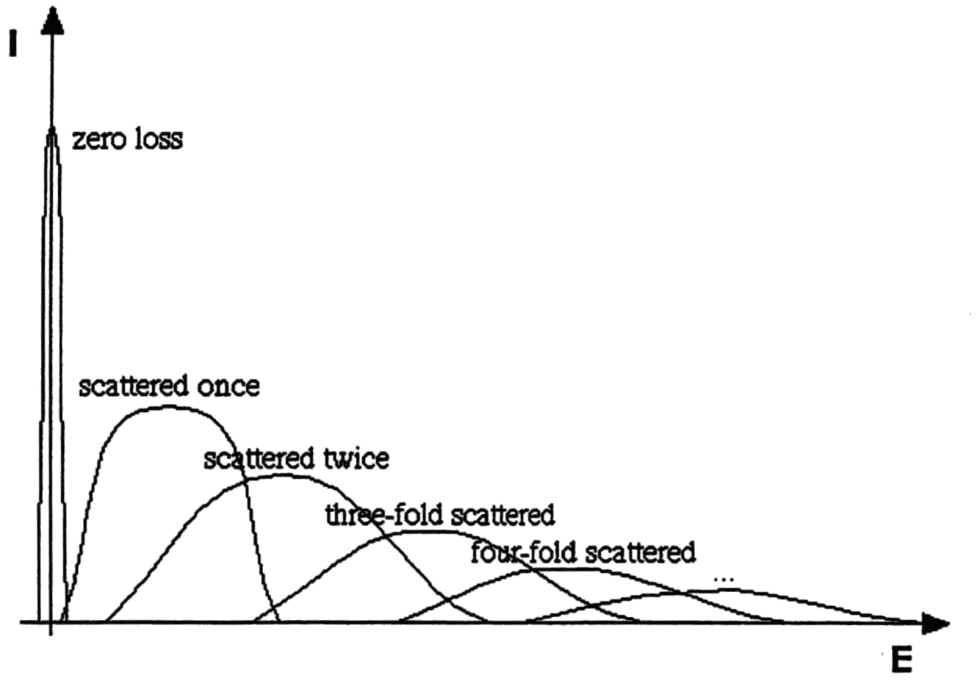

Figure 4.2: Series of plasmon peaks due to multiple scattering. Courtesy of Michael Stöger-Pollach.

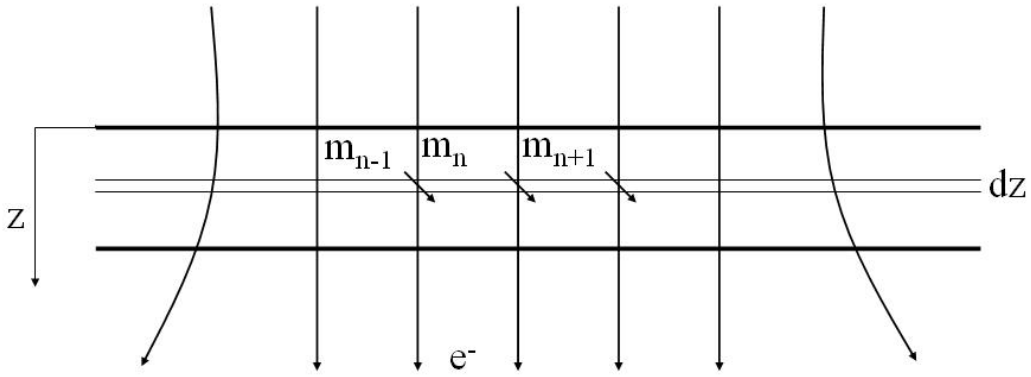

Figure 4.3: Schematic representation of multiple scattering in a thin sample. From Ref. [35].

determined by electronic properties such as interband transitions, absorption edges, and resonant dipole excitation.

Multiple scattering can be reduced by preparing very thin specimens, but it can never be eliminated nor neglected. However its effects on the EELS spectra can be simulated and removed with a deconvolution process [35]. When the electron beam passes through the specimen, assuming the electrons are scattered by small angles, the probability Q_n of the electron being scattered n times is only dependent on the depth z in the specimen. The assumption of small scattering angles is justified for the high energy electrons of a TEM (hundreds of keV).

Indicating with $m_n(z)$ the number of electrons scattered n-fold at a depth z, the variation of m within a distance dz is (fig. 4.3):

$$dm_n = (m_{n-1} - m_n)\,\alpha dz \tag{4.2}$$

with α being the rate of scattering. The scattering probability is then:

$$\dot{Q}_n(z) = \alpha\,(Q_{n-1} - Q_n) \tag{4.3}$$

with the solution

$$Q_n(z) = \frac{(z\alpha)^n}{n!} e^{-\alpha z} \tag{4.4}$$

which is a Poissonian distribution. For $n = 0$ the well-known exponential attenuation of the incident beam is reproduced:

$$I(z) = I(0)\, e^{-\frac{z}{\Lambda}}, \tag{4.5}$$

where $\Lambda = \alpha^{-1}$ is the electron mean free path. The plural scattering peaks have appreciable intensities if the specimen thickness is close to the mean free path Λ.

In a classical particle model of scattering, the mean free path Λ of electrons in matter is defined as the mean distance between two scattering events. Generally Λ is a direct measure of the intensity of scattering from each atom and inversely proportional to the scattering cross section.

The mean free path Λ (in nm) is given by:

$$\Lambda \approx \frac{106F\left(\frac{E_0}{E_m}\right)}{ln\left(2\beta\frac{E_0}{E_m}\right)} \tag{4.6}$$

$$F = \frac{1 + E_0/1022}{(1 + E_0/511)^2} \tag{4.7}$$

where F is a relativistic factor, E_0 is the incident electron energy in keV, β is the collection semiangle in mrad, and E_m is the mean energy loss (in eV), which depends on the chemical composition of the specimen [36]:

$$E_m \approx 7.6Z^{0.36} \tag{4.8}$$

Z being the atomic number.

Eq. 4.6 is only valid for $\beta \ll \sqrt{E/E_0}$ because it is based on a dipole approximation; in practice, this means collection semiangles up to about 10 mrad for $E_0 = 200$ keV.

The knowledge of Λ allows the determination of the specimen thickness with the Log-Ratio method. For a specimen of thickness t, the probability Q_n that a transmitted electron suffers n collision is given by eq. 4.4:

$$Q_n = (1/n!)\,(t/\Lambda)^n \exp(-t/\Lambda) \tag{4.9}$$

with t/Λ the mean number of collisions. Q_n is represented in the energy loss spectrum by the ratio of the energy-integrated intensity of the n-fold scattering, divided by the total integrated intensity:

$$Q_n = \frac{I_n}{I_t} \tag{4.10}$$

For a given order n of scattering, the intensity is highest when $t/\Lambda = n$. In the case of the unscattered component (n=0, the ZLP), the intensity has a maximum for $t = 0$ and decreases exponentially with specimen thickness. Combining eqs. 4.9 and 4.10 one has (for $n = 0$):

$$t/\Lambda = ln\,(I_t/I_0)\,. \tag{4.11}$$

Measurement of I_t and I_0 involves a choice of two adjacent energy ranges (delimited in fig. 4.1 by $E_{1,2,3}$, with the shaded area being I_0). The lower limit (E_1) of the zero-loss region can be taken anywhere to the left of the ZLP (where the intensity should be zero). The separation point (E_2) may be taken at the first minimum in intensity, assuming that errors arising from the overlapping tails of the ZLP and the inelastic part cancel each other. The upper limit (E_3) should correspond to an energy loss above which the further contribution to I_t are negligible with respect to the experimental accuracy.

4.3 The spectrometer

An EELS spectrometer uses the fact that electron with different kinetic energies follow different trajectories when immersed in an electric or magnetic field. When the more or less monochromatic electron beam passes through the specimen, some electrons lose energy and can be dispersed, *i.e.* spatially separated and detected.

One of the more common spectrometer designs makes use of a sector magnet (fig. 4.4), which produces an uniform magnetic field $\vec{B}$ perpendicular to the electron path (in the y direction in fig. 4.4). The magnetic field exerts a force $\vec{F}$ on the electron (of charge e, mass m and speed $\vec{v}$) equal to:

$$\vec{F} = e(\vec{v} \times \vec{B}). \tag{4.12}$$

As this force is always perpendicular to the electron velocity, the electron is put in a circular motion, whose radius r can be calculated from the centripetal acceleration $\vec{a}$ using the third law of dynamics:

$$\vec{F} = m\vec{a} \Rightarrow evB = \frac{mv^2}{r} \tag{4.13}$$

from which it follows:

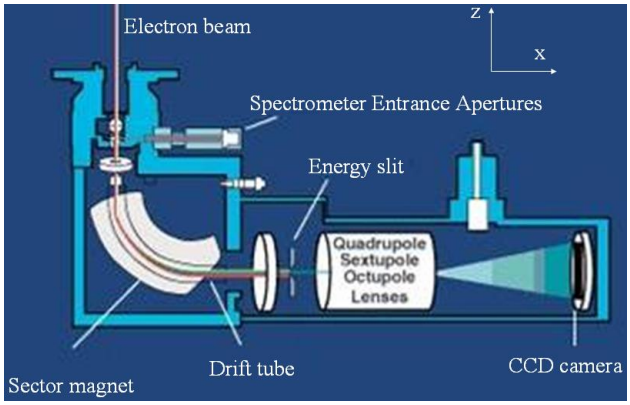

Figure 4.4: Scheme of the spectrometer for EELS (from http://www.gatan.com/analysis/gif_2000.php).

$$r = \frac{mv}{eB}. \tag{4.14}$$

The radius is different for electrons with different energies (velocities) and it is now possible to measure the number of electrons which have lost a certain energy E by placing a slit or a CCD camera at the corresponding value of r. This kind of spectrometer can be easily attached beneath the camera chamber of a TEM as an accessory and its usefulness makes it a common instrument in many TEM labs. As is the case with camera plates, the electron beam can enter the spectrometer only once the screen is raised.

An important feature of all spectrometers is focusing. Focusing in the perpendicular direction comes from the fringe fields which have a component B_x. The sector behaves as a magnetic lens with a strong chromatic aberration in one direction. In an uncorrected magnetic prism, the focusing is correct to the first order. Commercially available spectrometers have cylindrically curved surfaces that provide second order focusing (thus correcting the aberrations to the second order).

The spectrometer also has two *conjugate planes*: in an ideal optical system the rays from every point in the object space pass through the system so that they converge to or diverge from a corresponding point in the image space. This corresponding point is the image of the object point, and the two are said to be conjugate to each other (object and image functions are interchangeable). By projecting one such plane onto a screen or CCD camera

and using an appropriate energy selecting slit between the two planes, it is possible to obtain an energy filtered image of the object placed in the other conjugate plane, *i.e.* an image formed by using only electrons which have lost a well-defined energy. This principle is realized in the Gatan Imaging Filter (the instrument used for the experiments in this thesis). If the object in the first conjugate plane is the projection of the specimen image, then the technique is called Energy-Filtered Transmission Electron Microscopy (EFTEM). If the object is a projection of the back focal plane of the objective lens (where the diffraction pattern of a crystal would take form), the procedure is called Energy Spectroscopic Diffraction (ESD). This is made possible by the prespectrometer coupling lens, which is built so as to project an image onto the entrance of the spectrometer, where one of several Spectrometer Entrance Apertures (SEA) can be selected. The lower focus of the coupling lens coincides with the object plane of the spectrometer. By changing the excitation of the coupling lens, the TEM projects either an image or a diffraction pattern at the spectrometer entrance plane. By changing the excitation of the spectrometer lenses, the spectrometer projects either one of the conjugate plane or the point with maximum chromatic dispersion on the CCD camera. In the first case one obtains an image of the object projected on the SEA, in the second case a spectrum is obtained (the latter is the normal EELS mode).

In the normal EELS mode, since the electron beam is dispersed only in one direction (z in figure 4.4), the spectrum image contains additional spatial information in the y direction, which corresponds to the y direction of the object projected on the SEA. Usually this information is integrated out to produce an $I(E)$ plot such as the one in fig. 4.1. The energy loss information contained in the spectrum originates from an area in the specimen which is the area that falls within the SEA (or equivalently, the area on the screen delimited by the projected SEA). Since an EELS spectrum can be used to identify the elements present in the investigated area, high resolution imaging, combined with EELS, constitutes a microanalysis tool with the potential to detect clusters of few atoms or, in some cases, even single atoms [35, 37].

EFTEM is routinely used to aid chemical analysis of the sample in conjunction with complementary techniques such as electron crystallography. The energy slit can be adjusted so as to only allow electrons which have not lost energy to pass through to form the image. This prevents inelastic scattering from contributing to the image, and hence produces an enhanced contrast image.

Adjusting the slit to only allow electrons which have lost a specific amount of energy can be used to obtain elementally sensitive images. As the ionization signal is often significantly smaller than the background signal, it is normally necessary to obtain more than one image at varying energies to remove the background effect. The simplest method is known as the *jump ratio* technique, where an image recorded using electrons at the energy of the maximum of the absorption peak caused by a particular inner shell ionization is divided by an image recorded just before the ionization energy. In the ratio image thus obtained, regions of the sample which do not contain the element that caused the edge will appear darker than regions which contain said element. A more elaborate and accurate approach is the so called *three-windows method*, where two pre-edge images (in different but not distant energy ranges) are taken and used to extrapolate, pixel by pixel, the background correction for the post-edge image. For both methods it is often necessary to cross-correlate the images to compensate for relative drift of the sample between the acquisitions. By repeating one of these procedures for every core-loss edge of interest and then combining the result, it is possible to obtain a false color image of the sample where each element is color coded. If the elements in the sample have well separated plasmon peaks, it is possible to construct such an elemental map from the plasmon losses. This has the advantage that the intensity of the signal is much higher than for core-losses (therefore reducing the relative importance of spatial drift), but the resulting image can nonetheless appear blurred because of the non-local nature of the plasmon.

Improved elemental maps can be obtained by taking an Energy Filtered Series (EFS) of images with small, adjacent energy windows spanning the range of interest [38]. The resulting set of data is called the *EELS data cube* and contains both spatial and energy-loss information. An alternative way to record the EELS data cube [39] is to use a STEM probe to scan the image and simultaneously record an EELS spectrum for each pixel.

Angle-resolved EELS and ESD are the equivalent of EELS and EFTEM in the reciprocal space. Since the TEM is being operated in diffraction mode, the information is collected from the entire illuminated area: when a Selected Area Aperture (SAA) is used, this is typically a circular region of 100-5,000 nm diameter. In the case of angle-resolved EELS, the spectrum shows the energy lost by the electrons which have been scattered onto a particular direction and have therefore transferred a well defined linear momentum $\hbar\vec{q}$ to the target. On the other hand, ESD produces an energy filtered image

Table 4.1: TEM and EELS modes

TEM	Spectrometer	Description
Image	Imaging	EFTEM
Image	Spectroscopy	EELS
Diffraction	Imaging	ESD
Diffraction	Spectroscopy	angle-resolved EELS

(with a well defined energy window) of the angular distribution of the electrons scattered by the solid. When taking an EFS in diffraction mode, a different EELS data cube is obtained, containing angular distribution (in two dimensions) and energy loss information.

To summarize, the spectrometer can be operated in four different modes, depending on:

a) what is being projected onto its entrance plane (these are more properly TEM modes as they concern the mode of operation of the TEM); one can distinguish between image mode (an image is projected on the TEM screen or the SEA) and diffraction mode (a diffraction pattern is projected on the TEM screen or the SEA).

b) what is being projected onto the spectrometer CCD camera (these are proper spectrometer modes, as the internal optic of the spectrometer has to be adjusted). One can distinguish between spectroscopy (energy dispersed electrons hit the camera) and imaging mode (only electrons with the same energy can reach the camera).

4.4 Applications of EELS

EELS is often spoken of as being complementary to EDX spectroscopy, which is another common spectroscopy technique available on many electron microscopes. EDX can be used in a broader energy loss range, is quite easy to use, and is particularly sensitive to heavier elements. EELS has historically been a more difficult technique but is in principle capable of measuring atomic composition, chemical bonding, valence and conduction band electronic properties, surface properties, and element-specific pair distance distribution functions. EELS tends to work best at relatively low atomic numbers, where the excitation edges tend to be sharp, well-defined, and at

experimentally accessible energy losses (the signal being very weak beyond about 3 keV energy loss). EELS is perhaps best developed for the elements ranging from carbon through the $3d$ transition metals (from scandium to zinc). For carbon, an experienced spectroscopist can tell at a glance the differences among diamond, graphite, amorphous carbon, and mineral carbon (such as the carbon appearing in carbonates). The spectra of $3d$ transition metals can be analyzed to identify the oxidation states of the atoms. Cu(I), for instance, has a different white-line intensity ratio than does Cu(II). This ability to fingerprint different forms of the same element is a strong advantage of EELS over EDX. The difference is mainly due to the difference in energy resolution between the two techniques (1 eV or better for EELS, $\geq$ 100 eV for EDX, but they in general depend on the element under analysis and the type of detector). Also, for energy losses below 1 keV EELS is more sensitive than EDX.

When compared to XAS, the main advantage comes from the attainable spatial resolution.

Chemical microanalysis is performed by identifying all core-loss edges in the EELS spectrum. This operation is not always straightforward, because the energy loss at which an edge occurs is proportional to the *effective* nuclear charge experienced by the excited electron. This net charge is roughly equal to the total number of proton in the nucleus minus the number of electrons in the shells laying closer to the nucleus. Therefore, even if the energy loss associated to each K edge is different for every element, it might happen that K edges of a lighter element overlap partially with the L (or M, N, etc.) edges of heavier elements. For example the L_3 edge of Potassium (Z = 19) occurs at 294 eV energy loss and the K edge of Carbon (Z = 6) is at 284 eV. Moreover the energy onset of a certain elemental edge may change because of the environment in which the element is found (an effect called chemical shift).

After removing the multiple scattering background, the scattering cross section can be calculated and, from this, the number of scatterer per unit area of the specimen. To obtain the chemical composition it is sufficient to calculate the ratio of this numbers. When the background subtraction is not possible because two or more edges overlap, the spectrum can be analyzed by least-square fittings with standard spectra of known composition and thickness.

The spectral shape of every edge is strongly affected by the free density of states above the Fermi Energy. The DoS is determined by the chemical

environment and many computer codes exist nowadays that can give quite accurate prediction of the spectral features. An example is given in fig. 4.5, where the carbon K edge is modeled for cementite (Fe_3C) and ferrite (bcc-Fe) with C impurities in an interstitial site.

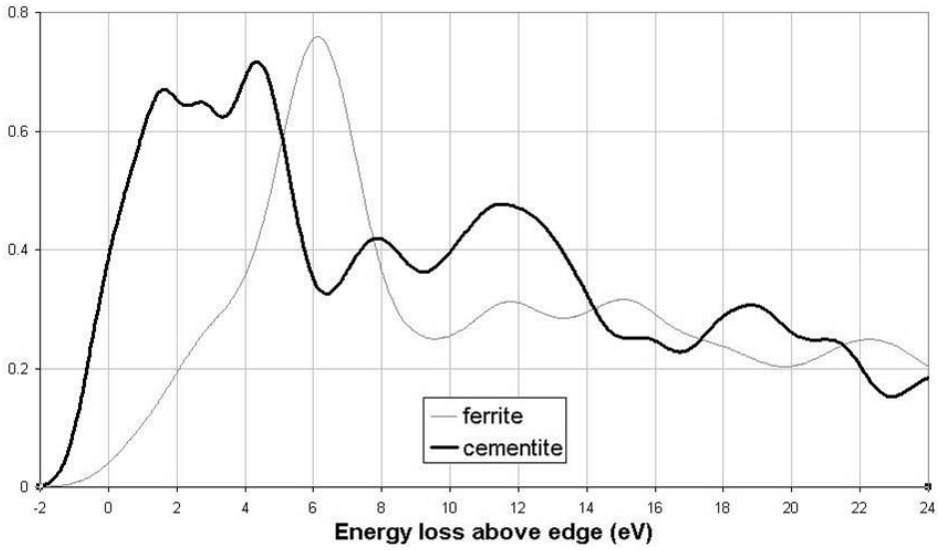

Figure 4.5: Simulated ELNES for cementite (Fe_3C) and a ferrite supercell containing a C atom in an interstitial position with a Fe:C ratio of 27:1. The differences in the position and width of the main peak, as well as the presence of accessory peaks can be used to determine experimentally the type of chemical environment of the C in a sample.

Additional information can be obtained by the extended energy-loss fine structure, an oscillation in the post-edge intensity related to the distance of an excited atom to its next-neighbors. This allows to measure changes of the order of 1% in the lattice constant.

Site specific chemical information can be obtained in a crystal by exploiting the Bloch dynamical diffraction theory that will be more extensively presented in chapter 5. The fast electron inside the crystal is described by Bloch waves with the same periodicity of the crystal lattice. For particular scattering conditions the fast electron density can be forced to assume very high values for certain atomic sites (and correspondingly low values for the other atomic sites), *i.e.* the probe electron is *channeled* into a specific atomic

column. In a crystal that contains two or more species of atoms this effect can provide information on which sort of atom can be found at a specific lattice site and, for anisotropic atoms, what its orientation is. This technique is called ELCE [40, 41].

Chapter 5

EMCD theoretical framework

In the past it was assumed that magnetic circular dichroism cannot be detected with electrons except with spin polarized ones. But, from the previous exposition in paragraph 3.3 one can notice that in XAS the photon does not couple directly to the spin of electrons but to the angular momentum of the excited atom, and the effect becomes visible by the spin-orbit coupling [25]. So there is no reason that spin polarized electrons are needed for detection of circular dichroism in EELS. Rather, in the inelastic electron interaction that is equivalent to an XMCD experiment, the virtual photon that is exchanged must be circularly polarized.

This chapter presents theoretical *ab initio* predictions of the dependence of the dichroic signal in EMCD measurements on several experimental conditions, such as sample thickness, detector placement, size of convergence and collection angles and kinetic energy of the fast electron. This information should help optimize the experimental geometry in order to maximize the Signal-to-Noise ratio (SNR).

A great deal of work has been carried out to improve the predictive capacity of several numerical simulation methods for XMCD. The case of localized orbitals (like M edges of rare earth or L edges of light transition metals) was investigated by use of multiplet methods [42, 43]. Multiple scattering theory was successfully applied to more delocalized orbitals like the K-edge of iron [44] or for the extended fine structures of the Gd L_2 and L_3 edges [45]. The band structure code WIEN2k was applied to the calculation of XMCD at the uranium M_2 and M_3 edges [46] and to the calculation of the closely related Faraday and Voigt effects [47, 48]. The development of sum rules allows to retrieve directly spin and orbital moments from the experiment [23, 48, 49, 50].

Partially based on these results, an extension [4] of the WIEN2k package was developed, with the purpose of simulating the EMCD effect in EELS spectra.

5.1 Method of calculation

The derivations of the Double Differential Scattering Cross Section(DDSCS) presented in Refs. [51, 52] will be followed. Within the first-order Born approximation [53] the DDSCS is written as

$$\frac{\partial^2\sigma}{\partial\Omega\partial E} = \frac{4\gamma^2}{a_0^2}\frac{k_f}{k_i}\frac{S(\vec{q},E)}{q^4} \tag{5.1}$$

with

$$S(\vec{q},E) = \sum_{i,f} |\langle i|e^{i\vec{q}\cdot\vec{R}}|f\rangle|^2 \delta(E_f - E_i - E) \tag{5.2}$$

where $\vec{q} = \vec{k}_f - \vec{k}_i$ is the difference (wave vector transfer) between final wave vector $\vec{k}_f$ and initial wave vector $\vec{k}_i$ of the fast electron; $\gamma = 1/\sqrt{1 - v^2/c^2}$ is a relativistic factor and a_0 is the Bohr radius. The $S(\vec{q},E)$ is the Dynamic Form Factor (DFF) [54]. The difference with respect to paragraph 5.2 and specifically eq. 5.8 (and derivations) is that this is the more general case where the dipole approximation is not used.

This equation is valid only if the initial and final wave functions of the fast electron are plane waves. In the crystal the full translation symmetry is broken and as a result, the electron wave function becomes a superposition of Bloch waves, which reflects the discrete translation symmetry. Each Bloch wave can be decomposed into a linear combination of plane waves - it is a coherent superposition of (an in principle infinite number of) plane waves. The wave function of the fast electron can be thus written as

$$\psi(\vec{r}) = \sum_g \sum_j \epsilon^{(j)} C_g^{(j)} e^{i(\vec{k}^{(j)}+\vec{g})\cdot\vec{r}} \tag{5.3}$$

for incident wave and

$$\psi'(\vec{r}) = \sum_h \sum_l \epsilon^{(l)} D_h^{(l)} e^{i(\vec{k}^{(l)}+\vec{h})\cdot\vec{r}} \tag{5.4}$$

for outgoing wave, where $C_g^{(j)}$, $D_h^{(l)}$ are Bloch coefficients, $\epsilon^{(j)}$ ($\epsilon^{(l)}$) determine the excitation of the Bloch wave with index j (l) and wave vector $\vec{k}^{(j)}$ ($\vec{k}^{(l)}$) and $\vec{g}$ ($\vec{h}$) is a vector of the reciprocal lattice.

When one derives the Born approximation of the DDSCS starting with such fast electron wave functions, a sum of two kinds of terms is obtained: direct terms (DFFs) as in the plane wave Born approximation (eq. 5.1), and interference terms (MDFFs). Each of them is defined by two wave vector transfers, thus they are labeled $S(\vec{q}, \vec{q'}, E)$.

The MDFF can be evaluated within the single particle approximation as

$$S(\vec{q}, \vec{q'}, E) = \sum_{i,f} \langle i|e^{i\vec{q}\cdot\vec{R}}|f\rangle\langle f|e^{-i\vec{q'}\cdot\vec{R}}|i\rangle\delta(E_f - E_i - E) \tag{5.5}$$

where $|i\rangle, |f\rangle$ are the initial and final single-electron wave functions of the target electron in the crystal. In the dipole approximation this expression is reduced to eq. 5.11. For more details about calculation of MDFF see paragraph 5.5.

The wave vector transfers are $\vec{q}_{gh}^{\vec{jl}} = \vec{k}^{(l)} - \vec{k}^{(j)} + \vec{h} - \vec{g}$ and the total DDSCS will be a sum over all diads of $\vec{q}$ and $\vec{q'}$ vectors of terms

$$\frac{\partial^2\sigma}{\partial\Omega\partial E} = \frac{4\gamma^2}{a_0^2}\frac{\chi_f}{\chi_0}\sum_{\mathbf{ghg'h'}}\sum_{jlj'l'}\sum_{\mathbf{a}} X^{jlj'l'}_{\mathbf{ghg'h'}}(\vec{a})\frac{S_{\mathbf{a}}(\vec{q}, \vec{q'}, E)}{q^2 q'^2} \tag{5.6}$$

where $X^{jlj'l'}_{\mathbf{ghg'h'}}(\vec{a})$ is the product of the coefficients of the individual plane wave components of the fast electron wave functions and $\vec{a}$ labels the position of the atoms where the inelastic event can occur. The $X^{jlj'l'}_{\mathbf{ghg'h'}}(\vec{a})$ coefficients are given by dynamical diffraction theory. This will be covered in the next paragraph 5.4. The χ_f and χ_0 are the magnitudes of wave vectors outside the crystal (in the vacuum).

The calculation is thus split into two separate tasks.

i) Calculation of the Bloch wave coefficients using the dynamical diffraction theory and identification of important terms. This task is mainly geometry dependent, although it can also contain some input from electronic structure codes, namely the Coulomb part of the crystal potential.

ii) Calculation of MDFFs requested by the dynamical diffraction theory. This part strongly depends on the electronic structure of the studied system. The final step is the summation of all terms.

Physically, this separate treatment is possible because the exchange and correlation effects of fast electrons with electrons in the sample are negligible. The fast electron wavefunction is described as a linear combination of plane waves with large $\vec{k}$-vector (of the order of $10^2\vec{G}$, where $\vec{G}$ is a reciprocal

lattice vector). The wavefunctions of electrons in the sample have (with the exception of deeply lying core states of heavy elements) much lower spatial frequencies. Therefore the overlap integrals between the fast electron and the electrons in the sample are practically zero and this makes their exchange interaction (and thus also correlations) negligible.

Further simplification of the fast electron part of the problem is possible due to negligible exchange and correlation effects of fast electrons among themselves. Even for high-brilliance electron sources in modern electron microscopes the density of fast electrons in the sample is extremely low. For example for a Tecnai F20, the TEM used for most of the experiments reported in this work, in the experimental setup described in the following chapters a probe current of the order of 1 μA is measured. This corresponds to the passage of $6{\cdot}10^{12}$ electrons per second or one electron every $1.6{\cdot}10^{-13}$ s. As the speed v of a 200 keV electron is 2.086 $\cdot 10^8$ m/s (70% of the speed of light), this means that the average distance between the fast electrons is $\approx 30\mu$m, much larger than the typical thickness of the sample. However electrons are wave packets with a characteristic coherence length λ_c, which can be thought of as the spatial extension of the packet in the direction of propagation.

$$\lambda_c = \frac{hv}{\Delta E} \tag{5.7}$$

where ΔE is the energy spread of the electron gun [15]. For a 200 keV field emission microscope (with $\Delta E = 0.7$ eV) $\lambda_c = 1.2$ μm, one order of magnitude smaller than their average separation. This allows to transform the problem into a single-electron one, where the fast electron moves in the crystal potential - a basis of the dynamical diffraction theory.

5.2 Equivalence between electrons and photons

The equations describing the scattering process in EELS and the absorption of a photon in XAS, within the dipole approximation, are remarkably similar [1]. In EELS, the DDSCS is given by:

$$\frac{\partial^2\sigma}{\partial E\partial\Omega} = \sum_{i,f} \frac{4\gamma^2}{a_0^2 q^4}\frac{k_f}{k_i}\frac{1}{q^2}\left|\langle f|\vec{q}\cdot\vec{R}|i\rangle\right|^2\delta(E_i - E_f + E). \tag{5.8}$$

with $\vec{q} = \vec{k_f} - \vec{k_i}$ is the wave vector transfer, $\vec{R}$ is the quantum mechanical position operator and $|i\rangle$ and $|f\rangle$ are the initial and final states (in one electron approximation) of the target electron with energies E_i and E_f respectively (fig 5.1).

For XAS the absorption cross-section is:

$$\sigma \propto \omega \sum_{i,f} |\langle f|\vec{e}\cdot\vec{R}|i\rangle|^2 \, \delta(E + E_i - E_f) \tag{5.9}$$

where ω is the photon angular frequency and $\vec{e}$ the polarization vector (the direction of oscillation of the associated electric field, as defined in paragraph 3.1). From equations 5.8 and 5.9 it is clear that within the dipole approximation the polarization vector $\vec{e}$ in x-ray absorption spectroscopy is formally equivalent to the direction of the momentum transfer $\hbar\vec{q}$ in inelastic electron scattering. It is then to be expected that XAS spectra closely resemble EELS spectra. This equivalence in the formalism can be understood when one realizes that in both cases the driving agent for transitions is an electric field $\vec{E}$ (fig. 5.1). This oscillating field of the photon or of the closely passing electron acts directly onto the electrons of the absorbing atom and changes the charge distribution in the direction of the field.

Linear dichroism can be measured in angle resolved EELS: the loss spectrum depends on the direction of the selected wave vector transfer $\vec{q}$. Such measurements have been performed on many single crystals; traditionally the effect has come to be known as EELS anisotropy rather than linear dichroism although it is exactly the same. The details have been described elsewhere [51, 56]. EELS experiments were done, *e. g.* in h-BN [56, 57, 58], in AlB_2 [59] and in V_2O_5 [60]. Linear *magnetic* dichroism experiments in the TEM were reported for hematite [61, 62].

The physics of the XMCD effect can be understood when taking into consideration the electric field corresponding to the polarization vector $\vec{e} \pm i\vec{e'}$ with $\vec{e} \perp \vec{e'}$ of a circularly polarized photon. As before, the imaginary unit i signifies a phase shift of $\pm\pi/2$ between the two perpendicular polarizations. At the position of an ionized atom this field will rotate clockwise or counterclockwise; at resonance the frequency will be exactly that for forcing an electron from the ground state into an excited state (for convenience a transition $s \rightarrow p$ is taken as example) that rotates in phase with the electric field; quantum mechanically, the final p state is $|l = 1, m = \pm 1\rangle$ *i.e.* the angular part of the wave function will have the symmetry of the $Y_1^{\pm 1}$ spherical harmonic function, obeying the selection rule $\Delta m = \pm 1$. That this

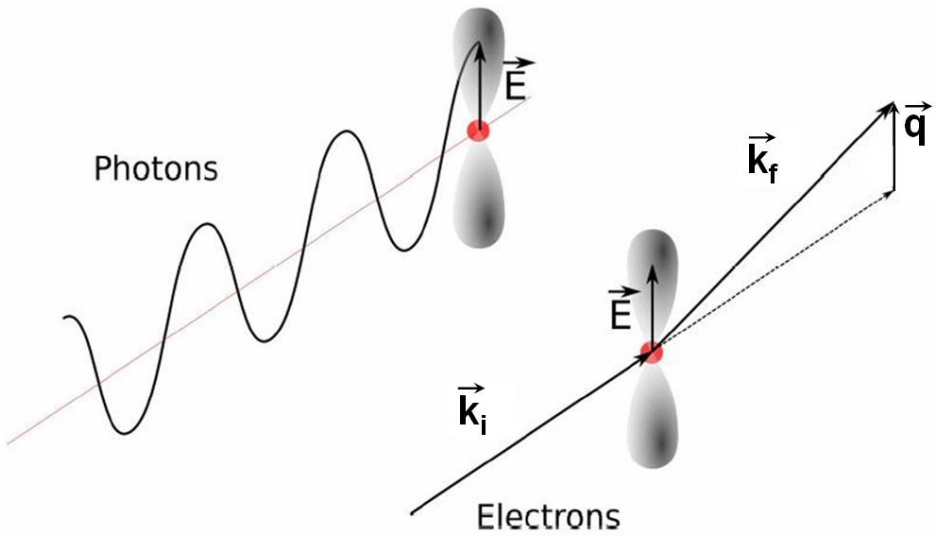

Figure 5.1: In photon absorption $\vec{E}$ is parallel to the polarization vector $\vec{e}$ whereas in inelastic electron scattering $\vec{E}$ is parallel to the momentum transfer $\hbar\vec{q}$ (the field is longitudinal because the interaction is largely Coulombic). Since the charges are polarized in the direction of the electric field, an $s \rightarrow p$ transition will select a final orbital with its main axis parallel to $\vec{q}$. This is a particular case of the (electric) dipole selection rule for optical transitions. Figure from Ref. [55]

orbital corresponds to a rotating final state can be seen if time dependence is introduced: the wave function is now $\psi \propto e^{i\omega t}e^{\pm i\phi m} = e^{i(\omega t \pm \phi m)}$ with ϕ the azimuthal angle in a spherical coordinate system. This corresponds to a running wave in the angle ϕ quite similar to a running plane wave $e^{i(\omega t - kx)}$.

The analogy to an absorption experiment with circularly polarized photons is seen when comparing the polarization vector $\vec{e} + i \cdot \vec{e'}$ with $\vec{e} \perp \vec{e'}$ and the momentum transfer $\vec{q} + i \cdot \vec{q'}$ with $\vec{q} \perp \vec{q'}$ for electrons. Also for the electron the imaginary unit describes a phase shift of $\pm\pi/2$ between the vertical and horizontal electric field components; in other words, the two incident electron plane waves must be shifted relative to each other by $\pm\lambda/4$, which makes a phase difference of exactly $\pm k\lambda/4 = \pm\pi/2$. This corresponds to the idealized case of two coherent incident plane waves of equal amplitudes. The experimental setup equivalent to this polarization will be illustrated in section 5.3 and its implementation in chapter 6.

Replacing $\vec{q}$ by $\vec{q} + i\vec{q'}$ and multiplying out the squared term, eq. 5.8 becomes:

$$\begin{aligned}\frac{\partial^2\sigma}{\partial E \partial\Omega} &= \frac{4\gamma^2}{a_0^2}\frac{k_f}{k_i}\sum_{i,f}\Big[\frac{1}{q^4}\big|\langle f|\vec{q}\cdot\vec{R}|i\rangle\big|^2 + \frac{1}{q'^4}\big|\langle f|\vec{q'}\cdot\vec{R}|i\rangle\big|^2 + \\ &- \frac{1}{q^2q'^2}\langle f|\vec{q}\cdot\vec{R}|i\rangle\langle i|i\vec{q'}\cdot\vec{R}|f\rangle + \\ &+ \frac{1}{q^2q'^2}\langle f|i\vec{q'}\cdot\vec{R}|i\rangle\langle i|\vec{q}\cdot\vec{R}|f\rangle\Big]\delta(E_i - E_f + E). \qquad (5.10)\end{aligned}$$

The first two terms in brackets are DFFs, denoted by $S(\vec{q}, E)$. They describe inelastic scattering of an incident plane wave into an outgoing plane wave with wave vector transfer $\vec{q}$ and energy loss E. They appear in angle resolved EELS and would produce directional dependence of spectra in anisotropic materials.

The last two terms in brackets are genuine inelastic interference terms. They are called MDFFs [54] and usually denoted $S(\vec{q}, \vec{q'}, E)$. In dipole approximation, they are thus defined as (compare with the general expression, eq. 5.5):

$$S(\vec{q}, \vec{q'}, E) = \sum_{i,f}\langle f|\vec{q}\cdot\vec{R}|i\rangle\langle i|\vec{q'}\cdot\vec{R}|f\rangle\delta(E_i - E_f + E). \qquad (5.11)$$

The situation is very similar to the double slit experiment where a coupling term between plane waves with wave vectors $\vec{q}$ and $\vec{q'}$ gives rise to

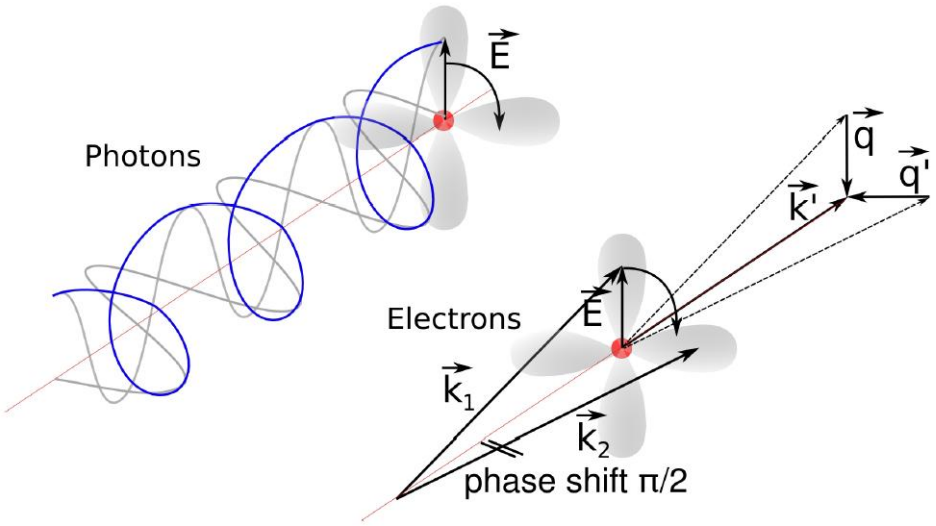

Figure 5.2: The equivalence between photons and electrons can be understood by invoking the electric field which is the driving agent for chiral transitions: in photon absorption, the circular polarization creates a rotating electric field at the atom position. This rotating field increases (or decreases, depending on the polarization) the magnetic quantum number m by 1. Additionally to the selection rule $\Delta l = \pm 1$ (in the figure realized by a transition $s \rightarrow p$) the selection rule $\Delta m = \pm 1$ for the magnetic quantum number applies. Figure from Ref. [55]

interference fringes [63]. The interference can change the intensity of an ionization edge; for example, interference between Bragg scattered waves in a crystal is the origin of the inelastic channeling effect and is the basis for the ALCHEMI and ELCE techniques [40, 41]. It was used to select transitions to particular antibonding orbitals in rutile [64, 51]. The MDFF relates to the off-diagonal elements of the probe electron density matrix after inelastic scattering [65]. Techniques exploiting the MDFF were used to detect dipole-forbidden transitions in the silicon L-edge [66], to study symmetry selected final state orbitals [67], and to investigate the localization and correlation in a solid state plasma [68]. Up to now, the relationship of the MDFF to circular dichroism passed unnoticed, because an EELS experiment invoking two coherent plane electron waves with a phase shift of $\pi/2$ was not considered to have any practical consequence.

Eq. 5.11 shows that the MDFF collapses into DFF for $\vec{q} = \vec{q'}$. The MDFF obeys several symmetry relations.

$$S(\vec{q}, \vec{q'}, E) = S^*(\vec{q'}, \vec{q}, E)$$

holds always. Consequently, the diagonal elements $S(\vec{q}, \vec{q}, E)$ (*i.e.* the DFFs) are real. The off-diagonal elements ($\vec{q} \neq \vec{q'}$) are in general complex. When the crystal has an inversion center then

$$S(\vec{q}, \vec{q'}, E) = S(-\vec{q}, -\vec{q'}, E).$$

When time inversion symmetry holds,

$$S(\vec{q}, \vec{q'}, E) = S(-\vec{q'}, -\vec{q}, E).$$

When both time inversion *and* spatial inversion symmetry are present,

$$S(\vec{q}, \vec{q'}, E) = S(-\vec{q'}, -\vec{q}, E) = S(\vec{q'}, \vec{q}, E) = S^*(\vec{q}, \vec{q'}, E)$$

and all elements are real. In this case the target system does not have any chirality and circular dichroic effects are not expected. This is important since time inversion symmetry is broken in the presence of magnetic moments, due to their pseudo-vectorial nature. Indeed it is possible to demonstrate that the chiral signal is closely related to the imaginary part of the MDFF.

The cross section, eq. 5.10 can be written in a simpler form:

$$\frac{\partial^2 \sigma}{\partial E \partial \Omega} = \frac{4\gamma^2}{a_0^2} \frac{k_f}{k_i} \left\{ \frac{S(\vec{q}, E)}{q^4} + \frac{S(\vec{q'}, E)}{q'^4} + 2\Im[\frac{S(\vec{q}, \vec{q'}, E)}{q^2 q'^2}] \right\}. \qquad (5.12)$$

In general the two plane waves will have different, complex amplitudes A_1 and A_2. Experimentally, this situation is approximated in electron diffraction by the two-beam case, the most important plane waves being the incident one and a single Bragg scattered wave.

The scattered intensity is then [69]

$$\frac{\partial^2 I(k_i,k_f)}{\partial E \partial \Omega} = \frac{4\gamma^2}{a_0^2}\frac{k_f}{k_i}\big(|A_1|^2\frac{S(\vec{q},E)}{q^4} + |A_2|^2\frac{S(\vec{q}',E)}{q'^4} + 2\Im[A_1 A_2^* \frac{S(\vec{q},\vec{q}',E)}{q^2 q'^2}]\big). \tag{5.13}$$

If one considers the three components (r_1, r_2, r_3) of the position vector operator $\vec{R}$ of the one-electron scatterer with initial and final wave functions $|i\rangle$, $|f\rangle$, it is possible to use the matrix elements

$$r_{jk} = \sum_{if} \langle i|r_j|f\rangle\langle f|r_k|i\rangle \delta(E + E_i - E_f) \tag{5.14}$$

of the transition matrix $\hat{R} = \{r_{jk}\}$ to rewrite eq. 5.11 as

$$S(\vec{q},\vec{q}',E)_{dip} = \sum_{jk} q_j r_{jk} q'_k = \underbrace{\sum_{j=k} q_j r_{jj} q'_j}_{A} + \underbrace{\sum_{j\neq k} q_j r_{jk} q'_k}_{B}. \tag{5.15}$$

Replacing the space operators r_j by their spherical components

$$r_1 = -\frac{1}{\sqrt{2}}(R_+ - R_-) \tag{5.16}$$

$$r_2 = \frac{i}{\sqrt{2}}(R_+ + R_-) \tag{5.17}$$

$$r_3 = R_0 \tag{5.18}$$

will help in analyzing the selection rules for the matrix elements such as r_{jk} for $j = k = 1$:

$$r_{11} = \frac{1}{2}(r_{++} + r_{--}) - \Re[r_{+-}] \tag{5.19}$$

where the transition matrix elements in terms of the spherical components $R_{+,-,0}$ are defined as

$$\mathrm{r}_{++} = \sum_{if} \langle i|R_+|f\rangle\langle f|R_+|i\rangle \delta(E + E_i - E_f) \tag{5.20}$$

and similar for all other combinations.

The Wigner-Eckart theorem can be now invoked. It states that the matrix element between states of well defined angular momentum $|njm\rangle$ of the p component of a generic spherical tensor T^k_p of rank k is the product of a number independent of m and characteristic of the tensor (called the reduced matrix element) and a 3j symbol that describes alone the angular dependence of the matrix element:

$$\langle njm|T^k_p|n'j'm'\rangle = \langle nj||T^k||n'j'\rangle \begin{pmatrix} J' & k & J \\ -m' & p & m \end{pmatrix}. \tag{5.21}$$

In the case of $R_{+,0,-}$, $k = 1$ and $p = 1, 0, -1$. One of the properties of the 3j symbols is that they are zero unless $m + p - m' = 0$. This means that when considering a particular transition between states with a well defined angular momentum (such as $2p \rightarrow 3d$ transitions, with fixed m and m') only one of the matrix elements associated with $R_{+,0,-}$ can be non-zero and every cross term in eq. 5.19 vanishes. This gives:

$$\begin{aligned}
r_{11} &= \frac{1}{2}(r_{++} + r_{--}) && (5.22)\\
r_{22} &= \frac{1}{2}(r_{++} + r_{--}) && (5.23)\\
r_{33} &= r_{00} && (5.24)\\
r_{12} &= -\frac{i}{2}(r_{++} - r_{--}) && (5.25)\\
r_{13} &= 0 && (5.26)\\
r_{23} &= 0 && (5.27)
\end{aligned}$$

The two terms A and B in eq. 5.15 can be then rewritten as:

$$\begin{aligned}
A &= q_1 r_{11} q'_1 + q_2 r_{22} q'_2 + q_3 r_{33} q'_3 && (5.28)\\
&= \frac{1}{2}(r_{++} + r_{--})(q_1 q'_1 + q_2 q'_2) + r_{00} q_3 q'_3 \\
B &= q_1 r_{12} q'_2 + q_2 r_{21} q'_1 = \frac{i}{2}(r_{++} - r_{--})(q_2 q'_1 - q_1 q'_2) && (5.29)
\end{aligned}$$

thus they represent respectively the real and imaginary part of the MDFF. For isotropic systems the transition matrix degenerates to a quantity proportional to the unity matrix [69] because $r_{++} = r_{--} = r_{00}$. This case was

discussed in the context of ionization fine structure and dynamical diffraction [64, 65].

The MDFF (eq. 5.15) can be written in a different form when one assigns the magnetic field direction as the positive r_3 axis (which in our case is the TEM optical axis) and decomposes $\vec{q} = (\vec{q}_\perp, q_3)$:

$$S(\vec{q}, \vec{q}', E)_{dip} = \frac{1}{2}(\mathrm{r}_{++} + \mathrm{r}_{--})\, \vec{q}_\perp \cdot \vec{q}_\perp{}' + \mathrm{r}_{00}\, q_3 q_3' + \\ + \frac{i}{2}(\mathrm{r}_{++} - \mathrm{r}_{--})\, (\vec{q}_\perp \times \vec{q}_\perp{}') \cdot \vec{e}_3 \tag{5.30}$$

where $\vec{e}_3$ is the unit vector in direction of the r_3 axis. All matrix elements and vector components are real in eq. 5.30. In this form the MDFF is separated into a real component proportional to the scalar product of the wave vector transfers $\vec{q}_\perp$, $\vec{q}'_\perp$ and an imaginary part proportional to their vector product. Starting from eq 5.9 and proceeding in a manner analogous to what has been done for electron scattering, it is possible to calculate the absorption cross section for a generic x-ray polarization obtaining:

$$I_{XAS} \propto C_1(\vec{e'} \cdot \vec{e}) + iC_2 \vec{m} \cdot (\vec{e'} \times \vec{e}) \tag{5.31}$$

where $\vec{m}$ is the direction of the magnetic moment and C_i are resonant terms describing chiral transitions [25]. Alternatively, the Stokes parameters can be used to replace the Jones vector, with $\sqrt{S_1^2 + S_2^2}$ describing the mean photon linear polarization and S_3 the mean photon helicity).

It can be noted that the imaginary part vanishes if the magnetic transitions ($\Delta m = \pm 1$) are degenerate. Only when the presence of a magnetic field in r_3 direction lifts the m-degeneracy will an effect become visible. For a transition with fixed energy loss E the operators R_+ and R_- will then contribute with different oscillator strengths, and the MDFF in eq. 5.30 will acquire an imaginary part. Its sign depends on which transitions are allowed by the selection rules.

The imaginary part can be interpreted as the difference in probability to change the magnetic quantum number m by ± 1. It thus describes the difference in response of the system to LCP and RCP electromagnetic fields. An imaginary part of the MDFF signifies that time inversion symmetry is broken. In fact this symmetry breaking relates to the angular momentum operator. Under time inversion its direction is reversed. In the presence of a magnetic field this is no longer a symmetry operation.

From what has been demonstrated so far it appears evident that the equivalence between electron scattering and photon absorption allows the definition of the equivalent of the Jones vector for the *electron virtual polarization*. This means that the present discussion can be extended to the more general case of any pair $\vec{q}, \vec{q'}$ by use of the equivalent Jones vector.

The scattering vector $\vec{q}_\perp$ in the diffraction plane is perpendicular to the magnetic field vector. It is reasonable to assume that the magnetic moments of the scatterer are aligned parallel to the optical axis r_3 in the strong magnetic field ($\approx$ 2 T) of the objective lens of the microscope. One can now evaluate the scattered intensity for specimens showing magnetic circular dichroism.

If in eq. 5.13 one writes the phase shift ϕ explicitly as

$$A_1 A_2^* = |A_1||A_2| \cdot e^{-i\phi}, \tag{5.32}$$

then a phase shift $\phi \neq n\pi$ between the two incident plane waves is needed in order to activate the imaginary part of the MDFF. A phase shift of $\pm\pi/2$ is recommended since in this case the real part of the MDFF disappears in eq. 5.13 and only the imaginary part survives. In a two-beam case with such a phase shift the pseudovector part contributes with its full magnitude and gives rise to an asymmetry in the scattering cross section of a magnetic transition such as the L edges of the ferromagnetic *d*-metals.

It appears then clear that the chiral transitions that give rise to the XMCD effect have their counterpart in the MDFF for inelastic electron scattering, whose evaluation will be described in paragraph 5.5. Since this quantity can be measured in the TEM under particular scattering conditions, it was predicted [1] that the counterpart of XMCD experiments should be possible in the electron microscope, without using polarized electron sources.

5.3 Basic geometry for EMCD

Four conditions are required to perform an EMCD experiment: 1) two coherent electron waves must exist so that two simultaneous momentum transfers can occur; 2) the two momentum transfers must not be parallel (perpendicular in the ideal case); 3) they must not be in phase (with a phase shift of $\pi/2$ being the optimal condition); 4) there should be a mechanism to change the helicity of the excitation. These conditions are summarized in figure 5.3.

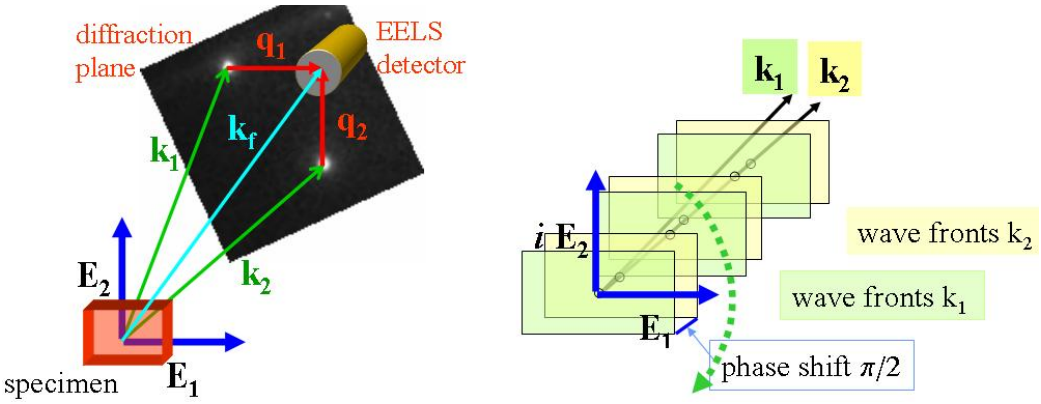

Figure 5.3: Scattering geometry for the EMCD experiment. Two incident plane waves, with wave vectors $\vec{k}_1$ and $\vec{k}_2$, produce each an oscillating electric field (E_1 and E_2) at the atom. An aperture is then placed in the diffraction plane to select the final scattering direction ($\vec{k}_f$) so that $\vec{q}_1$ and $\vec{q}_2$ are perpendicular to each other. When the phase shift between the two incident waves is set to $\pi/2$ the total electric field at the atomic site is rotating (also compare with fig. 5.2). Figure from Ref. [70]

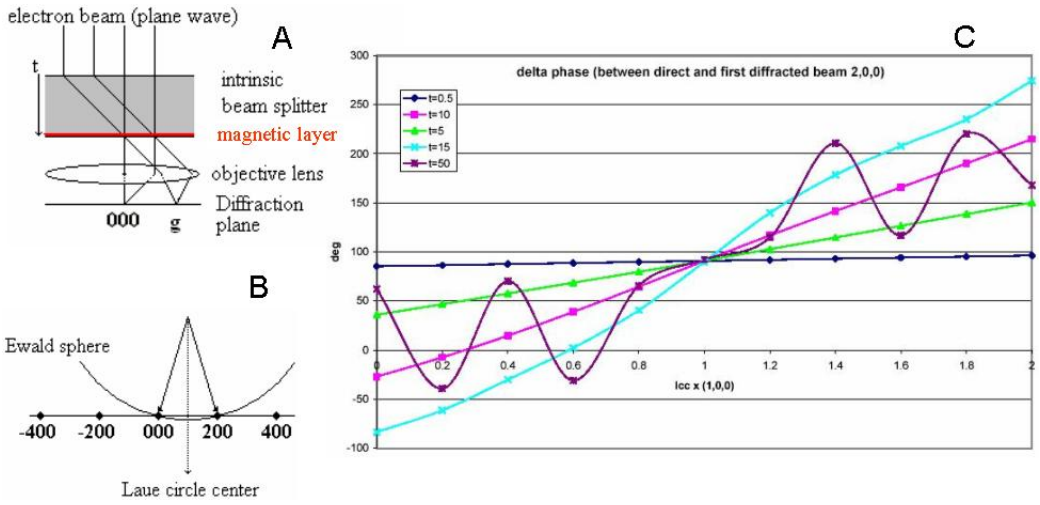

Figure 5.4: **A**: in the intrinsic method a crystalline specimen is used as beam splitter. The sample can be seen as composed by two parts: a first layer of thickness t, where the chirality of the electron beam is set, and the target magnetic layer where the ionization process occurs. **B**: the Laue Circle Center (LCC) is a convenient way to indicate the tilt of the incoming electron beam with respect to the crystal. It is defined [15] as the projection, on the diffraction plane, of the center of the Ewald's sphere, *i.e.* the sphere having the incident $\vec{k_i}$ vector as its radius (diffraction points are strongly excited only if they lay close to the surface of the Ewald's sphere). **C**: plot of the phase shift between the direct and the first diffracted beam (2,0,0 of fcc Nickel) as a function of the tilt of the incident beam and for different values of the thickness t (in nm) of the sample. Figure from Ref. [70].

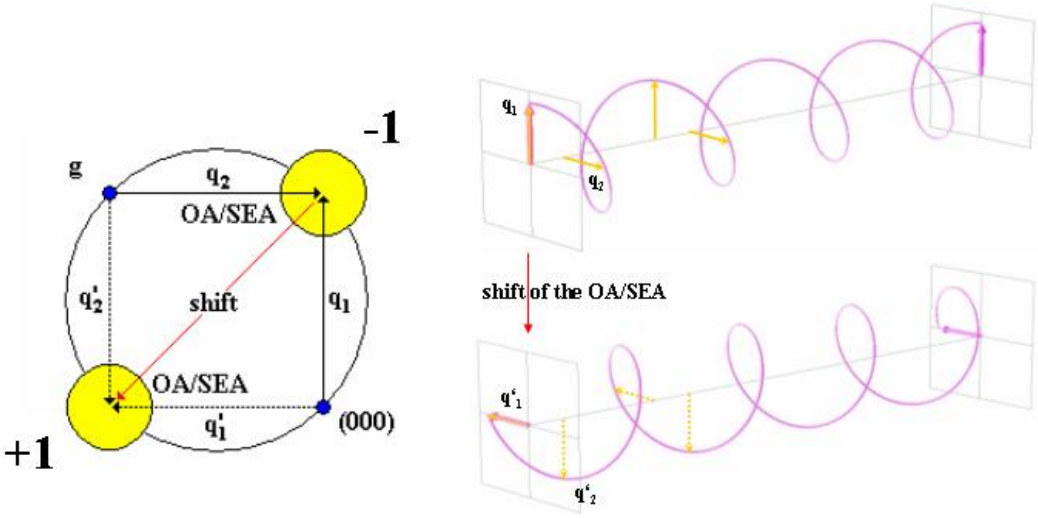

Figure 5.5: Chirality of the electron excitation in an EMCD experiment. The Thales circle is constructed in the diffraction plane by taking as its diameter the segment connecting the 000 and g spot. One achieves the TEM equivalent of circular polarization when the OA (or the SEA) is located on the Thales circle in such a way that $|\vec{q}_1| = |\vec{q}_2|$ and when their phase shift is set to $\pm\pi/2$. The helicity of the virtual photon absorbed in the EMCD process changes its sign when the OA (or SEA) is shifted to the symmetric position on the Thales circle. Figure from Ref. [70]

There are several methods to obtain two electron beams in the TEM, however so far only the so called intrinsic way has been successful in obtaining EMCD spectra. In this method a crystalline sample is used to split the beam via Bragg scattering. When the electron wave enters the crystal it undergoes a decomposition into Bloch waves, whose amplitude and phase can be calculated within the framework of the Bloch theory (detailed in the following paragraphs) and can be controlled by setting the boundary conditions (namely beam tilt and specimen thickness) to appropriate values. The sample has to be tilted a few degrees away from a direction of high symmetry (called Zone Axis) so that only one or two Bragg spots besides the direct (000) beam are strongly excited (this situation is called respectively two-beam case and three-beam case). This is exemplified in fig. 5.4 for an ideal two-beam case: the fine tilt of the beam is determined by the Laue Circle Center (LCC), which is the projection of the Ewald's sphere on the diffraction plane. The appropriate tilt and thickness are chosen to set the phase shift between the Bloch waves to the desired value (for example 90 degrees).

The advantage of the intrinsic method is threefold: it provides two simultaneous momentum transfers (two Bragg scattered beams being excited); the proper variation of the boundary conditions is a mean to control their phase shift; the phase shift is the same for all atoms at the same depth and occupying the same elementary cell position because Bloch waves have the same periodicity of the crystal lattice (the phase is then locked to the lattice position). Therefore the intrinsic method fulfills conditions 1 and 3 at the same time. Condition 2 can be reached by a suitable selection of the scattering direction $\vec{k}_f$, placing either the Objective Aperture (OA) or the Spectrometer Entrance Aperture (SEA) in the diffraction plane, so that $\vec{q} \perp \vec{q}'$. The ensemble of points in the diffraction plane fulfilling this conditions describes a circle (here referred to as *Thales circle*), having the segment connecting the two Bragg spots as one of its diameters. The diameter perpendicular to that one has as extremities the only two points for which the further condition $q = q'$ holds. As $\vec{q}$ and $\vec{q}'$ now play the roles of Jones vector for the equivalent electron polarization, these two points represent the case of circular polarization (for any other point in the circle elliptical polarization is obtained even with a phase shift of 90 degrees). This also provides a very simple way to change the helicity (condition 4) as illustrated in fig. 5.5. The simple picture provided in fig 5.4 is an extreme simplification of the dynamical diffraction of the electron by the crystal lattice and is presented only for its heuristic

value. A more detailed discussion should include Bragg scattering after the ionization event (which can occur at any depth inside the specimen, not just at the lowermost layer) and take into account all other excited beams of relevance.

5.4 Dynamical electron diffraction theory

The formalism described here is a generalization of the formalism presented in Ref. [65, 52] extending it beyond systematic row approximation by including also higher-order Laue zones (HOLZ). The extension to HOLZ is performed along lines presented in Refs. [71, 72]. The high-energy Laue case is assumed, *i.e.* back-reflection and back-diffraction can be safely neglected.

The Bloch wave vectors of the electron after entering the crystal fulfill the continuity condition

$$\vec{k}^{(j)} = \vec{\chi} + \gamma^{(j)}\vec{n} \tag{5.33}$$

where $\vec{n}$ is the unit vector normal to the crystal surface and χ is the wave vector of the incoming electron. Only the wave vector component normal to the surface can change.

Expanding the wave function of the fast electron into a linear combination of plane waves and substituting it into the Schrödinger equation one obtains the secular equation [71]

$$\sum_{\mathbf{g}} \left[\left(K^2 - (\vec{k}^{(j)} + \vec{g})^2 \right) + \sum_{\mathbf{h}\neq 0} U_{\mathbf{h}} C^{(j)}_{\mathbf{g}-\mathbf{h}} \right] e^{i(\vec{k}^{(j)}+\vec{g})\cdot\vec{r}} = 0 \tag{5.34}$$

where $K^2 = U_0 + 2meE/\hbar^2$, m is the electron mass and e its charge, $U_{\mathbf{g}} = 2meV_{\mathbf{g}}/\hbar^2$ where $V_{\mathbf{g}}$ are the Fourier components of the crystal potential, which can be either calculated *ab initio* or obtained from the tabulated forms of the potential [73, 74]. The WIEN2k [75] package can calculate x-ray structure factors. This code is a state-of-the-art implementation of the full-potential linearized augmented plane waves method. By supplying the potential instead of the charge density it is possible to use the same code to calculate the electron structure factors. It can be shown [71, 76] that in the high energy limit the secular equation, which is a quadratic eigenvalue problem in $\gamma^{(j)}$, can be reduced to a linear eigenvalue problem $\mathbf{AC}^{(j)} = \gamma^{(j)}\mathbf{C}^{(j)}$ where $\mathbf{A}$ is a non-Hermitean matrix [72, 76]

$$A_{\mathbf{gh}} = \frac{K^2 - (\vec{\chi} + \vec{g})^2}{2(\vec{\chi} + \vec{g}) \cdot \vec{n}} \delta_{\mathbf{gh}} + (1 - \delta_{\mathbf{gh}}) \frac{U_{\mathbf{g-h}}}{2(\vec{\chi} + \vec{g}) \cdot \vec{n}}. \tag{5.35}$$

This eigenvalue problem can be transformed into a Hermitean one using a diagonal matrix $\mathbf{D}$ with elements

$$\mathbf{D}_{\mathbf{gh}} = \delta_{\mathbf{gh}} \left[1 + \frac{\vec{g} \cdot \vec{n}}{\vec{\chi} \cdot \vec{n}} \right]. \tag{5.36}$$

Then the eigenvalue problem is equivalent to $(\mathbf{D}^{1/2}\mathbf{A}\mathbf{D}^{-1/2})(\mathbf{D}^{1/2}\mathbf{C}^{(j)}) = \gamma^{(j)}(\mathbf{D}^{1/2}\mathbf{C}^{(j)})$ or $\tilde{\mathbf{A}}\tilde{\mathbf{C}}^{(j)} = \gamma^{(j)}\tilde{\mathbf{C}}^{(j)}$, where the matrix $\tilde{\mathbf{A}}$ is Hermitean

$$\begin{aligned} \tilde{A}_{\mathbf{gh}} &= \frac{K^2 - (\vec{\chi} + \vec{g})^2}{2(\vec{\chi} + \vec{g}) \cdot \vec{n}} \delta_{\mathbf{gh}} + \\ &+ (1 - \delta_{\mathbf{gh}}) \frac{U_{\mathbf{g-h}}}{2\sqrt{[(\vec{\chi} + \vec{g}) \cdot \vec{n}][(\vec{\chi} + \vec{h}) \cdot \vec{n}]}} \end{aligned} \tag{5.37}$$

and the original Bloch wave coefficients can be retrieved using the relation

$$C_{\mathbf{g}}^{(j)} = \tilde{C}_{\mathbf{g}}^{(j)} \Bigg/ \sqrt{1 + \frac{\vec{g} \cdot \vec{n}}{\vec{\chi} \cdot \vec{n}}} \tag{5.38}$$

By solving this eigenvalue problem one obtains the fast electron wave function as a linear combination of eigenfunctions as given in eq. 5.3. To obtain values for $\epsilon^{(j)}$ boundary conditions have to be imposed, namely that the electron is described by a single plane wave at the crystal surfaces. The crystal surface is a plane defined by the scalar product $\vec{n} \cdot \vec{r} = t_0$. Then the boundary condition (in the high energy limit) leads to the following condition [71]

$$\epsilon^{(j)} = C_{\mathbf{0}}^{(j)\star} e^{-i\gamma^{(j)} t_0} \tag{5.39}$$

It is easy to verify that

$$\begin{aligned}
&\psi(\vec{r})|_{\vec{n}\cdot\vec{r}=t_0} = \\
&= \sum_{j\mathbf{g}} C_{\mathbf{0}}^{(j)\star} C_{\mathbf{g}}^{(j)} e^{i(\vec{k}^{(j)}+\vec{g})\cdot\vec{r}} e^{-i\gamma^{(j)}t_0} \\
&= \sum_{\mathbf{g}} e^{i(\vec{\chi}+\vec{g})\cdot\vec{r}} \sum_{j} e^{i\gamma^{(j)}\vec{n}\cdot\vec{r}} e^{-i\gamma^{(j)}t_0} C_{\mathbf{0}}^{(j)\star} C_{\mathbf{g}}^{(j)} \\
&= \sum_{\mathbf{g}} e^{i(\vec{\chi}+\vec{g})\cdot\vec{r}} \sum_{j} C_{\mathbf{0}}^{(j)\star} C_{\mathbf{g}}^{(j)} \\
&= \sum_{\mathbf{g}} e^{i(\vec{\chi}+\vec{g})\cdot\vec{r}} \delta_{\mathbf{0g}} \Big/ \sqrt{1+\frac{\vec{g}\cdot\vec{n}}{\vec{\chi}\cdot\vec{n}}} \\
&= e^{i\vec{\chi}\cdot\vec{r}}|_{\vec{n}\cdot\vec{r}=t_0}
\end{aligned} \tag{5.40}$$

as required by the boundary condition. The continuity condition, eq. 5.33, was used and the completeness relation for the Bloch coefficients

$$\begin{aligned}
\delta_{\mathbf{gh}} &= \sum_{j} \tilde{C}_{\mathbf{g}}^{(j)*} \tilde{C}_{\mathbf{h}}^{(j)} = \\
&= \sqrt{\left[1+\frac{\vec{g}\cdot\vec{n}}{\vec{\chi}\cdot\vec{n}}\right]\left[1+\frac{\vec{h}\cdot\vec{n}}{\vec{\chi}\cdot\vec{n}}\right]} \sum_{j} C_{\mathbf{g}}^{(j)*} C_{\mathbf{h}}^{(j)}.
\end{aligned} \tag{5.41}$$

Therefore the wave function of the fast moving electron in the crystal, which becomes a single plane wave at $\vec{n}\cdot\vec{r} = t_0$, is given by the following expression:

$$\psi(\mathbf{r}) = \sum_{j\mathbf{g}} C_{\mathbf{0}}^{(j)\star} C_{\mathbf{g}}^{(j)} e^{i\gamma^{(j)}(\vec{n}\cdot\vec{r}-t_0)} e^{i(\vec{\chi}+\vec{g})\cdot\vec{r}}. \tag{5.42}$$

The following discussion will be restricted to a particular case - a crystal with parallel surfaces. For such a crystal with normals in the direction of the z axis one can set $t_0 = 0$ for the fast electron entering the crystal and $t_0 = t$ when leaving the crystal (t is the crystal thickness).

The inelastic event leads to a change of the energy and momentum of the scattered electron. The detector position determines the observed projection of the electron wave function (Bloch field) onto a plane wave after the inelastic event. Therefore the calculation of the ELNES requires the solution of two independent eigenvalue problems describing an electron wave function before

and after the inelastic event [52, 65]. Invoking the reciprocity of the electron propagation, the outgoing wave can also be considered as a time reversed solution of the Schrödinger equation, also known as the *reciprocal wave* [77] with the source replacing the detector.

Now it is possible to identify the prefactors $X^{jlj'l'}_{\mathbf{ghg'h'}}(\vec{a})$ from eq. 5.6. For the sake of clarity $C^{(j)}_{\mathbf{g}}$ indicates the Bloch coefficients of the incoming electron and $D^{(l)}_{\mathbf{h}}$ is used for the Bloch coefficients of the outgoing electron after the inelastic scattering (obtained from the two independent eigenvalue problems). Similarly, superscript indices (j) and (l) indicate eigenvalues and Bloch-vectors for incoming and outgoing electron, respectively. One then obtains

$$\begin{aligned} X^{jlj'l'}_{\mathbf{ghg'h'}}(\vec{a}) &= C^{(j)\star}_{\mathbf{0}} C^{(j)}_{\mathbf{g}} D^{(l)}_{\mathbf{0}} D^{(l)\star}_{\mathbf{h}} \\ &\times C^{(j')}_{\mathbf{0}} C^{(j')\star}_{\mathbf{g'}} D^{(l')\star}_{\mathbf{0}} D^{(l')}_{\mathbf{h'}} \\ &\times e^{i(\gamma^{(l)}-\gamma^{(l')})t} e^{i(\vec{q}-\vec{q'})\cdot\vec{a}} \end{aligned} \tag{5.43}$$

where

$$\begin{aligned} \vec{q} &= \vec{k}^{(l)} - \vec{k}^{(j)} + \vec{h} - \vec{g} \\ \vec{q'} &= \vec{k}^{(l')} - \vec{k}^{(j')} + \vec{h'} - \vec{g'}. \end{aligned} \tag{5.44}$$

In crystals the position of each atom can be decomposed into a sum of a lattice vector and a base vector, $\vec{a} = \vec{R} + \vec{u}$. Clearly, MDFF does not depend on $\vec{R}$, but only on $\vec{u}$. It is then possible to perform analytically the sum over all lattice vectors $\vec{R}$ under the approximation that the MDFF does not depend strongly on the j, l indices. This is indeed a very good approximation, as verified by numerical simulations (see fig. 5.6).

First the summation over all lattice vectors is treated. The sum in eq. 5.6 can be separated into two terms

$$\frac{1}{N}\sum_{\mathbf{a}} e^{i(\vec{q}-\vec{q'})\cdot\vec{a}} = \frac{1}{N_{\mathbf{u}}}\sum_{\mathbf{u}} e^{i(\vec{q}-\vec{q'})\cdot\vec{u}} \frac{1}{N_{\mathbf{R}}}\sum_{\mathbf{R}} e^{i(\vec{q}-\vec{q'})\cdot\vec{R}}. \tag{5.45}$$

Since

$$\begin{aligned} \vec{q}-\vec{q'} &= [(\gamma^{(j)}-\gamma^{(j')}) - (\gamma^{(l)}-\gamma^{(l')})]\vec{n} \\ &+ \vec{h} - \vec{h'} + \vec{g'} - \vec{g} \end{aligned} \tag{5.46}$$

and the sum of $\vec{g}, \vec{h}$ is simply a reciprocal lattice vectors $\vec{G}$, which fulfills $e^{i\vec{G}\cdot\vec{R}} = 1$, it is possible to simplify the second term

$$\sum_{\mathbf{R}} e^{i(\vec{q}-\vec{q'})\cdot\vec{R}} = \sum_{\mathbf{R}} e^{i[(\gamma^{(j)}-\gamma^{(j')})-(\gamma^{(l)}-\gamma^{(l')})]\vec{n}\cdot\vec{R}}. \tag{5.47}$$

For general orientations of the vector $\vec{n}$ this sum is difficult to evaluate. In particular coordinate systems with $\vec{n} \parallel z$ and crystal axes $a, b \perp z$ this sum leads [52, 78] to

$$\sum_{\mathbf{R}} e^{i(\vec{q}-\vec{q'})\cdot\vec{R}} = N_{\mathbf{R}} e^{i\Delta t/2} \frac{\sin \Delta\frac{t}{2}}{\Delta\frac{t}{2}} \tag{5.48}$$

so that the total sum over all atomic positions is

$$\frac{1}{N}\sum_{\mathbf{a}} e^{i(\vec{q}-\vec{q'})\cdot\vec{a}} = e^{i\Delta\frac{t}{2}} \frac{\sin \Delta\frac{t}{2}}{\Delta\frac{t}{2}} \frac{1}{N_{\mathbf{u}}} \sum_{\mathbf{u}} e^{i(\vec{q}-\vec{q'})\cdot\vec{u}} \tag{5.49}$$

where $\Delta = (\gamma^{(j)} - \gamma^{(j')}) - (\gamma^{(l)} - \gamma^{(l')})$. The final expression of the DDSCS can be written as

$$\begin{aligned} \frac{4\gamma^2}{a_0^2}\frac{\chi_f}{\chi_0}\frac{\partial^2\sigma}{\partial\Omega\partial E} &= \sum_{\mathbf{ghg'h'}} \frac{1}{N_{\mathbf{u}}} \sum_{\mathbf{u}} \frac{S_{\mathbf{u}}(\vec{q}, \vec{q'}, E)}{q^2 q'^2} e^{i(\vec{q}-\vec{q'})\cdot\vec{u}} \\ &\times \sum_{jlj'l'} Y^{jlj'l'}_{\mathbf{ghg'h'}} T_{jlj'l'}(t) \end{aligned} \tag{5.50}$$

where

$$\begin{aligned} Y^{jlj'l'}_{\mathbf{ghg'h'}} &= C^{(j)\star}_{\mathbf{0}} C^{(j)}_{\mathbf{g}} D^{(l)}_{\mathbf{0}} D^{(l)\star}_{\mathbf{h}} \\ &\times C^{(j')}_{\mathbf{0}} C^{(j')\star}_{\mathbf{g'}} D^{(l')\star}_{\mathbf{0}} D^{(l')}_{\mathbf{h'}} \end{aligned} \tag{5.51}$$

depends only on the eigenvectors of the incoming and outgoing beam and

$$T_{jlj'l'}(t) = e^{i[(\gamma^{(j)}-\gamma^{(j')})+(\gamma^{(l)}-\gamma^{(l')})]\frac{t}{2}} \frac{\sin \Delta\frac{t}{2}}{\Delta\frac{t}{2}} \tag{5.52}$$

is a thickness and eigenvalue dependent function.

Perturbative treatment of the absorption can be easily introduced. Denoting by $U'_{\mathbf{g}}$ the absorptive part of the potential, within the first order perturbation theory the Bloch coefficients will not change, just the eigenvalues

will be shifted by $i\eta^{(j)}$ or $i\eta^{(l)}$ for the incoming or outgoing wave, respectively. Particular values of $\eta^{(j)}$ can be calculated using the following expression [71]

$$\eta^{(j)} = \frac{\sum_{\mathbf{g},\mathbf{h}} U'_{\mathbf{g}-\mathbf{h}} C_{\mathbf{h}}^{(j)} C_{\mathbf{g}}^{(j)\star}}{2\sum_{\mathbf{g}} C_{\mathbf{g}}^{(j)} C_{\mathbf{g}}^{(j)\star} (\vec{\chi}+\vec{g})\cdot\vec{n}} \tag{5.53}$$

and similarly for the outgoing beam.

This way the eigenvalues change from $\gamma^{(j)}$ to $\gamma^{(j)} + i\eta^{(j)}$ and Δ acquires an imaginary part. This approximate treatment of absorption thus affects only the thickness-dependent function $T_{jlj'l'}(t)$.

A few practical considerations, which were applied to the extended computer code, should be mentioned. The sum in eq. 5.50 is performed over 8 indices for every energy and thickness value. Such summation can easily grow to a huge number of terms and go beyond the computational capability of modern desktop computers. For example, if one assumes the splitting of the incoming (and outgoing) beam into only 10 plane wave components, taking into account the 10 most strongly excited Bloch waves, one would have 10^8 terms per each energy and thickness. A calculation with an energy mesh of 100 points at 100 different thicknesses would include one trillion terms and require a considerable amount of computing time. However most of these terms give a negligible contribution to the final sum. Therefore several carefully chosen cut-off conditions are required to keep the computing time reasonable without any significant degradation of the accuracy.

The first cut-off condition used is based on the Ewald's sphere construction. Only plane wave components with $\vec{k}+\vec{g}$ close to the Ewald's sphere will be excited. The strength of the excitation decreases also with decreasing crystal potential component $U_{\mathbf{g}}$. A dimensionless parameter $w_{\mathbf{g}} = s_{\mathbf{g}}\xi_{\mathbf{g}}$ - product of the excitation error and the extinction distance [71] - reflects both these criteria. Therefore one can filter the list of beams by selecting only beams with $w_{\mathbf{g}} < w_{max}$. Experience shows that in the final summation a fairly low number of beams is necessary to have a well converged results (in systematic row conditions this number is typically around 10). The convergence of the corresponding Bloch coefficients requires solving an eigenvalue problem with a much larger set of beams (several hundreds). Therefore two cut-off parameters for $w_{\mathbf{g}}$ were defined - the first for the solution of the eigenvalue problem (typically $w_{max,1}$ is between 1000 and 5000) and the second for the summation ($w_{max,2}$ typically between 50 and 100).

The second type of cut-off conditions is applied to the selection of the

Bloch waves, which enter the summation. Once the set of beams for summation is determined, this amounts to sorting the Bloch waves according to a product of their excitation $\epsilon^{(j)}$ and their norm on the subspace defined by the selected subset of beams, $C_{\mathbf{0}}^{(j)}||\mathbf{C}^{(j)}||_{\text{subsp}}$. In the systematic row conditions this value is large only for a small number of Bloch waves. Typically in the experimental geometries used for detection of EMCD one can perform a summation over less than 10 Bloch waves to have a well converged result (often 5 or 6 Bloch waves are enough).

5.5 Mixed dynamic form factor

It can be seen from eq. 5.5 that the calculation of the MDFF requires the evaluation of two matrix elements between initial and final states of the target electron. The derivation [52] of the expression for the MDFF describing a transition from core state $nl\kappa$ (n, l, κ are the main, orbital and relativistic quantum numbers, respectively) to a band state with energy E is presented in detail here. Though, note that in Ref. [52] the initial states are treated classically, which leads to somewhat different expression for MDFF giving incorrect $L_2 - L_3$ branching ratio.

The crystal is divided [67] into non-overlapping atomic spheres of radius R_{MT} and remaining interstitial region. The initial states $|i\rangle$ correspond to the core electrons of the target atom and they are fully contained in the atomic sphere. Therefore when calculating the matrix elements in eq. 5.5 only the atomic spheres need to be considered. When the effect of magnetic or exchange field is neglected, the core states can be expressed as products of radial solutions of the Kohn-Sham-Dirac equation and angular functions having the relativistic symmetry (combinations of products of the spherical harmonics $Y_l^m(\vec{r}/r)$ and the $\pm 1/2$ spinor functions). The core states are identified by the orbital number l and relativistic quantum numbers j, j_z. To calculate the radial core functions the spherical approximation for the potential is adopted. The splitting of the core states by the magnetic or exchange field is accounted for by first-order perturbation theory (the field induced mixing of states with different j is neglected). The final states $|f\rangle$ correspond to the valence states and they are computed with the full, non-spherical potential, using the second variational approach to include the spin-orbit interaction [79, 80]. As mentioned above, only the part of the valence function contained in the atomic sphere needs to be considered. It possesses

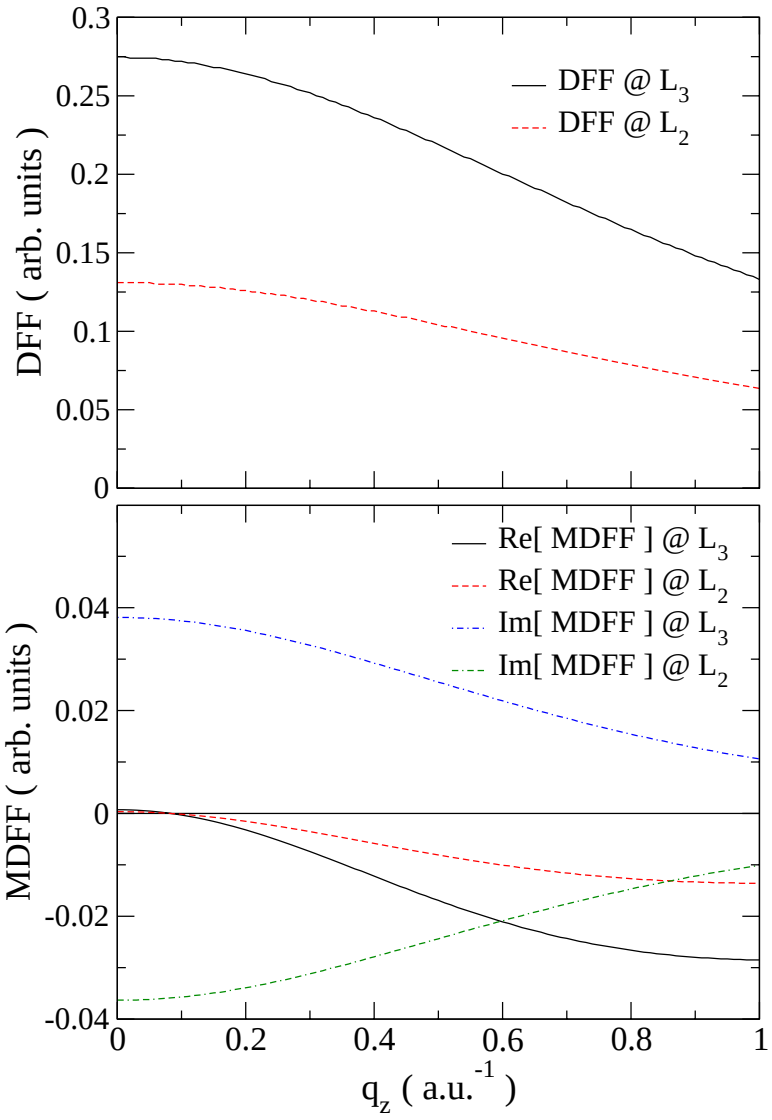

Figure 5.6: Dependence of $S(\vec{q}, E)$ (top) and $S(\vec{q}, \vec{q'}, E)$ with $\vec{q'} = \vec{G} + \vec{q}$ (bottom) on q_z (in reciprocal atomic units), calculated for the $L_{2,3}$ edge of hcp-Co, with $\vec{G} = (100)$, $q_x = -q'_x = -|G|/2$, $q_y = q'_y = |G|/2$. The ratio between values calculated at L_3 or L_2 is constant and equal to 2.1 for the real part and to -1 for the imaginary part. Figure from Ref. [4].

an atomic-like character and can be expressed as the $\vec{k}$-dependent combination of the products of radial functions, $\pm 1/2$ spinors and spherical harmonics $Y_L^M(\vec{r}/r)$. For the sake of clarity the spin states will be indicated by their magnetic quantum number only and the notation used in paragraph 3.3 is simplified by relabeling $m_l \Rightarrow m$ and $m_s \Rightarrow s$. Therefore, a generic spin state becomes:

$$|S, m_S\rangle \Rightarrow |\frac{1}{2}, s\rangle. \tag{5.54}$$

With this notation the matrix elements for practical calculations can be expressed as a product of wave functions in the $\vec{r}$-space:

$$\begin{aligned} \langle i|e^{-i\vec{q}\cdot\vec{R}}|f\rangle &= \sum_s \int d\vec{r} \sum_s \int d\vec{r'} \langle i|\vec{r}, s\rangle \langle \vec{r}, s|e^{-i\vec{q}\cdot\vec{R}}|\vec{r'}, s'\rangle \langle \vec{r'}, s'|f\rangle \\ &= \sum_s \int d\vec{r} \langle i|\vec{r}, s\rangle e^{-i\vec{q}\cdot\vec{r}} \langle \vec{r}, s|f\rangle \end{aligned} \tag{5.55}$$

For initial and final states one can use the following *Ansatz*:

$$\langle \vec{r}, s|i\rangle \rightarrow \langle \vec{r}, s|jj_z\rangle = \sum_m C^{jj_z}_{lm\frac{1}{2}s} R_{js}(r) Y_l^m(\vec{r}/r) \tag{5.56}$$

$$\langle \vec{r}, S|f\rangle \rightarrow \sum_{\nu\vec{k}} \langle \vec{r}, S|\nu\vec{k}\rangle = \sum_{LM} D_{LMS}(\nu\vec{k}) u^{E_{\nu\vec{k}}}_{LS}(r) Y_L^M(\vec{r}/r), \tag{5.57}$$

where Y_l^m are spherical harmonics, $C^{jj_z}_{lm\frac{1}{2}s}$ are Clebsch-Gordan (vector addition) coefficients, $R_{js}(r)$ is the exchange split radial wavefunction of core states, $u^E_{LS}(r)$ is the normalized radial expansion function of the valence states at energy E and $D_{LMS}(\nu\vec{k})$ is a projection of the corresponding amplitude of $\nu\vec{k}$ Bloch state onto LMS subspace.

The summations over initial and final states are in this *Ansatz* replaced by

$$\sum_i (\dots) \rightarrow \sum_{j_z} (\dots) \quad \text{and} \quad \sum_f (\dots) \rightarrow \sum_{\nu\mathbf{k}} (\dots). \tag{5.58}$$

Using the Rayleigh expansion

$$e^{i\vec{q}\cdot\vec{r}} = 4\pi \sum_{\lambda\mu} i^\lambda Y_\lambda^\mu(\vec{q}/q)^\star Y_\lambda^\mu(\vec{r}/r) j_\lambda(qr) \tag{5.59}$$

and the following notation for the resulting radial integrals

$$\langle j_\lambda(q)\rangle_{Elsj} = \int_0^{R_{MT}} dr\, r^2 u_{ls}^E(r) R_{js}(r) j_\lambda(qr) \tag{5.60}$$

the final expression becomes:

$$\begin{aligned}
&S(\vec{q},\vec{q'},E) = \\
&= \sum_{mm'}\sum_{LMS}\sum_{L'M'S'}\sum_{\lambda\mu}\sum_{\lambda'\mu'} 4\pi i^{\lambda-\lambda'}(2l+1)\sqrt{[\lambda,\lambda',L,L']} \\
&\times\ Y_\mu^\lambda(\vec{q}/q)^* Y_{\mu'}^{\lambda'}(\vec{q'}/q')\langle j_\lambda(q)\rangle_{ELSj}\langle j_{\lambda'}(q')\rangle_{EL'S'j} \\
&\times\ \begin{pmatrix} l & \lambda & L \\ 0 & 0 & 0 \end{pmatrix}\begin{pmatrix} l & \lambda' & L' \\ 0 & 0 & 0 \end{pmatrix}\begin{pmatrix} l & \lambda & L \\ -m & \mu & M \end{pmatrix}\begin{pmatrix} l & \lambda' & L' \\ -m' & \mu' & M' \end{pmatrix} \\
&\times\ \sum_{j_z}(-1)^{m+m'}(2j+1)\begin{pmatrix} l & \frac{1}{2} & j \\ m & S & -j_z \end{pmatrix}\begin{pmatrix} l & \frac{1}{2} & j \\ m' & S' & -j_z \end{pmatrix} \\
&\times\ \sum_{\nu\mathbf{k}} D_{LMS}(\nu\vec{k}) D_{L'M'S'}(\nu\vec{k})^* \delta(E + E_{nl\kappa} - E_{\nu\vec{k}})
\end{aligned} \tag{5.61}$$

where the Wigner 3j-symbols are used. The novelty of this formulation, with respect to previous treatments [56], comes from a more correct description of the core states. Here starting from a relativistic description results in the appearance of Clebsch-Gordan coefficients and an additional summation over j_z. The Clebsch-Gordan coefficients project the $|jj_z\rangle$ states into a $|lms\rangle$ basis and result in summation over spin index. Therefore both spin orientations are taken into account. When the spin-orbit interaction is present in the calculation, this formula includes also contributions from spin-crossterms as the sum over the spin indices is now correctly separated.

For evaluation of the radial integrals and Bloch state projections $D_{LMS}(\nu\vec{k})$ one can employ the Density Functional Theory [81, 82] (DFT) within the local spin density approximation [83]. It should be noted that this is just one of the possible approaches. In principle, one can employ any other method capable to provide radial parts of the wavefunctions and the energy resolved density matrix $\rho_{LMS}^{L'M'S'}(E)$, which is given in the Bloch state formulation as the last line in eq. 5.61. A fitting example would be the multiplet approach [84] or any other method better suited for correlated solids. The inclusion of the multiplet approach into this code is actually planned as the next step in the generalization of the calculations.

In paragraph 5.4 an approximation of negligible dependence of MDFF on the j, l indices (see eq. 5.46) was used. Generally, as the wave vector $\vec{k}^{(j,l)}$ for each Bloch wave changes slightly by an amount given by the corresponding eigenvalue $\gamma^{(j,l)}$, the values of q_z and q'_z would change accordingly and therefore one should not be allowed to take MDFF out of the sum over the indices j, l in the eq. 5.50. However, the change in q_z (and q'_z) induced by the eigenvalues $\gamma^{(j,l)}$ is small and can be neglected with respect to the $q_z = \chi_0 E/2E_0$ given by the energy loss E. To demonstrate this the dependence of MDFF on q_z, q'_z, for q_x and q_y corresponding to the main DFF and MDFF terms, is plotted in fig. 5.6. If q_z is given in a.u.$^{-1}$ (reciprocal atomic units, 1 a.u.= 0.529178 Å), typical values for $L_{2,3}$ edges of Fe, Co and Ni are around tenth of a.u.$^{-1}$, whereas typical values of $\gamma^{(j,l)}$ for strongly excited Bloch waves are one or two orders of magnitude smaller. Thus the approximation of a weak j, l dependence of the MDFF is well justified.

Besides $\gamma^{(j,l)}$, the other factors determining the value of q_z are the energy of the edge, *i.e.* the energy lost by the probe electron, the tilt with respect to the zone axis and whether the excited beam is in a HOLZ. These last factors have been included in the calculation. Only the variations due to $\gamma^{(j,l)}$ are neglected, thus giving rise to an error $\leq 1\%$. If a more accurate treatment would be needed, the smooth behavior of MDFF with respect to q_z would allow to use simple linear or quadratic interpolation/extrapolation methods.

As mentioned in paragraph 5.2 and explained in Refs. [3, 85], dichroism in the TEM is made possible by the analogous role that the polarization vector $\vec{e}$ and the wave vector transfer $\vec{q}$ play in the dipole approximation of the DDSCS. However the calculations reported here are not restricted to the dipole approximation, eq. 5.11, and the more complete expression eq. 5.5 is used.

To evaluate the accuracy of the dipole approximation, one can compare the dipole approximation of MDFF with the full calculation (with λ up to 3) also showing λ-diagonal components of the MDFF, fig. 5.7. Since the dominant contribution to the signal originates from (dipole allowed) $2p \rightarrow 3d$ transitions, the $\lambda = \lambda' = 1$ term nearly coincides with the total MDFF. While the dipole approximation works relatively well for the studied systems, particularly the MDFF divided by squares of momentum transfer vectors (right column of the fig. 5.7), it has significantly different asymptotic behaviors for larger $\vec{q}$-vectors. The $\lambda = \lambda' = 1$ term provides a much better approximation, which remains very accurate also in the large q region.

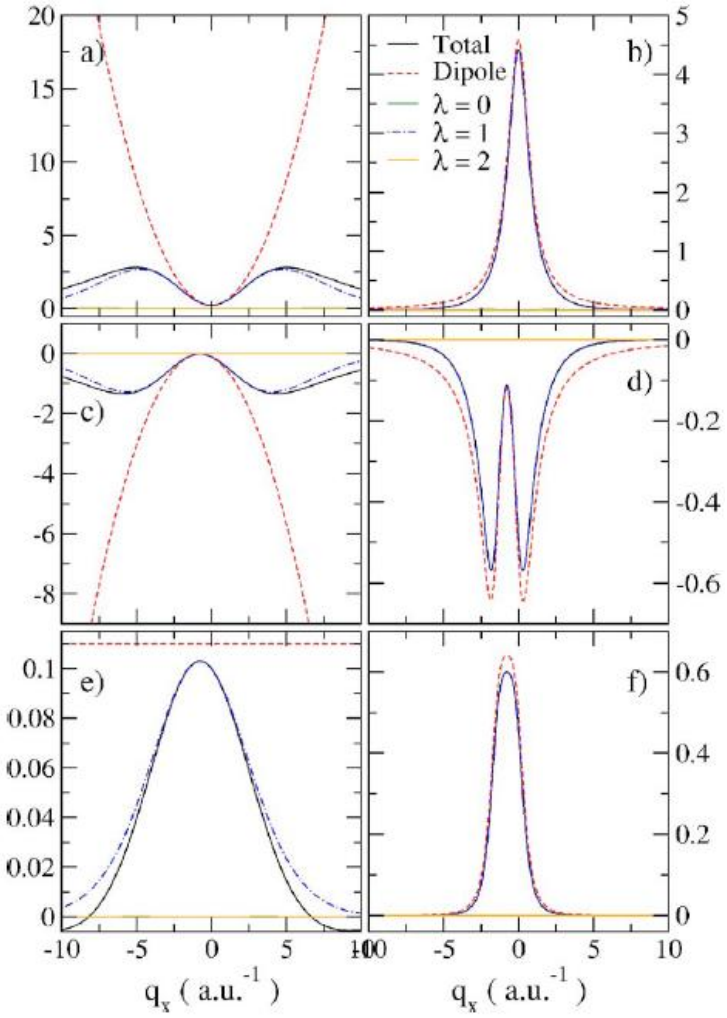

Figure 5.7: Decomposition of MDFF and dipole approximation calculated for hcp-Co with $\vec{q'} - \vec{q} = \vec{G} = (100)$ and $q_y = q'_y = |G|/2$ as a function of q_x (in reciprocal atomic units a.u.$^-1$) at the L_3 edge. Left column - graphs a), c) and e), show $S(\vec{q}, \vec{q'}, E)$ and right column, graphs b), d) and f), show $S(\vec{q}, \vec{q'}, E)/q^2 q'^2$. Top row - a) and b) - is the DFF, middle row - c) and d) - is the real part of the MDFF and bottom row - e) and f) - is the imaginary part of the MDFF. The y axes are in arbitrary units, but consistent within the given column. The values for the L_2 edge differ only by a factor of 2.1 for the real part and -1 for the imaginary part. Note that the contributions of $\lambda = 0, 2$ always coincide with the x axis and can be neglected. See text for more details. Figure from Ref. [4].

It is worth mentioning that thanks to the properties of the Gaunt coefficients the $2p \rightarrow 3d$ transitions are all included in the $\lambda = 1$ and $\lambda = 3$ contributions. Thanks to the negligible value of the radial integrals for $\lambda = 3$ the terms with $\lambda = 1$ account for the large majority of the calculated signal. The contributions from $\lambda = 0, 2$ describe transitions from $2p$ to valence p or f states and are always negligible due to the composition of the density of states beyond the Fermi level. They practically overlap with the zero axis in all the six parts of fig. 5.7.

It was shown in paragraph 5.2 that in the dipole approximation the real part of the MDFF is proportional to $\vec{q} \cdot \vec{q'}$ and the imaginary part is proportional to $\vec{q} \times \vec{q'}$. Neglecting the q_z and q'_z components this means (for the geometry described in fig. 5.7):

$$\Im[MDFF] \propto q_x q'_y - q_y q'_x = \frac{G}{2}(q_x - q'_x) = \frac{G}{2}G \tag{5.62}$$

$$\Re[MDFF] \propto q_x q'_x + q_y q'_y = q_x(q_x - G) + \frac{G^2}{4} = \left(q_x - \frac{G}{2}\right)^2 . \tag{5.63}$$

As expected, the DFF (which is proportional to q^2) has a minimum at $q_x = 0$, where $S(\vec{q}, E)/q^4$ has a maximum. For the MDFF (and corresponding $S(\vec{q}, \vec{q'}, E)/q^2 q'^2$) the maximum is at $q_x = -G/2 = -0.76\ a.u.^{-1}$ where $|q_x| = |q'_x|$), except for the imaginary part which is constant.

5.6 Simulations

Here are summarized the results obtained for body-centered cubic iron (bcc-Fe), hexagonal close-packed cobalt (hcp-Co) and face-centered cubic nickel (fcc-Ni) crystals, which are also the first samples prepared for EMCD measurements. These results are valuable for optimization of the experimental setup.

The geometry setup (see figs. 5.3 and 5.8) for observing the dichroic effect [3] consists in creating a two-beam case by tilting the beam away from a zone axis (here [001]) by a few degrees and then setting the Laue circle center equal to $\vec{G}/2$ for the $\vec{G}$ vector to be excited. In analogy to XMCD, where two measurements are performed for LCP and RCP light, here two measurements are performed by changing the position of the detector, which lies once at the top and once at the bottom of the Thales circle having as

diameter the line connecting the diffraction spots $\vec{0}$ and $\vec{G}$. This geometry setup, together with the crystal structure, is an input for the calculation of the Bloch wave coefficients (within the systematic row approximation) using the dynamical diffraction theory code described in paragraph 5.4.

The electronic structure was calculated using the WIEN2k package [75]. The experimental values of the lattice parameters were used. More than 10,000 $\vec{k}$-points were used to achieve a very good convergence of the Brillouin zone integrations. Atomic sphere sizes were 2.2, 2.3 and 2.2 Bohr radii for bcc-Fe, hcp-Co and fcc-Ni, respectively. The resulting electronic structure was the input for the calculation of the individual MDFFs required for the summation (see paragraph 5.5).

In the three cases here presented the dichroic effect is dominated by the transitions to the unoccupied $3d$ states. The d-resolved spin-up DoS is almost fully occupied, while the spin-down d-DoS is partially unoccupied. In fig. 5.9 the d-DoS is compared with the dichroic signal at the L_3 edge. Due to negligible orbital moments in these compounds the L_2 edge shows a dichroic signal of practically the same magnitude but with opposite sign. The shape of the calculated dichroic peaks corresponds to the difference of spin-up and spin-down d-DoS, similarly to XMCD, as it was shown for the same set of systems [86]. The calculations were performed within systematic row conditions with $\vec{G} = (200)$ for bcc-Fe and fcc-Ni and $\vec{G} = (100)$ for hcp-Co. The sample thickness was set to 20 nm, 10 nm and 8 nm for bcc-Fe, hcp-Co and fcc-Ni, respectively. These values were found to be optimal for these systems in the given experimental geometry.

An interesting point is the comparison of the strength of the dichroic signal. According to the d-DoS projections one would expect comparable strength of signals for the three elements under study. But the dichroic signal of hcp-Co seems to be approximately a factor of two smaller than that of the other two. The reason for that can be explained by simple geometrical considerations starting from eq. 5.50. For simplicity only the main contributions are considered: the DFF $S(\vec{q}, \vec{q}, E)$ and the MDFF $S(\vec{q}, \vec{q'}, E)$ with $\vec{q} \perp \vec{q'}$. For bcc-Fe and fcc-Ni the summation over $\vec{u}$ within the Bravais cell leads always to the structure factor 2 and 4, respectively, because $\vec{q'} - \vec{q} = \vec{G}$ is a kinematically allowed reflection. This factor cancels out after division by the number of atoms in the Bravais cell. Therefore regardless of the value of the $\vec{q}$-vectors, the sum over the atoms is equal to $S(\vec{q}, \vec{q'}, E)/q^2q'^2$ itself. On the other hand, the unit cell of hcp-Co contains two equivalent atoms at

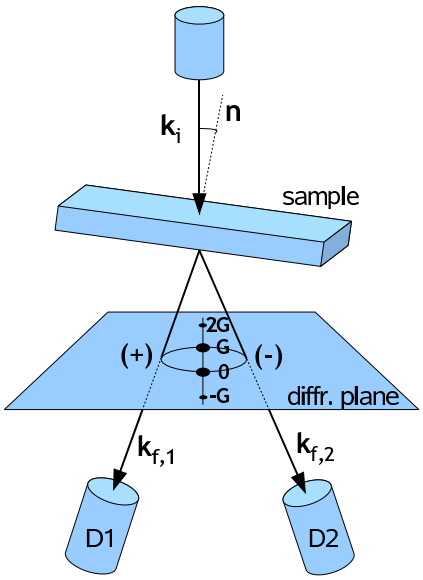

Figure 5.8: Experimental geometry. The bar shaped sample is tilted so that its surface normal $\vec{n}$ forms an angle of approximately 10 degrees with the incoming beam direction $\vec{k}_i$. This excites a systematic row of Bragg reflections $-\vec{G}$, $\vec{0}$, $\vec{G}$, $2\vec{G}$, and so on. Two spectra are measured by detectors D1 and D2 placed in $\vec{k}_{f,1}$ and $\vec{k}_{f,2}$ directions, which correspond to the positions with +1 and -1 helicity on the Thales circle above strongest $\vec{0}$ and $\vec{G}$ reflections in the diffraction plane (see also figs. 5.5 and 6.1). The two-beam case is excited by setting LCC to $\vec{G}/2$. Figure from Ref. [4].

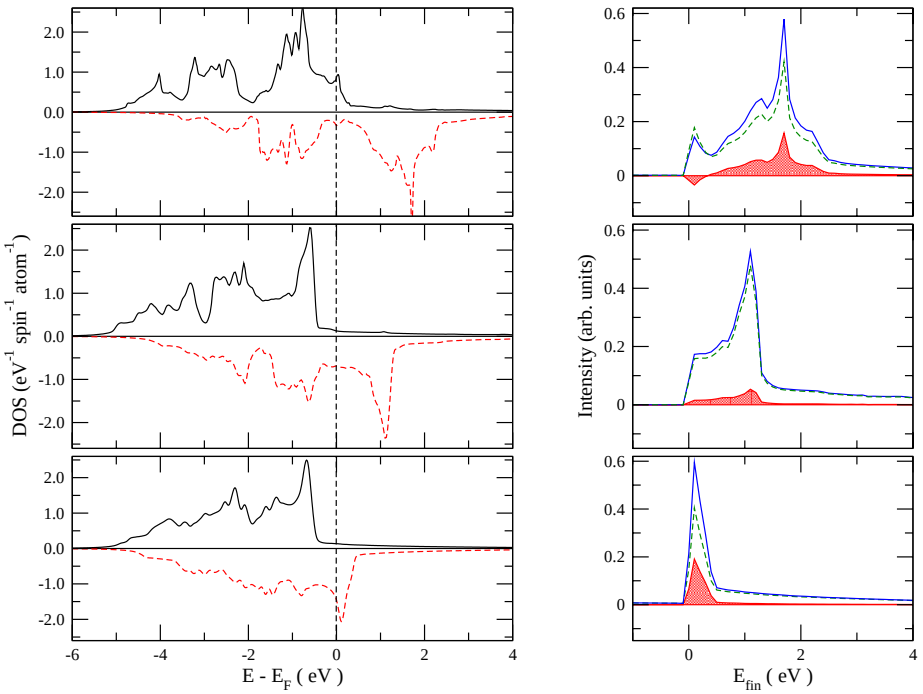

Figure 5.9: Spin-resolved d-densities of states (left) and resulting signal on L_3 edge (right) for bcc-Fe, hcp-Co and fcc-Ni (from top to bottom) at optimal thickness (see text). Spin-up DoS is drawn using a solid black line (positive) and spin-down DoS using a dashed red line (negative). The DDSCS for the positive helicity is drawn using a solid blue line, the DDSCS for the negative helicity is drawn using a dashed green line. The dichroic signal (difference) is the hatched red area. $\vec{G} = (200)$ for bcc-Fe and fcc-Ni and (100) for hcp-Co. Figure from Ref. [4].

positions $\vec{u}_1 = (\frac{1}{3}, \frac{2}{3}, \frac{1}{4})$ and $\vec{u}_2 = (\frac{2}{3}, \frac{1}{3}, \frac{3}{4})$. For the two DFFs, $\vec{q} = \vec{q'}$ and the exponential reduces to 1; since there are two such terms, after division by $N_{\mathbf{u}}$ the sum equals again the DFF itself. But for the main MDFF $\vec{q}$ is perpendicular to $\vec{q'}$ and the exponential factor will in general weight the terms. One can easily see that $\vec{q'} - \vec{q} = \vec{G}$. For the $\vec{G} = (100)$ systematic row case, which was used for calculation of hcp-Co in fig. 5.9, the exponentials evaluate to the complex numbers $-\frac{1}{2} \pm i\frac{\sqrt{3}}{2}$ and $-\frac{1}{2} \mp i\frac{\sqrt{3}}{2}$ for $\vec{u}_1$ and $\vec{u}_2$, respectively. Because of symmetry, the MDFFs for both atoms are equal and then the sum $N_{\mathbf{u}}^{-1} \sum_{\mathbf{u}}$ leads to a factor $-\frac{1}{2}$ for the MDFF contribution, *i.e.* the influence of its imaginary part, responsible for the dichroism, on the DDSCS is reduced by a factor of two. This would not be the case in an XMCD experiment, since the phase of the excitation (and therefore its chirality) does not depend on the sample.

To optimize the dichroic signal strength of hcp-Co, one can impose the condition $\vec{G} \cdot \vec{u}_1 = \vec{G} \cdot \vec{u}_2 = 2\pi n$, which gives in principle an infinite set of possible $\vec{G}$ vectors. The one with lowest hkl indices is $\vec{G} = (110)$. A calculation for this geometry setup leads to approximately twice the dichroic signal, see fig. 5.10 and compare to the corresponding plot in fig. 5.9.

For the optimization of the experimental setup it is important to know how sensitive the results are to variation of the parameters like the thickness of the sample or the accuracy of the detector position. Another question related to this is also the sensitivity to the finite size of the convergence and collection angles α and β. In the following these questions are addressed.

The thickness influences the factor $T_{jlj'l'}$ in the eq. 5.50 only. This factor leads to the so called *pendellösung* oscillations - modulations of the signal strength as a function of thickness. This also influences the strength of the dichroic signal. Results of such calculations are displayed in fig. 5.11 (absorption is not included into these simulations, so that all signal variations are only due to the geometry of the sample). From these simulations it follows that a well defined thickness of the sample is a very important factor. Relatively small variations of the thickness can induce large changes in the dichroic signal, particularly in fcc-Ni for $\vec{G} = (200)$. From the figure one can deduce that the optimal thickness for a bcc-Fe sample should be between 8 nm and 22 nm (of course, due to absorption, thinner samples within this range would have a stronger signal), for hcp-Co between 15 nm and 22 nm and for fcc-Ni it is a relatively narrow interval - between 6 nm and 10 nm. However, it is important to note that these results depend on the choice of the systematic row vector $\vec{G}$. For example hcp-Co with $\vec{G} = (100)$ (shown

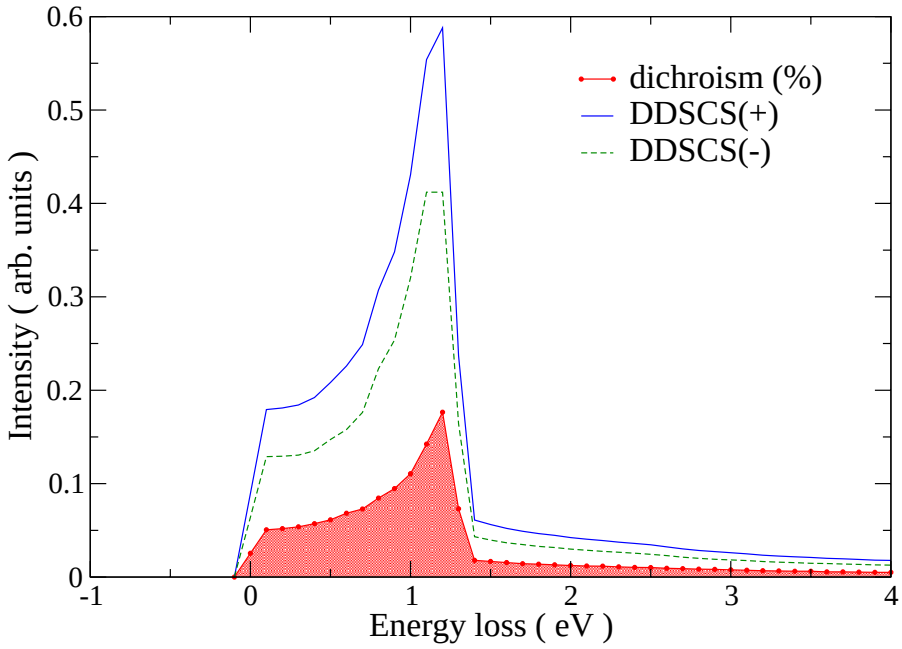

Figure 5.10: L_3 peak of hcp-Co calculated for the $\vec{G} = (110)$ systematic row at 18 nm. Compare with fig. 5.9. The peaks have been renormalized so that their sum is 1, therefore their difference is the dichroic signal ($\approx 17\%$ in this case). Figure from Ref. [4].

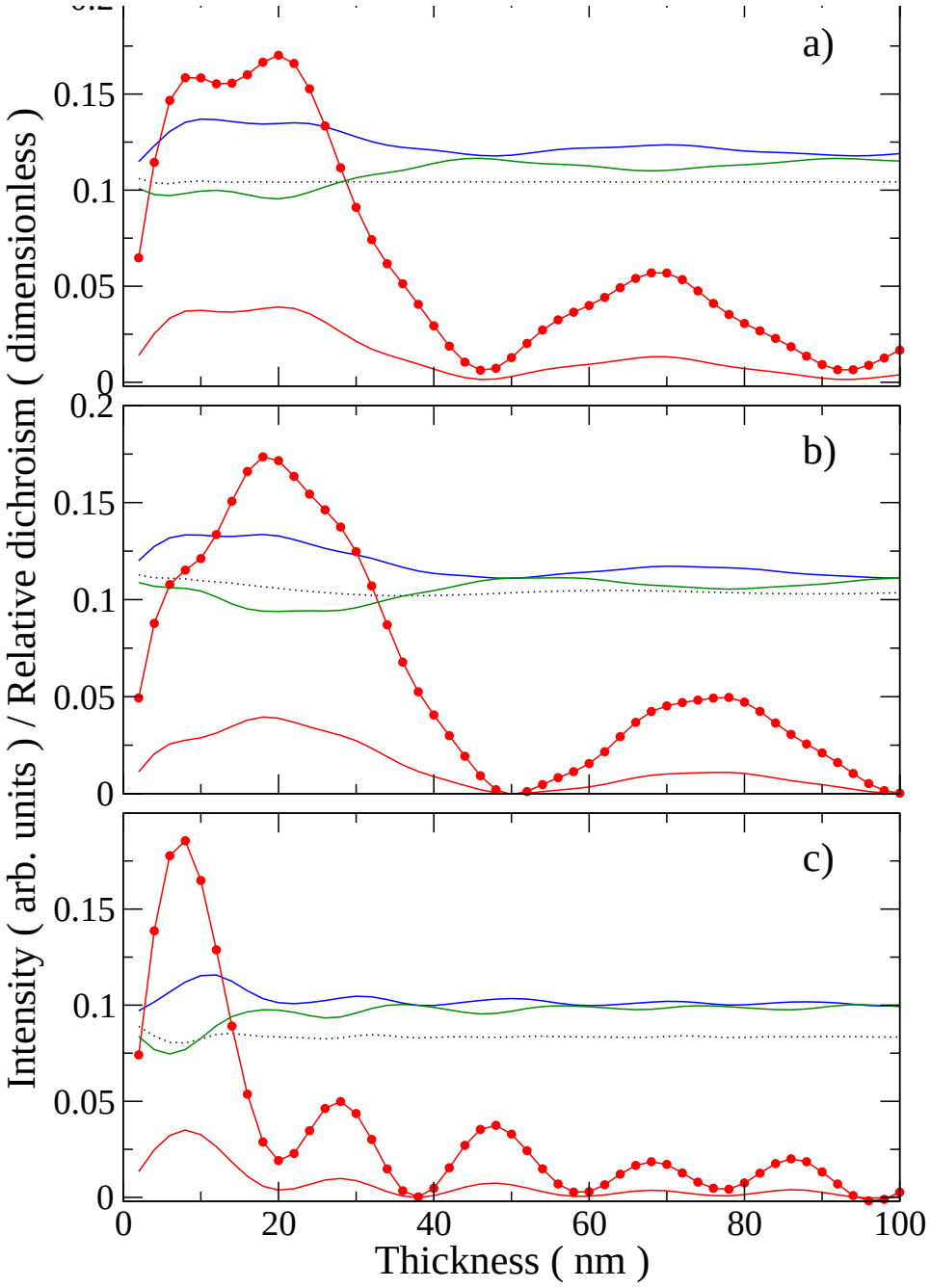

Figure 5.11: Dependence of the DDSCS and of the dichroic signal on the sample thickness for a) bcc-Fe, b) hcp-Co and c) fcc-Ni. The systematic row vector $\vec{G} = (200)$ was used for bcc-Fe and fcc-Ni, while for hcp-Co $\vec{G} = (110)$ was chosen. The blue and green solid curves are the DDSCSs calculated for opposite helicities, the dashed black curve is the DFF part of the DDSCS (which does not depend on the helicity). The red line with circles is the relative dichroism defined as difference of DDSCSs divided by their sum, the red solid curve is the absolute dichroism - difference of DDSCSs. Figure from Ref. [4].

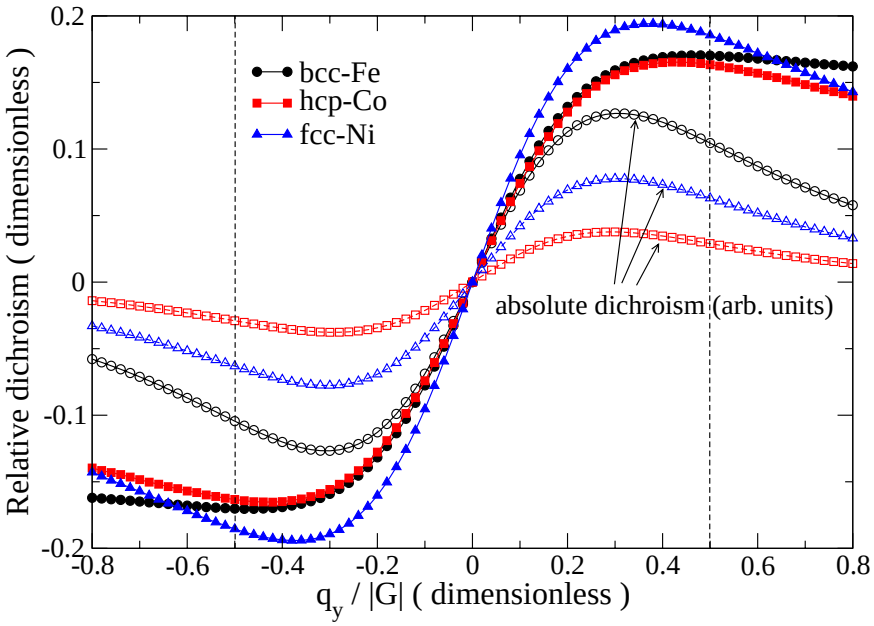

Figure 5.12: Dependence of the dichroic signal on detector displacements along q_y. The absolute dichroism is simply the difference between the L_3 peaks of spectra with opposite helicity. The relative dichroism is the absolute difference divided by the sum of the spectra at the L_3 peak. Vertical lines are showing the *default* detector positions. Figure from Ref. [4].

in fig. 6.7, whereas $\vec{G} = (110)$ is shown in fig. 5.11) has a maximum between 5 nm and 15 nm (although it is much lower, as discussed before).

Taking the optimal thickness, namely 20 nm, 18 nm and 8 nm for bcc-Fe, hcp-Co and fcc-Ni, respectively, the dependence of the dichroic signal on the detector position was calculated. Of particular relevance are changes of the dichroic signal when the detector is moved away from its *default* position in the direction perpendicular to $\vec{G}$, see fig. 5.12. It is interesting to note that the maximum absolute difference occurs for a value of q_y smaller than $|G|/2$. This can be explained by the fact that q_z and q'_z are small but non-zero and this implies that $\vec{q}$ and $\vec{q'}$ are not exactly perpendicular at the default detector

positions. Moreover the MDFF enters the summation always divided by $q^2q'^2$ and the lengths of $\vec{q}$ decrease with decreasing q_y. The important message that can be deduced from this figure is that the dichroic signal is only weakly sensitive to the accuracy of q_y since even displacement by 10-20% from the detector default q_y positions ($q_y = \pm G/2$) do not affect significantly the measured dichroic signal.

Related to this is a study of the dependence of the dichroic signal on the finite size of the convergence and collection angles α and β. A calculation for these three transition metals found that collection and convergence half-angles up to 2 mrad weaken the relative dichroic signal by less than 10%.

To produce the two-beam case, the incoming beam is first tilted away from a Zone Axis (a high-symmetry direction) by an angle θ_{ZA} (usually a few degrees). The direction of this tilt determines which excitations ($\vec{G}$ vectors) will lie close to the Ewald's sphere. Then LCC is set to $\mathbf{G}/2$ by a small (a few mrad) tilt in the direction of $\vec{G}$, so that the direct beam $\vec{k}_i$ and the diffracted beam $\vec{k}_i + \vec{G}$ have the same Bloch wave coefficients. The simulations have shown that the dichroic signal is very sensitive to the selection of a particular systematic row. Fig. 5.13 shows calculations of the thickness profiles (dependence of the signal on the sample thickness) of bcc-Fe and fcc-Ni for two $\vec{G}$ vectors. While $\vec{G} = (200)$ for iron and (220) for nickel display a broad peak around 15-20 nm, when $\vec{G}$ is set to (110) for iron and (200) for nickel more maxima and minima of the signal appear in its thickness profile. This imposes more stringent requirements on specimen drift, uniformity of thickness in the sampled area and precision of the determination of the thickness.

This figure simultaneously shows the dependence of the signal on the acceleration voltage of the fast electron. The general shape of the profiles is preserved, but non-negligible differences can be evidenced, especially with respect to the periodicity. For higher acceleration voltage the frequency of the oscillations in thickness decreases. The overall strength of the dichroic effect is not changed. This behavior can be qualitatively understood by observing that the mean free path of the probe electron increases when the acceleration voltage is increased and so does the extinction distance for each $\vec{G}$-reflection.

The sensitivity of the signal on θ_{ZA} (the beam tilt away from the Zone Axis) was also studied. Fig. 5.14 shows calculations of the thickness profiles of bcc-Fe for $\vec{G} = (110)$ and fcc-Ni for $\mathbf{G} = (220)$, respectively, at 200 keV acceleration voltage as a function of the beam tilt from the [001] Zone Axis.

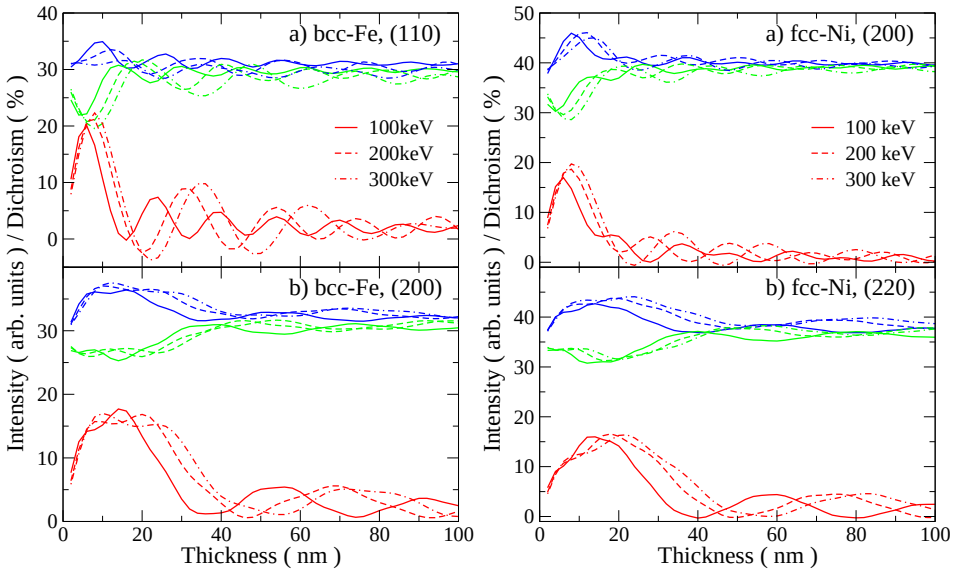

Figure 5.13: Thickness profiles of bcc-Fe (left) and fcc-Ni (right) as a function of the acceleration voltage. Within each panel, the top sets of curves (blue and green) correspond to the EELS signal at the L_2 edge for opposite helicities. These are given in arbitrary units. The bottom curves (red) are the relative dichroic signal (difference normalized to the sum) in percent. Systematic row indices are a) $\vec{G} = (110)$ and b) $\vec{G} = (200)$ for iron and a) $\vec{G} = (200)$ and b) $\vec{G} = (220)$ for nickel, respectively. Figure from Ref. [87].

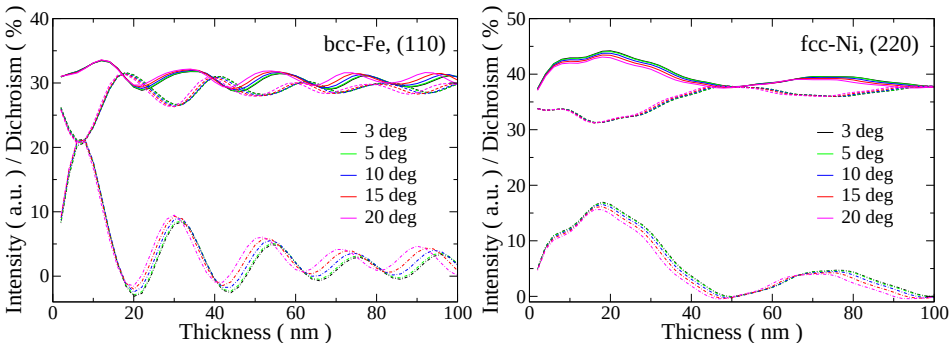

Figure 5.14: Thickness profiles of bcc-Fe [left, $\vec{G} = (110)$] and fcc-Ni [right, $\vec{G} = (220)$] as a function of the incoming beam tilt angle θ_{ZA} at 200 keV acceleration voltage. The full and dashed lines correspond to the EELS signal at the L_2 edge for opposite helicities. The dash-dotted line is the relative dichroic signal in percent. Figure from Ref. [87].

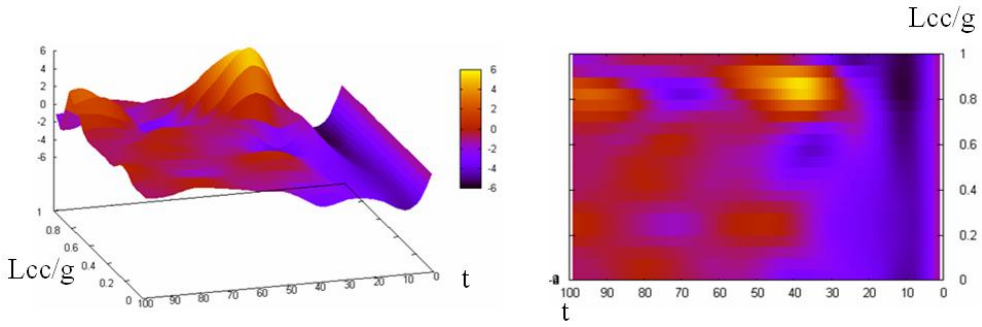

Figure 5.15: Dichroic signal at the Co L_3 edge for the $\vec{G} = (1, 0, 0)$ systematic row as function of thickness and tilt of the incoming beam.

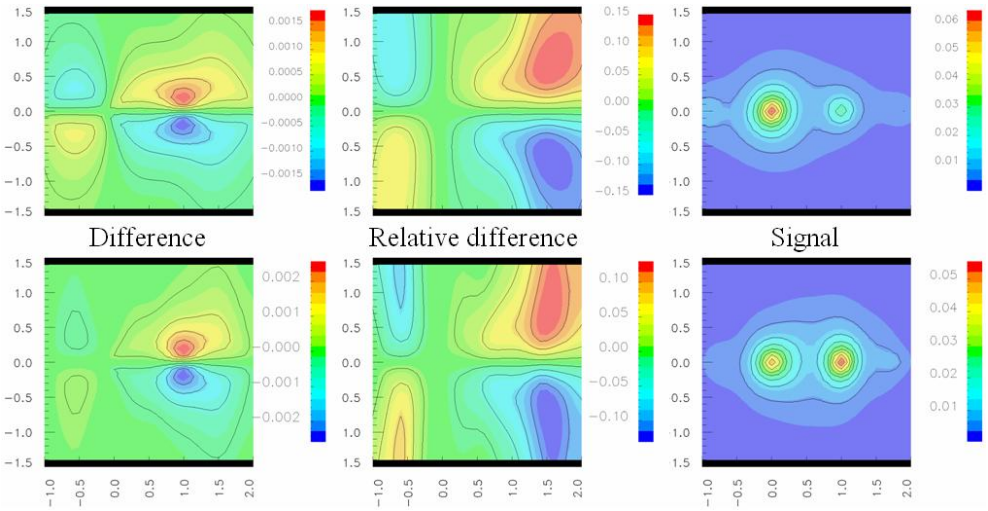

Figure 5.16: Co L_3 edge simulated distribution in the q_xq_y diffraction plane of the total signal (right), absolute difference (left) and relative difference (middle) calculated between a point P(q_x, q_y) and its symmetric P'$(q_x, -q_y)$ with respect to the systematic row line $\vec{G} = (1, 0, 0)$ for a two-beam case. The *pendellösung* effect is particularly visible when comparing the simulations for a thickness of 12 nm (upper row) with the ones for 18 nm (lower row). The shift in the intensity from the (0,0,0) to the (1,0,0) spot when the thickness is increased translates into an important change in both the absolute and relative difference. It should be noted that the maximum of the dichroic signal is not on the two symmetric positions on the Thales circle but closer to the (1,0,0) spot.

The tilt angle in the calculations ranges from 3 to 20 degrees. It should be noted that for very low angles the systematic row approximation becomes questionable, because other reflections from the (001) plane outside the systematic row are also very close to the Ewald's sphere and should no longer be neglected. Whereas it is possible to include them into the calculation (as the code is not restricted to the systematic row case), this increases the calculation time considerably. For higher beam tilts the approximation is very good and the influence of the beam tilt angle on the signal is very weak. Essentially, a larger tilt angle makes the oscillation period slightly smaller (this is connected with a smaller projection of the incoming beam wave vector to

the (001) surface normal).

An example of simulation of the dichroic signal as function of the LCC is illustrated in fig. 5.15. Here the effect of the tilt angle on the thickness dependence is much stronger than in the previous case, especially considering the change of scale: degreees in fig. 5.14, fractions of G ($\approx$ 10mrad) in fig 5.15). This is because in the systematic row approximation it is only the LCC, together with the thickness, that determines the values of the Bloch coefficients obtained as solution of the secular equation (paragraph 5.4).

By simulating EELS spectra for different detector positions it is possible to obtain the distribution of the spectral intensity in the diffraction plane (a so called *dichroic map*, fig. 5.16); by simple subtraction, the distribution of the dichroic signal as function of the scattering angle can be obtained as well. This can prove very useful not only for predicting the result of an ESD experiment, but also in providing indications on the best positioning of the SEA (or OA) in a spectroscopic experiment. The results show that the symmetric positions on the Thales circle are not always the best placement for the $\vec{q}$-selecting aperture.

5.7 Signal-to-noise ratio

Physics is an experimental science. As such, measured data are the basis of any serious investigation, supporting or disproving a theory or a model created to explain a phenomenon. However the result of any experiment cannot be considered valid if an estimate of their precision and accuracy is not given, that is, if the error in the measurements is not analyzed and specified. In the case of EELS, the major source of error is the Poissonian noise associated with the detection (counting) of the electrons which have lost a certain amount of energy. In this paragraph a general discussion on the SNR will be presented, together with some general consideration on how to improve it by choosing appropriate conditions for the detector (namely the shape and size of the SEA). To facilitate the exposition the spectral intensity (strictly related to the DDSCS, eqs. 5.13 and 5.30) is simplified to

$$I^{\pm} = I^0 \frac{\partial^2 \sigma}{\partial E \partial \Omega} = I^0 \frac{4\gamma^2}{a_0^2} \Big(\frac{M_1}{q^4} + \frac{M_2}{q'^4} + 2M' \cos\phi \frac{\vec{q} \cdot \vec{q'}}{q^2 q'^2} \pm 2M'' \sin\phi \frac{\vec{q} \times \vec{q'} \cdot \vec{e_z}}{q^2 q'^2} \Big) \tag{5.64}$$

where ϕ is the phase difference between the two interfering electron waves (eq. 5.32) and M_1, M_2, M', M'' are parameters which are a real function of the material, the thickness, the incidence angle of plane waves, the excitation energy and elastic scattering. In the most general case, the parameters depend on the wave vector transfer $\vec{q}$ and numerical simulations are needed.

The absolute dichroic signal is defined as the difference between the intensity of spectra taken for two different helicities (such as the ones occurring at the symmetrical positions on the Thales circle described in figs. 5.5 and 5.8):

$$I_D = I^+ - I^- = \Delta I. \tag{5.65}$$

As explained at the end of paragraph 5.2 (in particular eq. 5.30) these two positions are expected to provide an optimal dichroic signal since the vector product $q \times q'$ has a maximum. To obtain the SNR for the dichroic signal it is assumed that the noise in the detector is Poisson counting noise and the noise is independent for the two different detector positions. For Poisson noise one has:

$$V_A = var(A) = \overline{A} \tag{5.66}$$

Which gives for the variance on the dichroic signal:

$$var(I_D) = var(I^+) + var(I^-) \tag{5.67}$$

The signal to noise ratio is then defined as:

$$SNR_D = \frac{I^+ - I^-}{\sqrt{I^+ + I^-}} \tag{5.68}$$

Note that this formula is generally applicable also in the more complicated case of dynamic diffraction and even for experimental data. It is based purely on the method of treating the data and assuming Poisson noise and it is independent on the cross section formula. For a non-point-like detector the signal has to be integrated over the detector aperture. The intensities are integrated assuming that a real detector will actually detect the arrival position of electrons effectively measuring the probability and not the wave function. This is for instance the case if a scintillator is used in combination with a photon detector. The SNR then becomes:

$$SNR_{D,S} = \frac{\int_S I^+ ds - \int_S I^- ds}{\sqrt{\int_S I^+ ds + \int_S I^- ds}} \tag{5.69}$$

With S the area of the detector aperture.

Note that the SNR for a fixed aperture S scales as expected as:

$$SNR \propto \sqrt{N} \tag{5.70}$$

With N the number of detected electrons in the aperture. This shows how important it is to optimize the SNR by choosing the right detector S since it is very hard to improve the SNR significantly by *e.g.* increasing exposure time or beam current.

Although the relative strength of the chiral signal in the simple analytic model is strongest on the Thales circle, one could argue that in terms of SNR in the final chiral signal it would be advantageous to integrate over a larger detector. It will now be calculated, for the idealized two-beam case, what the effect of non-point-like detectors is on the SNR in the chiral signal, starting with a simple round detector since that is readily available in the microscope as the SEA. In a second step it will be shown that the SNR is improved by optimizing the shape of the detector to the signal. For a round detector with radius r_D and position q_D one can determine the SNR of the chiral signal by numerically integrating the signal over the detector area and then applying the formula for the SNR on this signal. One can check the effect of the different positions of the detector by convolving the detector shape with the signal and then applying eq. 5.69 on it. This will give a SNR map for a given detector size for all possible positions. The maximum in this map will point to the ideal detector position for the given size. One could imagine that other shapes of apertures might give rise to a higher SNR. This can be tested by a numerical simulation that adds different discrete points (pixels) of the signal together as long as the SNR keeps increasing. A smarter algorithm for finding this optimal shape S can be found when looking at the SNR for an integrated area and requiring that the change in SNR for going from S to $S + dS$ is zero:

$$\frac{\partial SNR_{D,S}}{\partial S} = 0 \Rightarrow \frac{2(I^+ - I^-)}{I^+ + I^-} = \frac{\int_S I^+ - I^- ds}{\int_S I^+ + I^- ds}. \tag{5.71}$$

Unfortunately this still depends on the optimal shape S but one can at least say that the optimal shape must be a contour line of the function:

$$f = \frac{2(I^+ - I^-)}{I^+ + I^-}, \tag{5.72}$$

since the last term of eq. 5.71 is a constant for a given aperture shape S. An optimized algorithm is to define an aperture A so that

$$A = \begin{cases} 1 & \text{if } f \geq \alpha \\ 0 & \text{if } f < \alpha \end{cases} \tag{5.73}$$

and then step through different threshold values α and stop when the total SNR does not improve anymore. This is a much more efficient algorithm compared to adding pixel by pixel to the aperture.

Different setups were chosen to test the prediction of the ideal aperture size, shape and position. A simple analytical two beams simulation can be then expanded with a dynamical equation simulating a three beam case.

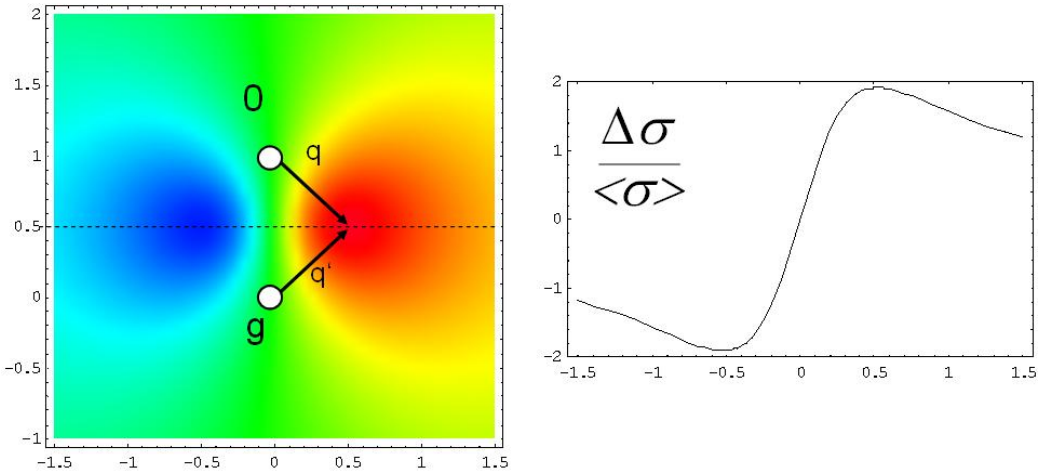

Figure 5.17: **Left**: dichroic signal as function of $q_\perp$ calculated in dipole approximation and neglecting q_z. **Right**: line trace along the horizontal dotted line of the left panel, passing through the symmetric + and - positions on the Thales circle.

First of all one can assume in eq. 5.64 $M_1 = M_2 = 1$ and $M' = M'' = 0.1$ as the most simple numerical example for dichroism. In dipole approximation (and neglecting any momentum transfer in the z direction) the expected distribution of the dichroic signal in the diffraction plane is plotted in fig. 5.17.

The results for the optimal position for the simple analytical case are shown in fig 5.18 and they demonstrate that the larger the aperture, the more one has to shift it up to avoid intersecting the axis connecting the two diffraction spots. The SNR in the final dichroic signal increases significantly for larger apertures and it seems that the upper limit is not yet reached although the increase in SNR levels off. Simulations according to eq. 5.73 show that the ideal aperture shape is circular with a radius of approximately 2.5 G with a position as is shown on fig 5.18 by the dotted line.

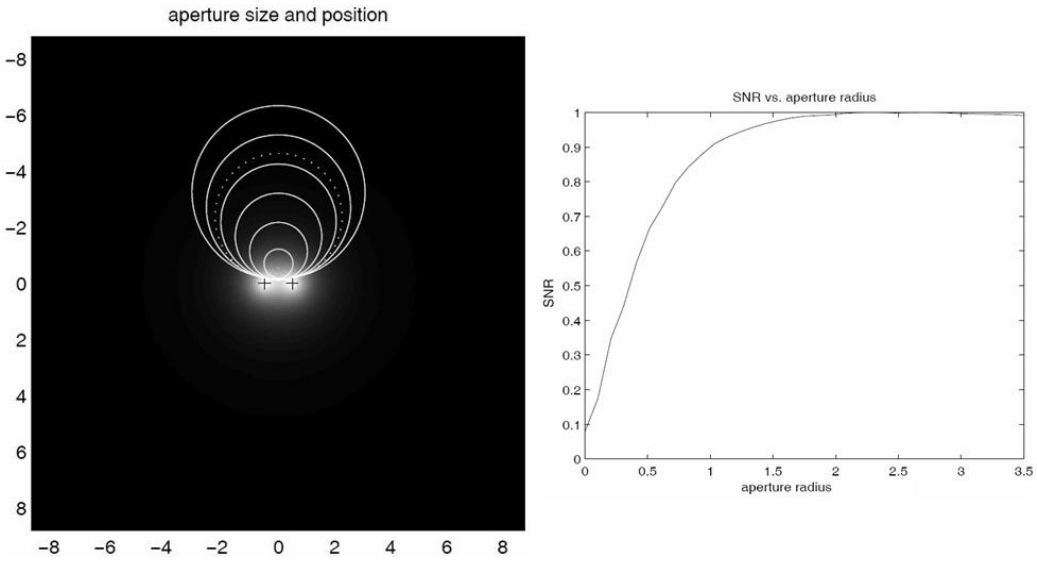

Figure 5.18: **Left**: optimal position for different round apertures in the diffraction plane. For small apertures the optimal position is on the Thales circle as expected but the optimum shifts up for larger detector sizes. The dotted line is the optimal aperture radius. The x and y axis are in unit of G = (1,1,0) for bcc-Fe. **Right**: SNR for different round aperture radii placed at their optimal position for the simple analytic case. A dramatic increase in SNR is obtainable when choosing larger apertures up to $r_D \approx 2.5G$. Figure from Ref. [88].

As a second step first principles simulations are used. These include elastic scattering events before and after the inelastic collision applying dynamical diffraction theory within the Bloch waves formalism, using the WIEN2k extension previously described. MDFFs are calculated using the full Coulomb

operator without assuming dipole approximation. As test case bcc Iron (alpha Ferrite) is chosen. Simulations are performed within the systematic row approximation as a function of energy and thickness on a grid of 51x51 pixels in a square area of the diffraction plane spanning from -2.5 G to 2.5 G in both dimensions, with $\vec{G} = (1, 1, 0)$ and LCC $= (0, 0, 0)$, *i.e.* in the three-beam case.

Applying the same detector integration techniques as before one realizes that the result depends sensitively on the thickness t of the sample. The ideal position for different round apertures is shown in fig 5.19 for $t = 8$ nm and $t = 16$ nm. As opposed to the analytical example, the optimal positions are shifted more towards the (-1,1,0)-beam. The SNR increases also considerably with radius much as for the analytical case. Note that no maximum in the SNR is reached up to aperture radii of 1 G. Most likely, larger apertures would not be practical, because weakly excited beams which are not included in systematic row simulations like, for example, (1,-1,0), will influence the signal in a non-trivial way.

The ideal shape of the aperture greatly depends on thickness and has quite a complicated contour as shown in fig. 5.20. It is clear that the ideal shape is unpractical to use but fortunately fig. 5.21 shows that the difference between the SNR obtained with an ideal aperture and the SNR obtained with a circular aperture is not more than 50% for any thickness. The fact that around 50% increase in SNR is possible for the ideal aperture is mainly due to the fact that two quadrants of the diffraction plane can be used simultaneously as opposed to a single circular aperture.

A surface plot of the SNR with respect to thickness (fig. 5.22) shows that for every value of the sample thickness the SNR goes up considerably with circular aperture radius, and it also shows that there are optimum thickness values around 10 nm and 30 nm which give the best SNR for this setup.

The dependence of the ideal aperture position on the thickness is also shown in fig. 5.22. For every thickness it is advantageous to select the biggest possible aperture radius which was limited in this simulation to 1 G. The optimal position is plotted for thicknesses between 2 and 40 nm and all positions are in the lower left quadrant, closer to the (-1,1,0)-spot. The sensitivity of the SNR on the exact position is shown in fig. 5.23 for a thickness of $t = 16$ nm. It is shown that the SNR has a plateau around which one can shift the position without affecting the SNR too much. One should however avoid that the aperture crosses the line connecting (-1,1,0) with (1,1,0). Therefore a reasonable rule of thumb could be to put a large aperture

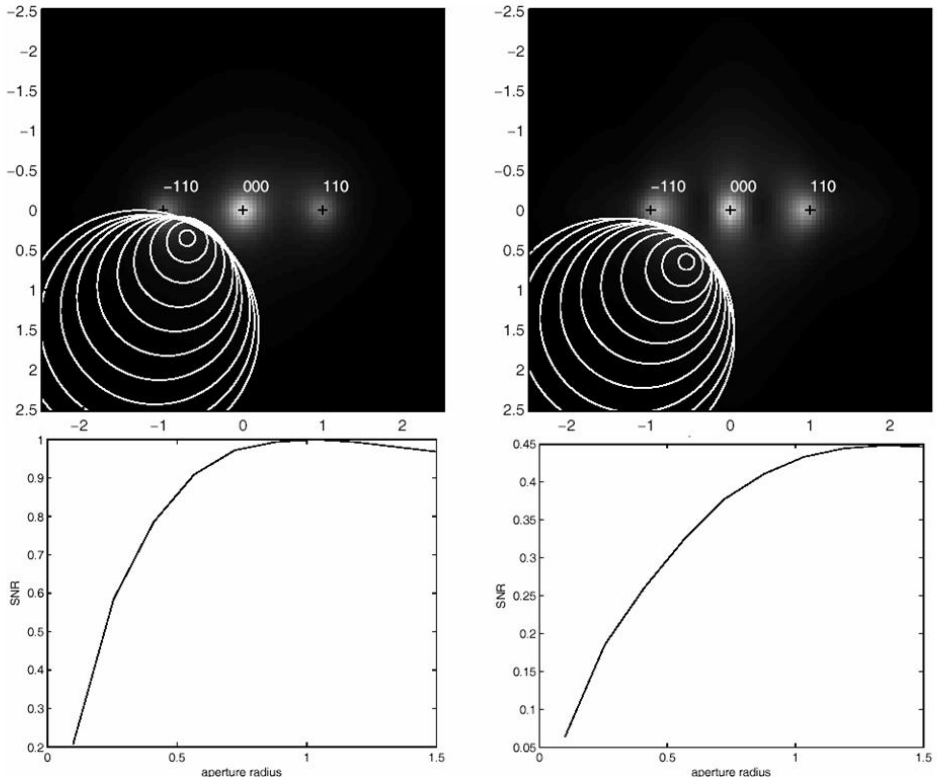

Figure 5.19: **Upper row**: optimal position for different (round) aperture sizes for a 3 beam Bloch wave calculation with (left) $t = 8$ nm and (right) $t = 16$ nm displayed on top of the integrated L_3 signal. **Lower row**: corresponding SNR as function of the size of the aperture radius. Figure from Ref. [88].

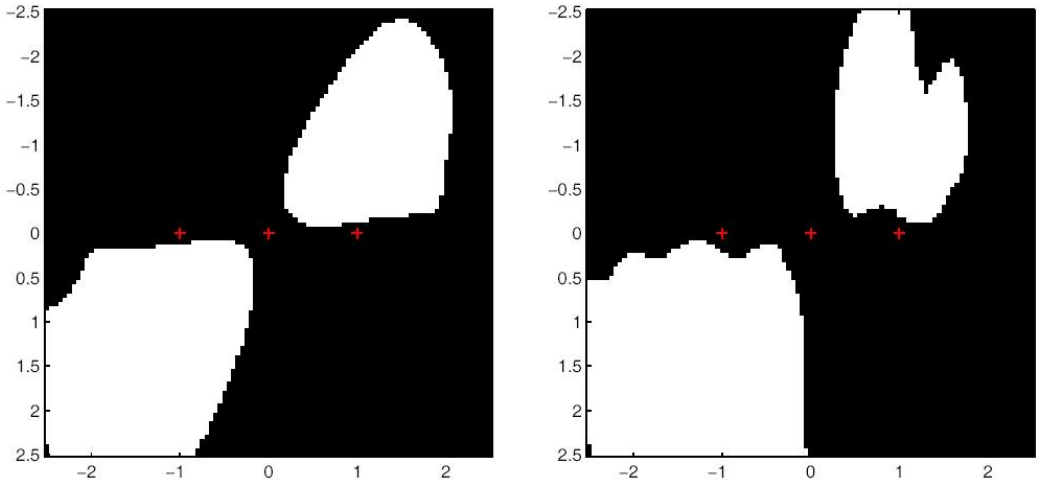

Figure 5.20: Numerically determined ideal shape and position of detector for a 3 beam Bloch wave with (left) $t = 8$ nm and (right) $t = 16$ nm. Figure from Ref. [88].

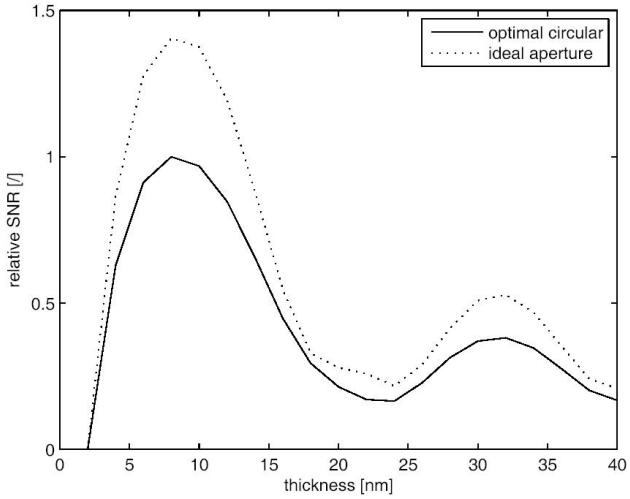

Figure 5.21: Relative SNR for an optimal round aperture at optimal position compared to an ideal aperture as a function of thickness. Figure from Ref. [88].

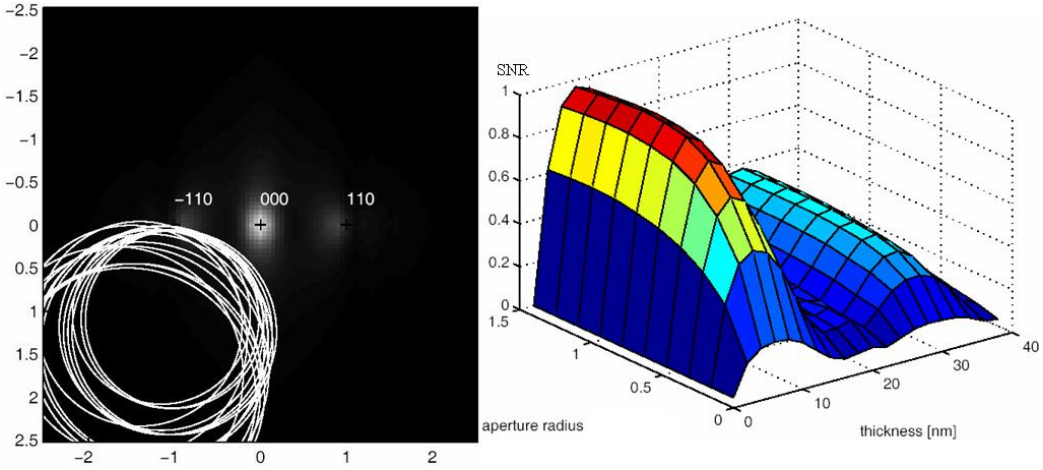

Figure 5.22: **Left**: ideal position and size for a circular aperture for different values of t in the range $2 < t < 40$ (in nm). For each thickness the SNR increases when the aperture radius is increased, thus only the position is given here. The optimal positions are all in the lower left quadrant and closer to the (-1,1,0)-beam. **Right**: relative SNR for a circular aperture at optimal position vs. radius and vs. sample thickness. Note the strong increase of SNR with increasing aperture radius and the dependence on the thickness due to *pendellösung* effect. Figure from Ref. [88].

with radius r_D in a position (-1,-r_D) expressed in terms of the reciprocal vector G, since in experiments one rarely knows the thickness and specimen tilt with the required precision. The position of this aperture can in principle be found from analytical simulations, but fig. 5.23 shows that the position sensitivity of the SNR is not so critical for large apertures, whereas it becomes more critical for small apertures.

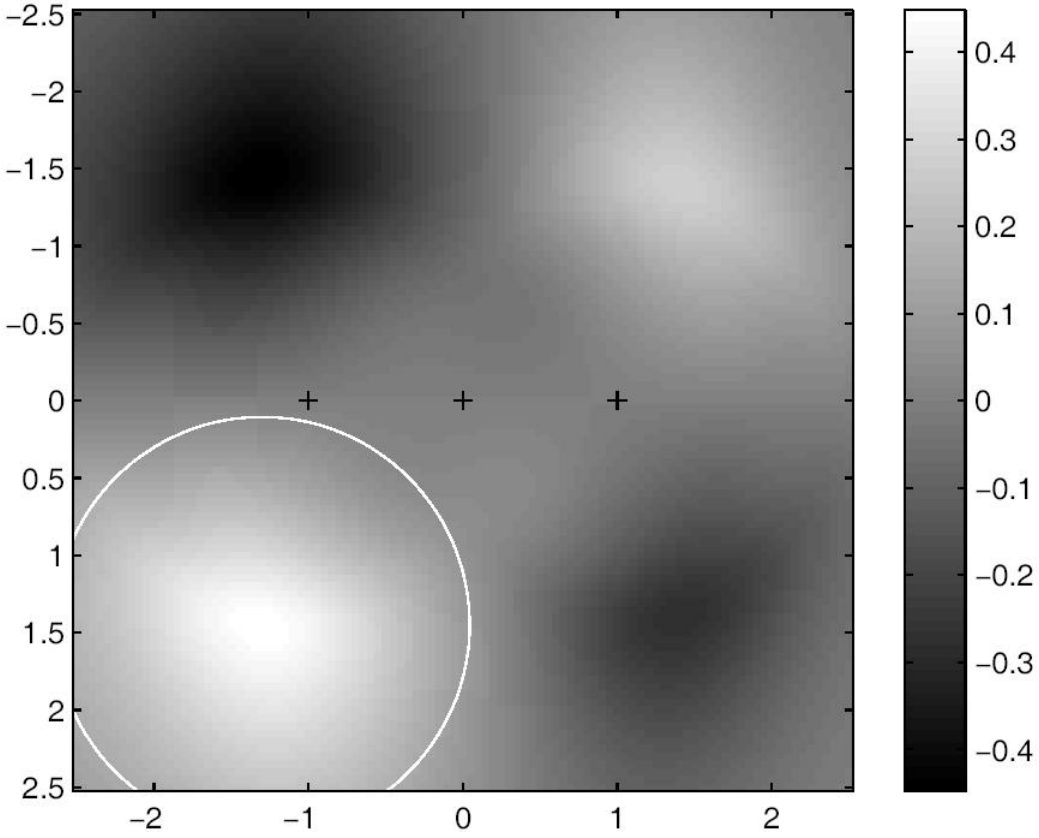

Figure 5.23: Position sensitivity of a circular aperture with $r_D = 1$ G for a thickness of t = 16 nm. Note that SNR is rather insensitive to a movement of the aperture. This could help to define a standard position which gives a reasonable SNR for all thicknesses and all orientations. Figure from Ref. [88].

It should be noted that the present discussion does not take into account noise arising from the variations of the dark count of the detector, which can be neglected only as long as it is much smaller than the Poissonian

noise assumed here. The dark count itself is usually corrected by taking a spectrum without any signal hitting the CCD camera and subtracting it from all subsequent measurements taken with the same acquisition time. When recording the signal with an EELS detector using two aperture positions, this is a good approximation since the signal should be considerably larger than the dark count noise.

Chapter 6

Experiments

The absolute dichroic signal $\Delta\sigma$ is a difference of two measured spectra(σ^+ and σ^-), be it in XAS or EELS. In practice it is often more convenient to refer to the relative dichroic signal σ_{dich} as the absolute difference normalized to the sum of the spectra (or alternatively to their average $\langle\sigma\rangle$):

$$\sigma_{\text{dich}} := \frac{\sigma^+ - \sigma^-}{\sigma^+ + \sigma^-} := \frac{\Delta\sigma}{2\langle\sigma\rangle} \tag{6.1}$$

It follows that, in order to perform a measurement of circular dichroism, one needs a mean to change the chirality of the excitation relative to the magnetic moments, as mentioned in paragraph 5.3. For XMCD experiment this can be easily accomplished by reversing either the polarization of the incident radiation or the magnetization of the sample (for example by physically flipping a ferromagnetic specimen so that its residual magnetization points in the opposite direction).

The matter is more complicated in the case of EMCD. The magnetization of the sample is, for most materials, forced in a particular direction (the TEM optical axis) by the strong magnetic field of the objective lens (≈ 2 Tesla). To reverse the magnetization it would be necessary to reverse the magnetic field of the lens itself (see paragraph 7.4). On the other hand, the chirality of the excitation could be reversed by changing the phase shift from $\pi/2$ to $-\pi/2$; this would reverse the helicity of the perturbing electric field.

However, as demonstrated in the previous chapter, the definition of the polarization of the excitation is not straightforward, as the picture presented in fig. 5.4 is an oversimplification and the phase shift between the two incident waves is not well defined. Moreover, according to the Bloch theory

the electron beam in the crystal is described by a superposition of several Bloch waves, not just two. Their amplitudes and phases are determined by the boundary conditions, namely the beam tilt and the specimen thickness. When more than two of those waves have a non negligible intensity, the resulting excitation would be the analogue of a superposition of several elliptically polarized photons. Another aspect to consider is that contributions to the MDFF (and therefore ultimately to the dichroic signal) can come from the waves after the ionization process. The process itself can occur randomly at any depth z inside the specimen. In this case, the only reliable method to predict the expected dichroic effect is to perform *ab initio* calculations [4]. Additionally, in the theoretical derivation (and in the simulations presented in paragraph 5.6) a parallel illumination and point-like k_f-selecting aperture are assumed. A non-parallel illumination would introduce an integration over $\vec{k_i}$, whereas an aperture with a certain angular size would correspond to an integration over $\vec{k_f}$. In both cases $\vec{q}$ and $\vec{q'}$ can assume a range of values and the resulting signal would be a combination of different chiral excitations. For example in fig. 5.5 the collection angle is clearly not zero and the range of possible values for k_f (and therefore for q_1 and q_2) is indicated by the yellow area. Only the point at the center of the yellow area is on the Thales circle; for all other points q_1 and q_2 are not perpendicular and the excitation acquires a linearly polarized component reducing the (relative) dichroic content of the signal. In practice one has always a finite convergence and collection angle. The more the beam is converged, the more intensity is collected; on the other hand, this will cause a blurring of the dichroic signal in the diffraction plane, possibly reducing the desired effect. Therefore one must always go for a compromise between parallelity and intensity. The implications of this will be explored more in details in paragraph 6.4.

In the following paragraphs, several different EMCD techniques will be described, with some applications on particular samples of interest. Unless otherwise indicated, all EELS spectra were taken on a FEI Tecnai F20-FEGTEM S-Twin equipped with a Gatan Imaging Filter and using the intrinsic way.

In order to be able to compare results obtained in different sessions, it is necessary to give an unambiguous label to two particular scattering directions often used in EMCD experiments. One can define a right-handed reference system in the diffraction plane having the direct beam (000) as origin, the line connecting 000 to the G-reflection as x axis, with the 000 to G direction as the positive one and an y axis perpendicular to the x one. The Thales circle (see also fig 5.5) is drawn by taking the segment 000-G as diameter. In

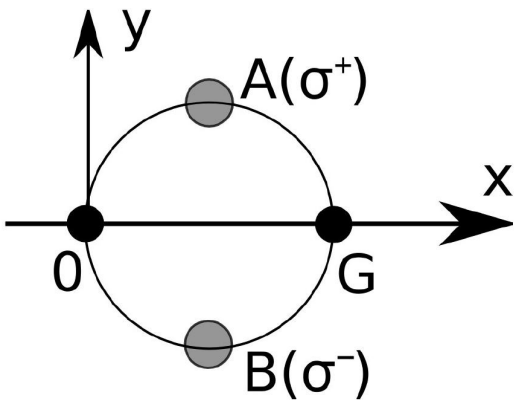

Figure 6.1: Definition of the positions A and B as used in this paper. The axis (000)-G is oriented positively; the position A is the in the upper half-plane and the position B in the lower half-plane. Figure from Ref. [55].

this work it was decided to indicate with *A* (above) or *1* or *+* the position on the Thales circle with the largest value of y and *B* (below) or *2* or - the position in the $y < 0$ half-plane, on the opposite side of the Thales circle (fig. 6.1). Of course results are comparable between different microscopes only if the magnetic field in the objective lens is in the same direction.

6.1 Tilt series

As mentioned in paragraph 5.3, the equivalent polarization of the electron beam in the intrinsic method is affected by the beam tilt and the specimen thickness. It follows that a way to switch from one helicity of the excitation to the other would be to modify the boundary conditions in order to change the phase shift. Fig. 5.4 shows for instance that the phase shift for a 15 nm thick sample changes from $\pi/2$ for LCC (1,0,0) to $-\pi/2$ (which corresponds to the opposite helicity) for LCC (0,0,0). But, as already mentioned, the model presented in fig. 5.4 is an oversimplification of the reality. A better description of the EMCD experiment must take into account the fact that the ionization process can occur at any depth inside the crystals. It must also consider the fact that the incoming and outgoing beams are diffracted as Bloch waves inside the crystal [18]. All these improvements can be included using the dynamical diffraction theory framework.

As demonstrated in chapter 5, the equivalent polarization of the electron beam in an EMCD experiment is a complicated function of the specimen thickness t and tilt with respect to the incoming beam (LCC). Diffraction on the crystal lattice, at first view detrimental to the dichroic signal, can be turned to advantage when one realizes that the phase shift between the 000 and the $\vec{G}$ wave can be tuned by varying the boundary conditions. Moreover, the lattice periodicity automatically serves as a phase-lock amplifier, creating equal phase shifts in each elementary cell. A consequence of this is that the helicity of the excitation can be changed by modifying the boundary conditions in a controlled way. For specimens of non-uniform thickness it would be possible to obtain and compare spectra from regions with different thicknesses. This however would raise questions to the legitimacy of the procedure as one could argue that spectral differences might be attributed to differences in the investigated regions instead than to the different chirality of the two measurements. A safer approach is then to compare spectra taken with different LCCs. In fig. 6.2 the simulated dependence of the L_2 peak value of EELS spectra is shown as function of thickness and LCC (in systematic row approximation).

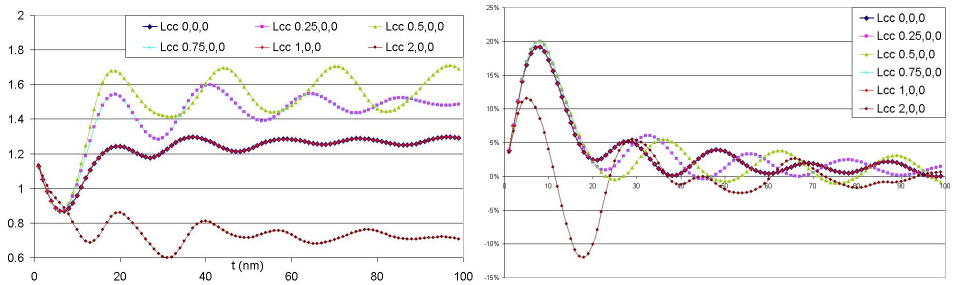

Figure 6.2: **Left**: Simulation of the Ni L_2 peak value of EELS spectra (in arbitrary units) as function of the thickness t (in nm) for $\vec{G} = (2, 0, 0)$ and for different values of the LCC. The detector is placed in the $+$ position of the Thales circle. **Right**: the corresponding dichroic signal for the L_3 edge between positions $+$ and - (as measured in paragraph 6.2).

A remarkable feature is that few plots overlap completely (LCC = (1,0,0) with LCC = (0,0,0) and LCC = $\left(\frac{1}{4}, 0, 0\right)$ with LCC = $\left(\frac{3}{4}, 0, 0\right)$). This is because the relation between the tilt of the incoming wave and the tilt of the outgoing wave [77] is determined by the detector position D:

$$LCC_{out} = D - LCC_{in}. \tag{6.2}$$

The simulations have been calculated for $D = (1, 1, 0)$; this means that when LCC for the incoming wave is set to (1,0,0), which corresponds to a two-beam case for $\vec{G} = (2, 0, 0)$, LCC for the outgoing wave is (0,1,0), which, in systematic row approximation, is equivalent to (0,0,0), a three-beam case. Conversely, for $\mathrm{LCC}_{in} = (0, 0, 0)$ (a three-beam case) $\mathrm{LCC}_{out} = (1, 1, 0) \equiv (1, 0, 0)$ (a two-beam case). More precisely, the two thickness profiles overlap because in eq. 5.50 every $C_{\mathbf{g}}^{(j)}$ obtained for a certain LCC'_{in} becomes the $D_{\mathbf{h}}^{(l)}$ for the tilt which has $\mathrm{LCC}_{out} = \mathrm{LCC}'_{in}$. The symmetry becomes evident in a 3D plot of the dichroic signal as function of both thickness and LCC (fig. 6.3), where the axis of symmetry is passing through the LCC = G/4 = (0.5,0,0), for which $LCC_{out} = LCC_{in} = (0.5, 0, 0)$. The symmetry does not extend to the range $LCC_{in} > G/2$ as it can be seen in fig. 5.15.

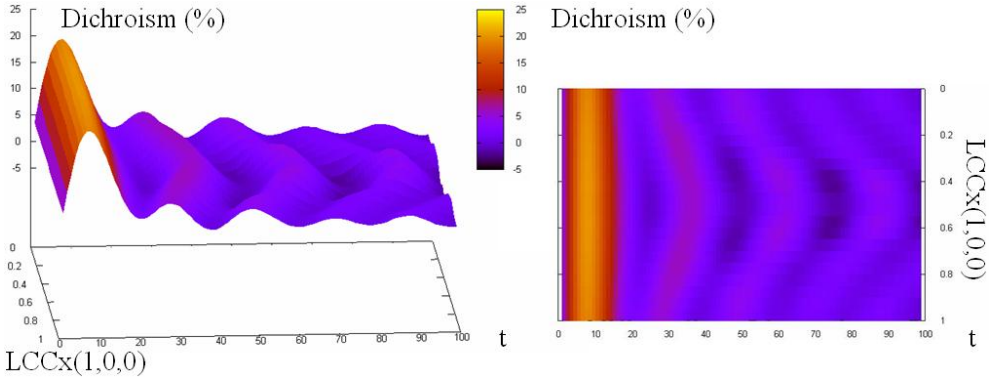

Figure 6.3: Dichroic signal at the Ni L_3 edge for the $\vec{G} = (2, 0, 0)$ systematic row as function of thickness and tilt of the incoming beam. The plot has an horizontal axis of symmetry at LCC=(0.5,0,0).

Experimentally, a tilt series can be performed in three ways: 1) by tilting the goniometer holding the specimen; 2) by deflecting the electron beam so as to change the direction of incidence; 3) if the specimen is slightly bent, by moving into different *bend contours* [15].

All three methods are viable and can be used indifferently, having very limited advantages or disadvantages with respect to each other: in the first case, the precision in the setting of LCC is limited by the accuracy of the

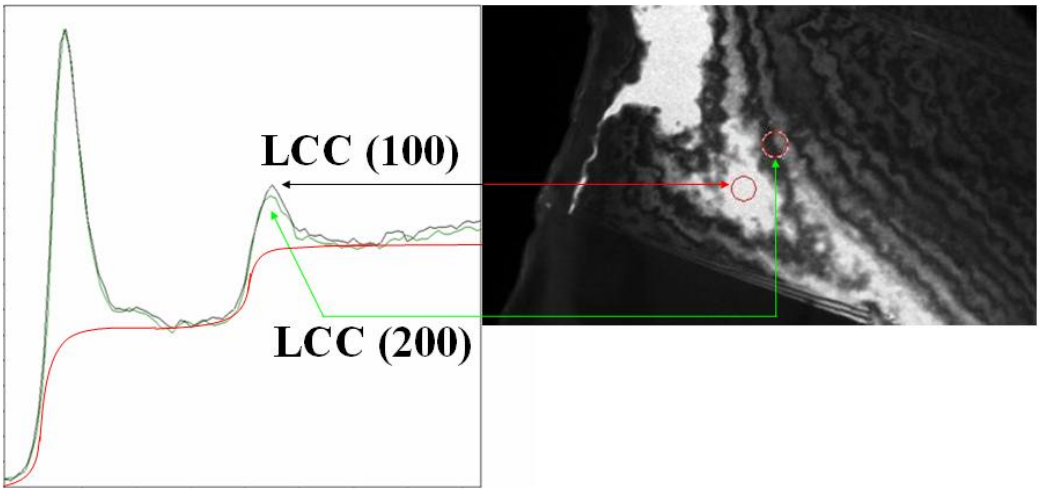

Figure 6.4: First detection of EMCD. **Left**: EELS spectra of the $L_{2,3}$ edge of Nickel, taken for two different values of LCC, with a thickness of 70 nm. The difference in the intensity of the two L_2 peaks is 10% after subtraction of the background approximated by a double step arc tangent function. **Right**: dark field image (for $\vec{G} = (2, 0, 0)$) of the sample, showing the bend contours and the regions from where the spectra were taken.

goniometer tilt and the skillfulness of the TEM operator; in the second case the beam tilt brings the electron beam out of the optical axis (where aberrations have a minimum), but usually only a few mrad of tilt are required and this is not enough to cause visible increase in the aberrations of the image; in the last method the relative tilt is controlled by the specimen shift (which is quite accurate), but measurements with different tilts will origin from adjacent but different regions.

The latter method was used in fig. 6.4 to detect the first EMCD effect ever, in 2003 [2]. The measured effect is smaller than expected because the signal is integrated over a rather large and bent area, therefore averaging different values of LCC (especially in the case of the LCC = (2,0,0) spectrum). Another reason is that absorption was not included in the simulation in fig. 6.2.

6.2 Detector shift

As depicted in fig 5.5 a more convenient way to change the helicity of the excitation is to move the $\vec{q}$-selecting aperture in the diffraction plane. First, a single crystalline area of the specimen is identified and tilted to the desired conditions. Working in diffraction mode, the specimen area is selected by an appropriate SAA. The momentum transfer is selected by the SEA, whose size in the diffraction plane is determined by the camera length. The positioning of the Bragg spots with respect to the SEA is made by using the diffraction shift coils situated in the projection stage of the microscope; thus, during the shift, the illumination conditions of the sample do not change and the positioning can be electronically controlled by a script (see appendix). In this setup the spatial resolution is given by the smallest manufacturable SAA (in our case, this represents a field of view of ≈200 nm). The advantages are that there is a good definition of the scattering vector and the specimen is stable in the beam since the illumination is not focused. Moreover since the TEM is operated continuously in diffraction mode, the beam and the lenses are very stable and so is the diffraction pattern, allowing long collection times. The main problem is the low intensity because the electron beam illuminates an area much larger than the SAA, especially when working with parallel illumination, and therefore a large fraction of the electrons is simply absorbed by the SAA and does not contribute to the signal.

In order to prove beyond doubt that the observed effect was indeed MCD, it was decided to perform an EMCD experiment on a sample prepared for and characterized by XMCD at the ELETTRA synchrotron. A thin Fe single crystal film was epitaxially grown in ultra high vacuum on top of a GaAs [001] self-supporting substrate previously thinned and ion milled to electron transparency and protected by 2.5 nm of Cu. Remanent in-plane magnetization could be evidenced by measurements of transverse and longitudinal MOKE: the hysteresis loops indicated a coercive field of 80 Oersted and full remanence in the (100) in-plane easy magnetization direction. The specimens, suitable for both XAS and TEM experiments, were transferred without breaking the vacuum to the APE high energy endstation for XMCD measures. Circularly polarized x-rays from the APPLE-II-type undulator radiation source at the ELETTRA storage ring were focused on a 50 μm spot on the sample surface, at 45 degrees incidence. The dichroic signal was obtained by scanning in energy over the Fe $L_{2,3}$ edge and by reversing the photon helicity, as well as, for a given x-ray helicity, by rotating the sample of 180 degrees around an

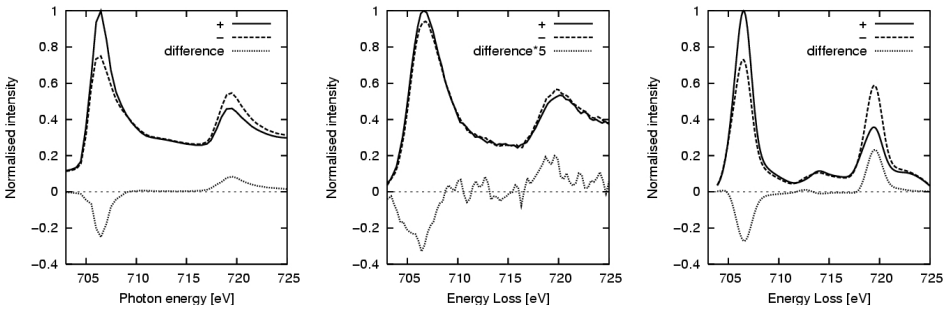

Figure 6.5: **Left**: Fe $L_{2,3}$ XMCD of epitaxial iron on GaAs(001) remanently magnetized along the in plane (100) direction. The full and dashed curves are obtained by reversing the handedness of circular polarized x-rays at each energy. The magnitude of the dichroism is represented by the difference (dotted) spectrum. **Middle**: EMCD measurements at the Fe $L_{2,3}$ edge for 10 nm Fe on GaAs (001) in the two configurations + and -. **Right**: simulations of the EMCD spectra. The dichroic signal is 0.07 for the measured spectra and 0.32 for the simulations. The *r.m.s.* of the noise is 0.03. From Ref. [3].

axis perpendicular to its surface. The remanent in-plane magnetization of the sample was mapped by XMCD all over the relevant parts of the sample in order to assess the uniformity of its magnetization. Representative data are shown in the left panel of fig. 6.5. A further capping layer of 2 nm of Cu was deposited to prevent Fe layer oxidation during the transferring of the samples to the TEM in Vienna.

For the EELS spectra, a flat region of 100 nm radius and uniform thickness was selected in a single grain of Fe. Chemical microanalysis revealed negligible traces of contaminants (C, O and Mo). The magnetization of the iron film in the TEM experiment is forced to be saturated in the out-of-plane direction by a field (created by the objective lens) that is large with respect to the in-plane coercitivity. This is crystallographically identical to the in-plane magnetization used in the XMCD experiment, providing two physically equivalent conditions. The measured spectra are shown in the middle panel of fig. 6.5. The dichroic signal is given by the difference between the two spectra taken at the position + and -. A comparison between the XMCD and the EMCD spectra shows that the observed dichroic signal is smaller than predicted. This can be qualitatively understood by considering the effects of

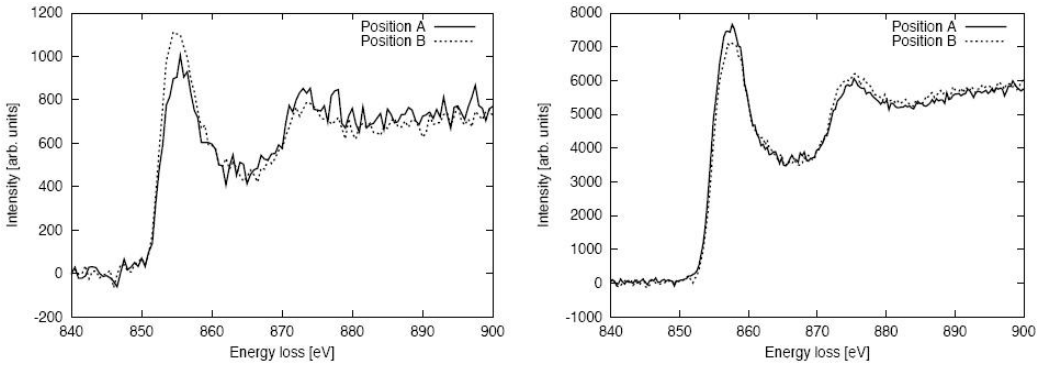

Figure 6.6: EMCD measurements at the Ni $L_{2,3}$ edge with the detector shift method. **Left**: Ni [110] $\vec{G}$ = (0,0,2); LCC=(0,0,1), 200 nm lateral resolution, parallel illumination, 60 s acquisition time. **Right**: Ni [111] $\vec{G}$ =(2,-2,0); LCC=(1,-1,0), 200 nm lateral resolution, optimized beam convergence, 60 s acquisition time. The total intensity is increased with a slightly convergent beam, without losing the dichroic signal. Figure from Ref. [55].

the simplifications used: as the $\vec{q}$-selecting aperture is placed on the (2,0,0) spot of the GaAs substrate, a large part of the collected signal is non-dichroic Bragg and thermal diffuse scattering. Moreover, the integration of the signal over the SEA and the non-zero convergence angle reduces the dichroic effect. Finally, simulations show that an increase of a few nanometers in the thickness would reduce the dichroic signal to half its value. Clearly both EMCD in the TEM and XMCD on the Fe/GaAs sample show comparable spectroscopic features, referred to either remanent or forced magnetization. Furthermore the comparison with the numerical predictions gives the first experimental confirmation of the EMCD effect in Fe.

Converging the beam to a limited extent increases the signal. It was suspected that the higher convergence angle then would reduce the dichroic effect, even below detectability since the LCC position would vary within the illumination cone and the angular resolution is reduced and given by the convolution of the illumination and collection cone. Nevertheless, the experiment yielded a detectable dichroic signal up to a relatively strongly convergent beam. This is related to the fact that the sign of the dichroic signal remains the same in a relatively large interval of LCC and thickness. The relative dichroic signal integrated over this interval is smaller, but the total signal and therefore the total dichroic signal increases because more

electrons now pass through the SAA instead of being blocked (when the beam is converged from parallel illumination, the illuminated area shrinks). Fig. 6.6 compares two setups for the detector shift method: left with nearly parallel illumination and right with increased convergent illumination.

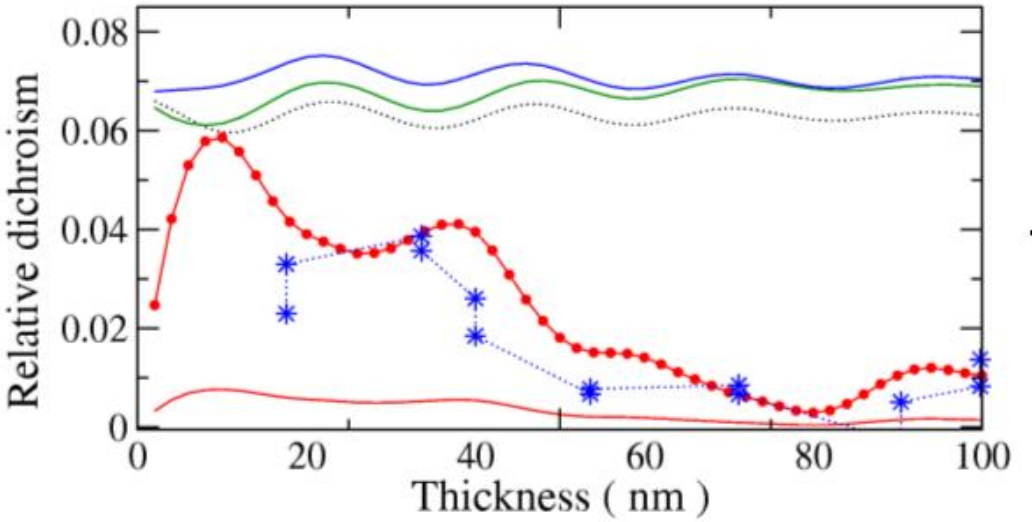

Figure 6.7: Thickness profile of the EMCD at the Co L_3 edge, obtained with the detector shift method in a Cobalt [001] hcp single crystal specimen, tilted to the G = (1,0,0) systematic row and with LCC = (0.5,0,0). The illuminated area is 200 nm in diameter. The experiment (blue asterisks) is compared with DFT based band structure calculations for the same dynamical diffraction conditions (see paragraph 5.6). The blue and green solid curves are DDSCSs calculated for opposite helicities, the dashed black curve is the DFF part of the DDSCS (which does not depend on the helicity). The red line with circles is the relative dichroism defined as difference of DDSCSs divided by their sum, the red solid curve is the absolute dichroism.

As already stated the dichroic signal depends non-linearly on the LCC and the specimen thickness. This is essentially related to the *pendellösung* variations of the strength and relative phase of the interfering Bloch waves as a function of these parameters. With the detector shift method it was possible to reproduce experimentally this dependence: in fig. 6.7 a series of EMCD measurements taken for different values of the thickness is compared to a 10 beams calculation within systematic row approximation for Co [4]. It

is evident from these graphs that, above a certain thickness, the simulation is in good agreement with the experiment. The plots also show that it is of paramount importance to choose the best specimen thickness in order to get a strong dichroic signal.

6.3 Objective aperture shift

A possibility to overcome the limited spatial resolution offered by working in diffraction mode is to use an Objective Aperture (OA) to select $\vec{k_f}$, so that $\vec{q} \perp \vec{q'}$, in the same way the SEA was used before. The microscope is then switched back to image mode and the investigated area in the specimen is selected by the projected SEA and thus depends on the magnification used. The theoretical spatial resolution that can be obtained is in the nanometer range, however the intensity of the signal decreases rapidly as the investigated area becomes smaller and smaller. Another drawback is that the positioning of the OA is done by eye and is therefore not very accurate; moreover, it requires switching back to diffraction mode after the first measurement to shift the aperture between the two positions with opposite helicity. This is a source of instabilities in the system. It is not possible to use the dark-field mode to preselect the positions of the diffraction pattern over the OA, because in dark-field mode it is the tilt of the beam that is changed and this would affect the phase shift (as the LCC is changed). As mentioned, the intensity is low, especially for high lateral resolution, because the electron beam illuminates an area much larger than the projected SEA and this effectively reduces the intensity by which the projected SEA is illuminated, *i.e.* a large part of the incident electrons do not contribute to the signal. Furthermore, in image mode the accurate positioning of the appropriate sample area over the SEA is very difficult. Any error in the position of the specimen may influence the phase if the specimen is bent or the thickness changes. Moreover one would now be limited in the precision of $\vec{q}$ by the smallest OA available (a few mrad).

The achievable spatial resolution is still an advantage; the intensity limitation could be improved by use of a more convergent beam and maybe by the use of a nanoprobe mode instead of a microprobe mode. As the spots in the diffraction pattern become disks when increasing the convergence angle, care must be taken that they do not overlap with themselves or with the OA. The use of preprogrammed motorized apertures may help the selection

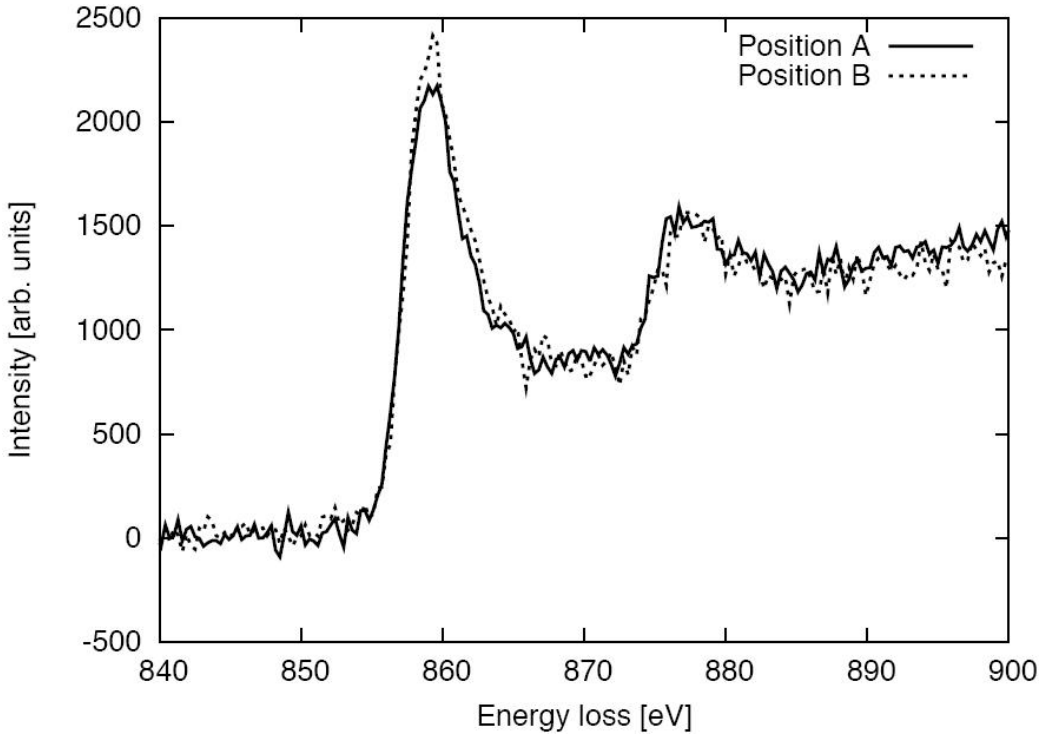

Figure 6.8: Ni $L_{2,3}$ edge in a monocrystalline region of a polycrystalline Ni sample. $\vec{G}$= (2,0,0), LCC = (0,0,0) acquired using an objective aperture to select $\vec{k_f}$. The change in intensity is roughly 10% at the L_3 edge. The sampled area had a thickness of $\approx$ 50 nm and a radius of $\approx$ 75 nm. Figure from Ref. [55].

of the momentum transfer. Fig. 6.8 shows the Ni $L_{2,3}$ edge in the OA shift method.

6.4 LACDIF method

Encouraged by the success of using a moderately converged beam in the previous methods, a completely converged beam technique was tried, using the specimen z-shift to separate the diffraction spots [89, 90]: a Large Angle Convergent DIFfraction (LACDIF) method.

In this geometry, the beam is first completely converged on the specimen in eucentric position [15] (in the image plane one sees a single sharp spot). The sample is then shifted upward, causing more spots to appear because of Bragg scattering. The image plane (which now contains a series of sharp spots similar to a diffraction pattern with parallel incident beam) is then projected onto the SEA. As the illumination is a cone with its base in the condenser system and its apex in the image plane, the area of the (thin) specimen that interacts with the electron beam is a circle with radius proportional to the z-shift and the convergence semiangle α, determined by the condenser aperture. For appropriate values of these two parameters, the investigated area can be reduced to a few tens of nanometers, which is smaller than what could be obtained with a SAA.

Aiming at 10 nm resolution would necessitate to reduce either the convergence semiangle α or the z-shift, or both. There is however a limit to this procedure because the focused spot in the image plane is not point-like. Assuming a perfect lens system and a point-like electron source the spot radius is given by the Airy disk (eq. 2.2) $r = 1.22\lambda/2\alpha$ [15]. When α is reduced, the spot will become larger according to the diffraction limit. That means that z cannot be reduced below a limit given by the condition that the distance s between (000) and the G spot (fig. 6.9) should be larger than 5 times the spot diameter $s \geq 5r$. From fig. 6.9, $s = 2\theta_G z$, hence $d \geq 6a_G$ where a_G is the lattice spacing for planes of reflection G. In practice this limit is of the order of 1 - 2 nm. When the source is partially incoherent and/or the lens has spherical aberration this value is accordingly larger, possibly up to a factor of 5. This seems to be the theoretical limit without C_s correction. A dichroic spectrum with a z-shift of 2.65 μm and $\alpha = 2$ mrad, giving an illuminated area of 11 nm of diameter, was recorded with this technique, but with a very high noise level. The achievable limit for spatial resolution is,

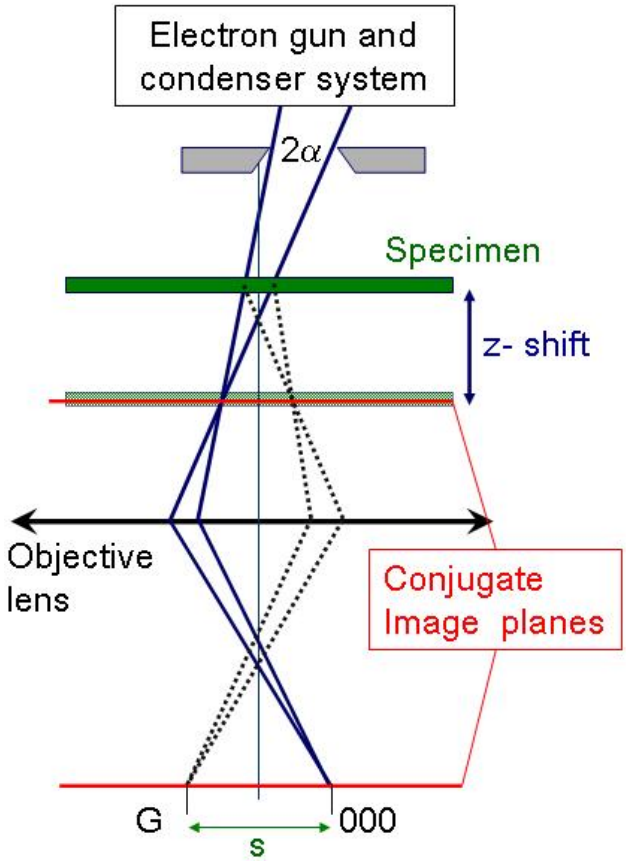

Figure 6.9: Schematic representation of the LACDIF setup: when the specimen is shifted upward from the eucentric position (image plane) by z the illuminated area is a disk with radius αz. Bragg scattering will cause a diffraction pattern to appear in the image plane.

.

in particular, affected by spherical aberration as it increases the size of the spots in the diffraction pattern. With a C_s corrector or a monochromator a spatial resolution of less than 10 nm should be attainable.

The EMCD signature is still detectable after being averaged over a large range of LCC values induced by the convergent illumination. In this illumination geometry the detector shift technique can be used with the difference that the SEA is now coupled to the image plane (equivalent to physically placing the detector in the image plane), where the Bragg spots are sharp and the microscope is operated in image mode. The collection angle is determined by the size of the projection of the SEA on the image plane and can be changed by varying the magnification, which, in this configuration, plays the same role as the camera length and can be made much larger than in the normal TEM diffraction mode.

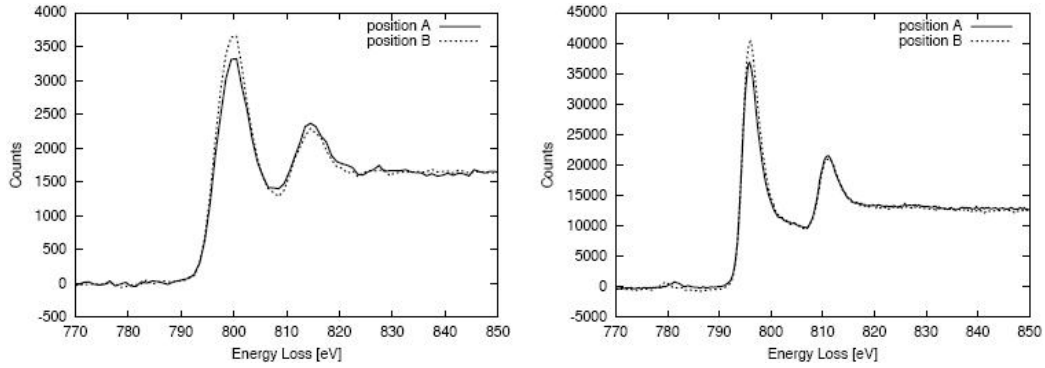

Figure 6.10: $L_{2,3}$ edges in a [001] Co hcp single crystal with orientation: $\vec{G}$ = (1,0,0) LCC = (0.5,0,0). **Left**: detector shift method, 200 nm lateral resolution, 60 s acquisition time; **right**: LACDIF method, 37 nm lateral resolution, 10 s acquisition time. Figure from Ref. [55].

Fig. 6.10 compares spectra obtained from the same specimen area with the detector shift method and the LACDIF method on Co. The modified scattering geometry provides a count rate per eV which is an order of magnitude higher than the one achieved in the previous configuration [3], thus improving significantly the signal to noise ratio. This is essentially caused by the fact that, when no SAA is used and the beam is focused on the area of interest only, all the electrons emitted from the gun contribute to the detected signal. In the detector shift geometry a nearly parallel incident bundle

illuminated a large area of the sample of which only a small fraction could be used. This effectively reduced the intensity by which the area of interest is illuminated, *i.e.* a large part of the incident electrons did not contribute to the signal. The increase in the count rate per eV allows a reduction of the acquisition time, thus limiting the effects of beam instability, specimen and energy drift. The shorter acquisition time, combined with the finer energy dispersion, improves the energy resolution with which the $L_{2,3}$ edges are recorded. In the older setup the L_3 has a Full Width at Half Maximum (FWHM) of 8 eV, compared to the 3.6 eV achieved with the new method (fig. 6.10).

The drawback of this setup is that, as it was the case for the OA shift method, the positioning of the detector has to be done by eye, thus limiting the precision in the selection of k_f. There are also other technical problems related to the proper setting of beam tilt, selected area and z-shift which render this geometry more difficult in practical applications.

6.5 The q vs. E diagram

The q vs. E diagram provides a mean to record the spectra with opposite chirality in a single acquisition, thus reducing the negative effect of specimen and beam drift or other instabilities by effectively halving the collection time. This method can be used only if a diffraction pattern is projected on the SEA, therefore either with the TEM operated in diffraction mode or with a LACDIF illumination.

To obtain such a diagram it is necessary to rotate the diffraction pattern, therefore a rotational holder is needed. Alternatively, changing the current in the projection lenses will induce a rotation of the image, coupled with a change of the camera length, but care should be taken not to permanently modify the manufacturer's lens current specifications in the registry. It is also possible, lacking a rotational holder, to remove the specimen from the TEM and manually rotate it inside the holder with a pair of tweezers, however this tedious procedure rarely grants a good enough sensitivity.

In the following this technique is demonstrated on a Co single crystal electropolished sample. The dichroic signal is obtained by first tilting out of the [001] zone axis to a two-beam case where only the $(0,0,0)$ and $\vec{G} = (1,0,0)$ reflections are strongly excited. With LACDIF illumination one obtains a diffraction pattern which is then projected onto the SEA. The beam (with a

convergence semiangle of $\alpha = 2$ mrad) is focused onto a 18 ± 3 nm thick area of the Co specimen which is then shifted upwards from the eucentric position by $z = 9.25\,\mu$m. The diameter of the illuminated area is $d = 2\alpha z = 37$ nm, accurate to 5%. Using a rotational sample holder, the reciprocal lattice vector $\vec{G}$ is then aligned parallel to the energy dispersive axis of the CCD camera, so that a q-E diagram can be recorded as depicted in fig. 6.11. As explained in paragraph 4.3, the quadrupoles of the energy filter collapse (integrating the signal in the q_x dimension) the circular area to a line in q_y when the system is switched to spectroscopy mode. The q_x axis is now replaced by the energy dispersive axis and any information depending on q_x is integrated and cannot be resolved. Each pixel of the image obtained displays the intensity of the electron scattering for a particular value of the energy lost and of the scattering angle in the y direction. This method allows to record not only both spectra A and B with a single acquisition, but the entire range of spectra with different q_y values comprised within the SEA. It should be noted however that the integration area in the q_x dimension is different for every value of $|q_y|$ and given by:

$$\Delta q_x = \sqrt{\frac{G^2}{4} - q_y^2}. \tag{6.3}$$

The dichroic signal is obtained by tracing the spectral intensity at points A and B in fig. 6.11, and taking their difference. With an acquisition time of 15 s and an energy dispersion of 0.3 eV/channel the intensity at the L_3 peak was about 13,500 counts (after background removal). *Ab initio* DFT simulations of the dichroic signal were performed including the effects of thickness, tilt of the incident beam, position of the detector, as well as the integration over q_x in the range dictated by the use of a circular SEA (eq. 6.3). Up to 8 beams were used for the calculations of the MDFFs. A comparison with the experiment is given in fig. 6.12 for the L_3 edge of Cobalt. The agreement is very good between -0.8 and 0.8 G with some discrepancy appearing at larger scattering angles. This can be due to the faint Bragg spots outside the systematic row (which are neglected in the simulations) and to the fact that the SEA is not exactly in the spectral plane of the energy filter and is therefore not sharply defined. The error bars correspond to the (2σ) Poissonian noise calculated for the theoretical signal using the number of electrons contributing to the signal as determined from the experimental data.

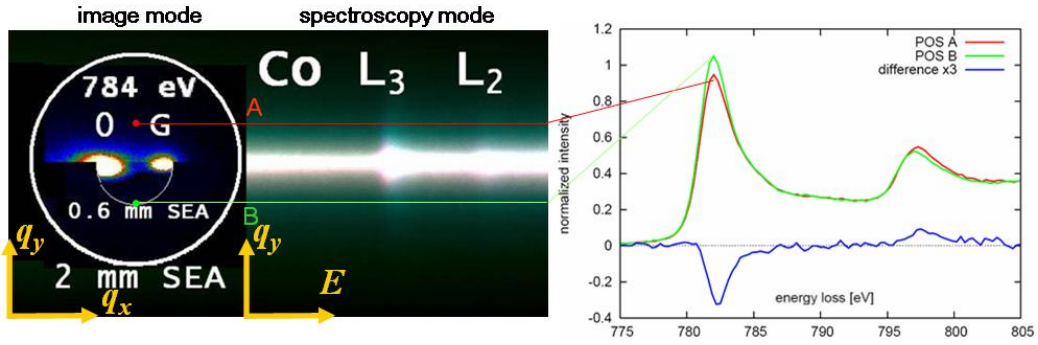

Figure 6.11: **Left**: Energy filtered diffraction pattern at 784 eV energy loss using a slit width of 20 eV. The sample was oriented in the two-beam case, capturing both reflections within the SEA. When the spectrometer is switched to spectroscopy mode, a q-E diagram is obtained. **Right**: EMCD spectra obtained as line traces from the q-E diagram for values of q_y corresponding to the positions A and B on the Thales circle. Courtesy of Michael Stöger-Pollach.

6.6 CBED setup

In the LACDIF setup it was shown that relatively large convergence angles still yield a significant dichroic signal. A CBED configuration was then tried to further improve the possible spatial resolution without sacrificing spectral intensity. Similarly to LACDIF, the beam is focused on the specimen but then the microscope is switched to diffraction mode. A diffraction pattern with large disks will appear. The size of these disks (*i.e.* the convergence angle) is defined by the condenser apertures and is about 2-3 mrad in this experiment. The convergence angle should be chosen so that the disks in the diffraction pattern do not overlap. The specimen (an hcp Co single crystal) is then tilted 5 degrees away from the [001] zone axis to excite the (110) systematic row. Since now for every possible k_f there is a combination of circular and linear polarization, there is no reason to expect that the maximum of the dichroic signal is at the Thales circle, especially if all significant Bragg spots are taken into account. Indeed simulations [88] have shown that for a three beam case (*i.e.* LCC = (0,0,0)) the maximum of dichroism is obtained for the positions A and B of fig 6.13. As opposed to the two-beam case this geometry has the advantage that one avoids any spectral difference not

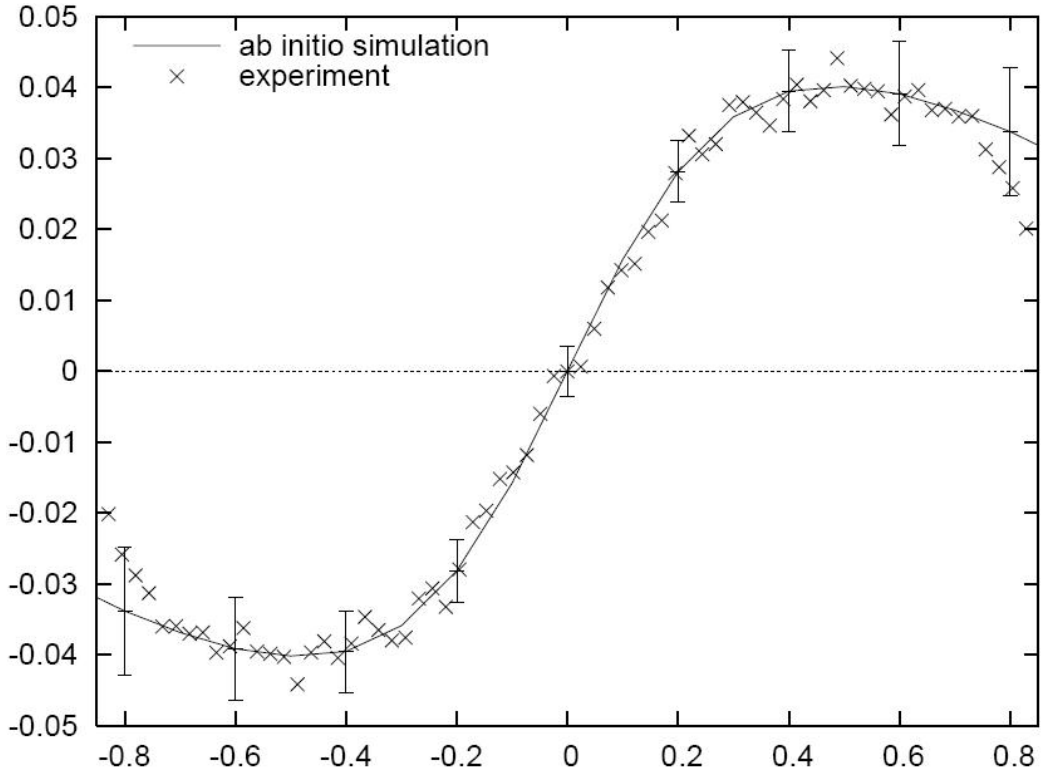

Figure 6.12: Dichroic signal at the Cobalt L_3 edge as function of the scattering angle q (in unit of G) in the direction perpendicular to the Bragg scattering vector $\vec{G}$. Positions A and B (see fig. 6.11) correspond to points q/G = 0.5 and -0,5 respectively. Comparison between *ab initio* simulation (line) and experimental data (crosses), obtained as line trace along the L_3 edge in the q-E diagram of fig. 5.16, lower row, and fig. 6.11, respectively. In both cases the values shown are obtained by first integrating the signal at L_3 over a range of 5.1 eV and the q_x determined by the SEA (virtual in the case of the simulations) and then subtracting the corresponding value for $-q_y$. The plot results to be antisymmetric by construction (*i.e.* the origin is an inversion center). The error bars correspond to simulated Poissonian noise (2σ). Figure from Ref. [91].

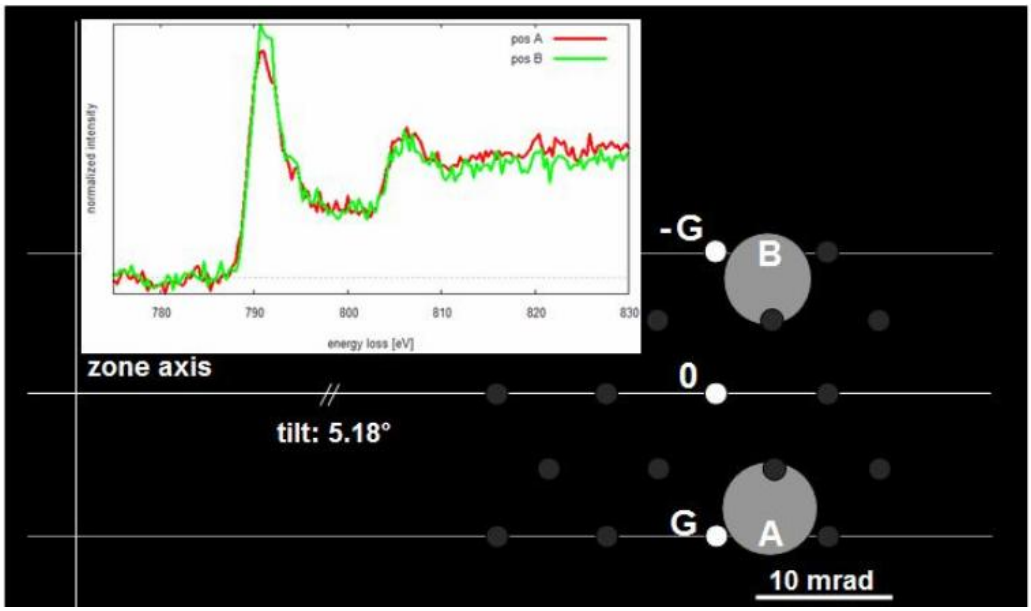

Figure 6.13: CBED configuration. The Co crystal is tilted in the (-1,1,0) direction from the [001] zone axis to a three beam case *i.e.* with $\vec{G} = (1, 1, 0)$ and -$\vec{G}$ equally excited. The other Bragg spots are shown for completeness but are very weak and do not appear in the energy filtered image of the diffraction pattern taken at the $L_{2,3}$ edge. The detector shift technique is used without SAA to record spectra from positions A and B (the gray circles indicate the SEA in such positions). The spatial resolution is given by the size of the focused spot, in this case $\approx$ 3 nm. Figure from Ref. [70].

related to dichroism: when one goes beyond the systematic row approximation, the Bloch coefficients for the positions A and B on the Thales circle are slightly different. This is due to the fact that the two-beam case is achieved by tilting away from a Zone Axis in a direction perpendicular to $\vec{G}$. Therefore the k_f corresponding to positions A and B will form different angles with respect to the Zone Axis. It is also possible to show that a large collection angle improves the signal-to-noise ratio [88]. The other Bragg spots are only weakly excited and can thus be neglected even if they happen to be on the projection of the SEA (as it is the case of the (0,1,0) spot).

The success of the CBED setup means that EMCD should be possible in STEM mode, where the electron beam is focused into a small probe and used to scan the sample and produce an image pixel by pixel, usually by collecting the scattered electron with a high-angle annular dark field in the diffraction plane. A spatial resolution in the sub-Ångstrom range can be routinely achieved. Since the EMCD is a difference of Fe signals, its theoretical geometric resolution must be the same. But this is only true for the same SNR. The smaller SNR in the EMCD signal reduces this limit. Therefore the EMCD signal has a spatial resolution given by the beam diameter which cannot be reduced below a certain limit because spectra obtained with smaller electron probes have a lower intensity and low signal to noise ratio. Experimentally it was found that a nominal spot size of 1.7 nm yielded a signal strong enough for detection of EMCD in Fe.

To calculate the resolution limit for EMCD one would need a test sample with several thin layers of alternating ferromagnetic and non-ferromagnetic material, ideally starting from 0.1 nm and then slowly increasing. The spatial resolution is then given by the thinnest gap between ferromagnetic layers that can be resolved according to the Rose criterion [92] for detection of a faint object in a noisy data set. It states that the signal I defining the object must exceed the background noise by a factor of at least 3 in order to be recognized as a structure. Such specimen would have fixed tilt in one direction because the interfaces have to remain projecting and this limits the choice of the systematic row to the one with $\vec{G}$ perpendicular to the interface and LCC to the three beam case.

Early measurements [93] on a FeAu multilayer sample (fig. 6.14) confirmed this possibility and were able to resolve the thinnest Au layer (5 nm) suggesting a spatial resolution of 1.7 nm or better.

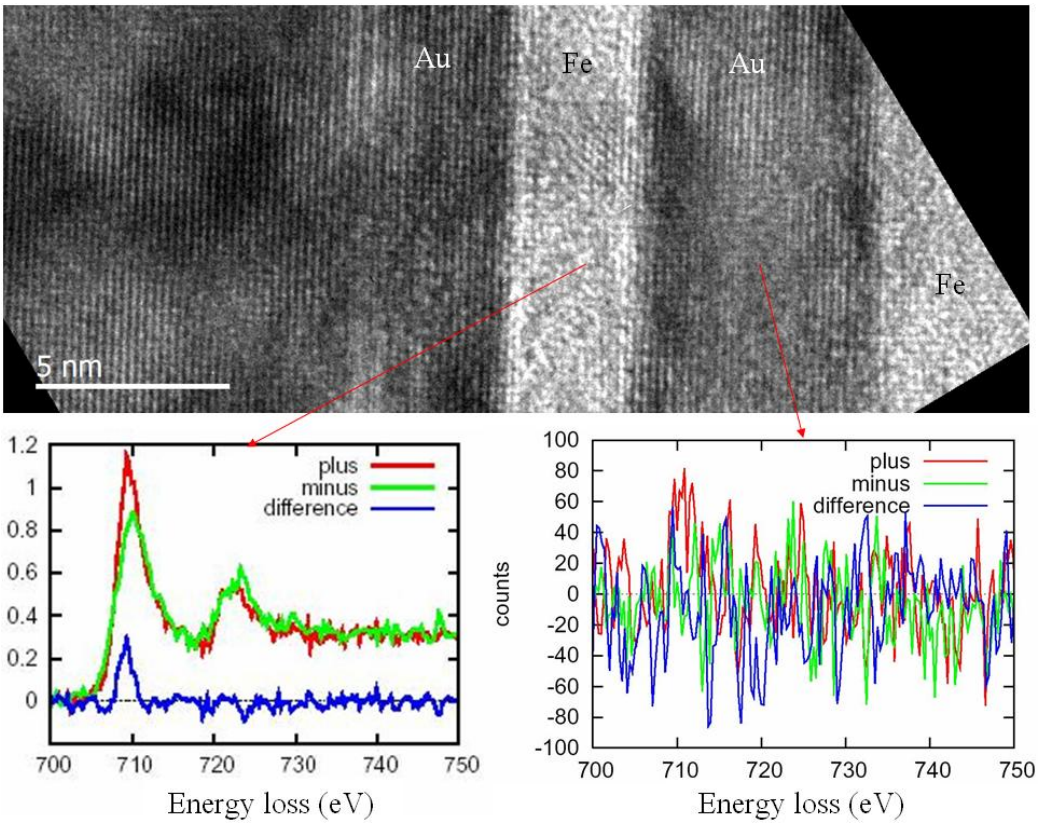

Figure 6.14: High-resolution TEM image of the FeAu multilayer sample (above) with EMCD spectra taken at the Fe $L_{2,3}$ edge in the 3 nm wide Fe layer (below, left) and in the 5 nm wide Au layer (below, right). The dichroic signature is clearly visible at the Fe L_3 edge in the iron layer, whereas only noise can be detected (after background subtraction) in the gold layer. The size of the beam is nominally 1.7 nm. Courtesy of Michael Stöger-Pollach.

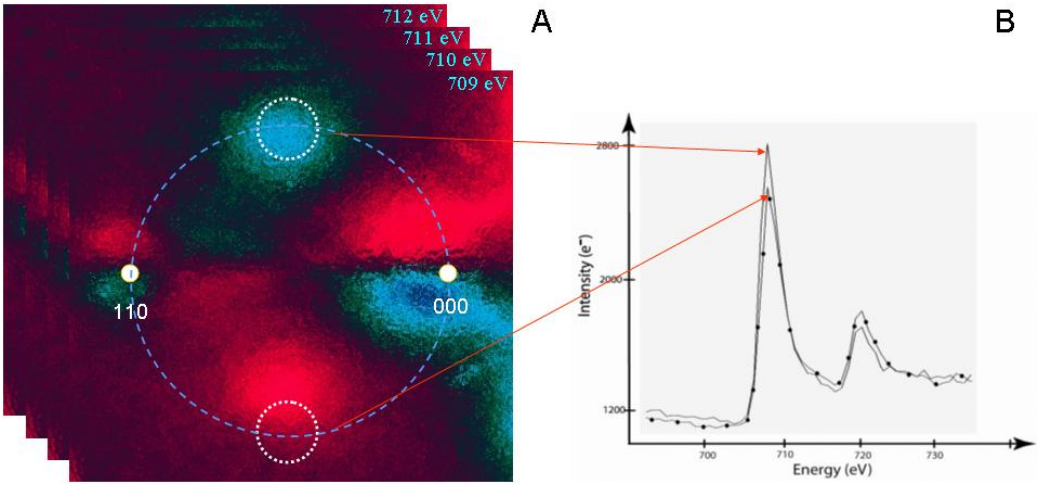

Figure 6.15: ESD **A**: a series of energy filtered images of the diffraction pattern of bcc Fe is acquired with an energy window of 1 eV. The one corresponding to the peak of the L_3 edge (at 709 eV) is then mirrored with respect to the line connecting the (0,0,0) and (1,1,0) spot and then subtracted from itself. The result is a map of the absolute dichroic signal. **B**: a virtual aperture is placed in every image of the series and the signal within that area is integrated. A plot of this integration as function of the energy loss gives the spectrum for that particular scattering angle. The spectra were taken in Toulouse on a C_s corrected Tecnai F20 equipped with a GIF tridiem. From Ref. [70].

6.7 Energy spectroscopic diffraction

An alternative approach to EMCD experiments is the Energy Spectroscopic Diffraction or Imaging (ESD or ESI) [94]. In ESD the diffraction pattern is projected on the SEA and a series of energy filtered images is acquired, scanning the $L_{2,3}$ edge. In this case each pixel of the CCD camera act as a detector and the signal for several different chiral excitations is recorded simultaneously. From the EELS data cube (see paragraph 4.3) thus obtained the dichroic signal can be extracted in two ways (fig. 6.15 shows an example for bcc-Fe).

One can take the energy filtered image of the diffraction pattern recorded for the energy loss corresponding to the L_3 (or L_2) peak. To improve the

SNR all images corresponding to the L_3 edge can be summed up. The line connecting the 000 and the diffracted spot is used as a mirror plane to change the value of every pixel to the one of the pixel with same x and opposite y coordinate. This mirrored image is subtracted from the original image to obtain, point by point, the dichroic signal as difference between the L_3 peak values of spectra with same q_x but opposite q_y. For the two-beam case, the maximum is expected to be at the opposite points in the Thales circle. Alternatively, one can imagine placing a virtual aperture in the same position in every image of the recorded diffraction pattern and measure the intensity falling within this aperture as function of the energy loss at which the image was recorded. The plot thus obtained is nothing else than the energy loss spectrum that would have been recorded with that particular scattering angle (*i.e.* with the SEA in the place of the virtual aperture). Extracting the corresponding spectrum from the opposite position on the Thales circle produces an EMCD measurement.

Another measurement taken in the three-beam case, *i.e.* exciting the (1,1,0) systematic row with LCC = (0,0,0), provides the opportunity to apply to this case the considerations developed in paragraph 5.7. The approximated thickness of the sample in this measurement is estimated to be 16 nm. A LACDIF illumination is used with a convergence angle of 7.8 mrad and an illuminated sample area of around 40 nm diameter. Isochromaticity and drift are corrected for by a Digital Micrograph script. Non-isochromaticity and drift in the image plane should be removed in a first step since these artifacts can strongly distort the EMCD signal. This step is however only necessary for EFS of diffraction patterns and is far less a concern when experiments are taken by making use of two EELS spectra acquisitions (like in the detector or OA shift method) or in the case of the q-E diagram. Conventional power law background subtraction is performed on each pixel in the q_x, q_y, E datacube. This datacube can now be used to extract the EMCD signal making use of different aperture size and positions, which is of special interest now as it allows to compare theoretical predictions with experiments. Different apertures sizes are simulated by convoluting the data with a circular aperture of a given radius.

Fig. 6.16 shows an integrated slice of the datacube around the L_3 edge with superimposed the optimal positions of different circular apertures. Note the reasonably good agreement between the predicted optimal positions in fig. 5.19 for the same thickness. The obtained dichroic signal as a function of the aperture size is shown in fig. 6.17. It is evident from this figure that the

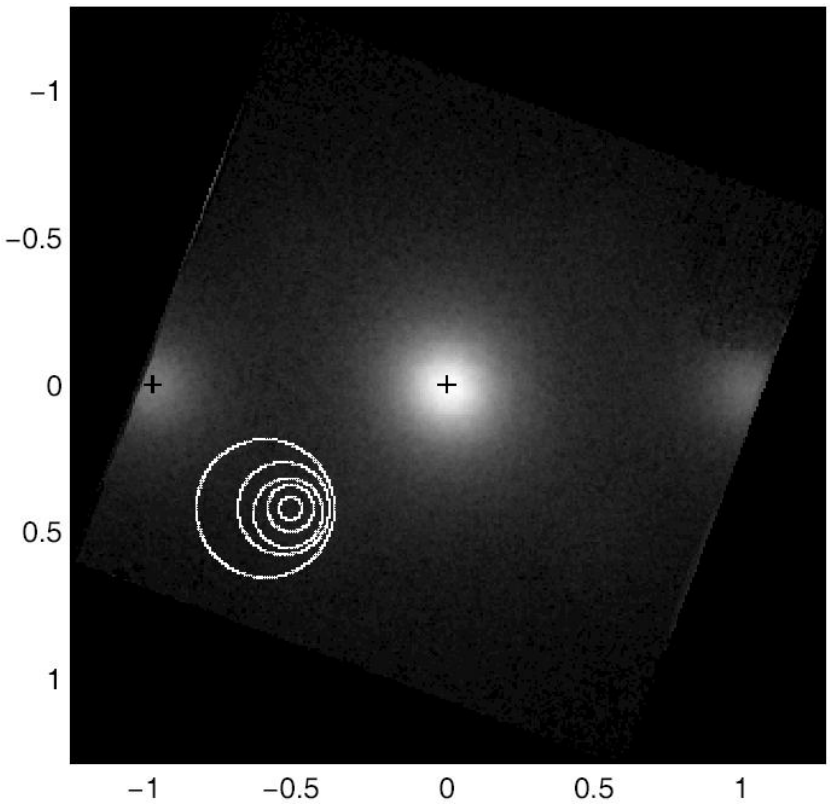

Figure 6.16: Experimental optimal aperture positions drawn on an integrated energy slice around the Fe L_3 edge. From Ref. [88].

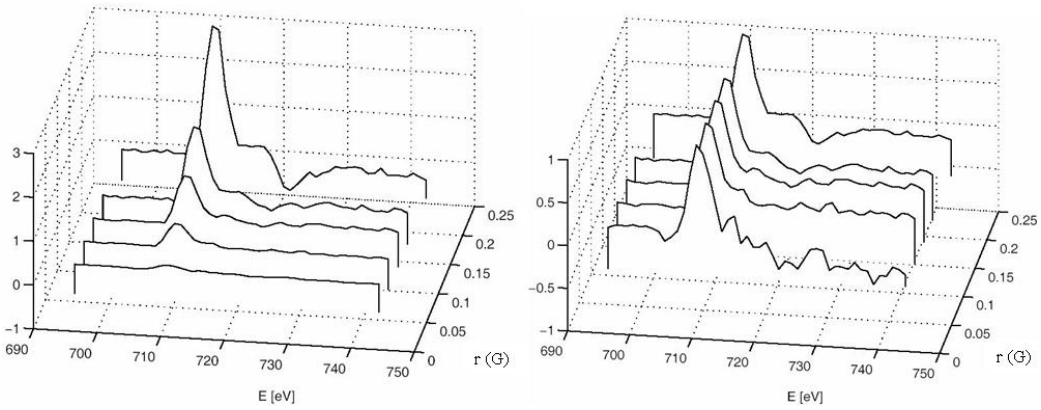

Figure 6.17: **Left**: absolute EMCD signal vs. aperture size, note the increase of the dichroic signal as the aperture size increases. **Right**: normalized absolute EMCD signal vs. aperture size, note the reduction in noise as the aperture increases. From Ref. [88].

signal increases significantly for bigger apertures. The improvement in SNR can more easily be seen when the signal is scaled to the maximum. A rough estimate of the SNR can be made by calculating the variance in the pre-edge region and comparing it to the variance in the $L_{2,3}$ region which can be seen as an estimate of the signal power. Fig. 6.18 shows this estimate and clearly indicates a strong increase in SNR as the aperture radius increases. As the maximum aperture size was limited in this experiment, the expected plateau visible in fig. 5.23 is not reached; however the experiment clearly confirms the significant gain in SNR by taking a larger aperture in an optimal position. The experimental dichroic signal, obtained for the largest aperture allowed by the experimental data cube, is also shown in fig. 6.18.

The dynamical simulation (figs. 5.19 and 5.22) and the experiment also showed that it is advantageous to shift the aperture slightly away from the central (0,0,0) spot to the diffracted spots (G). This can be understood as the position where an equal inelastic scattering amplitude from (0,0,0) and (1,1,0) leads to a maximum in the EMCD effect (compare with fig. 5.16 to see how the *pendellösung* effect influences the position of the maximum of the dichroic signal in the diffraction plane).

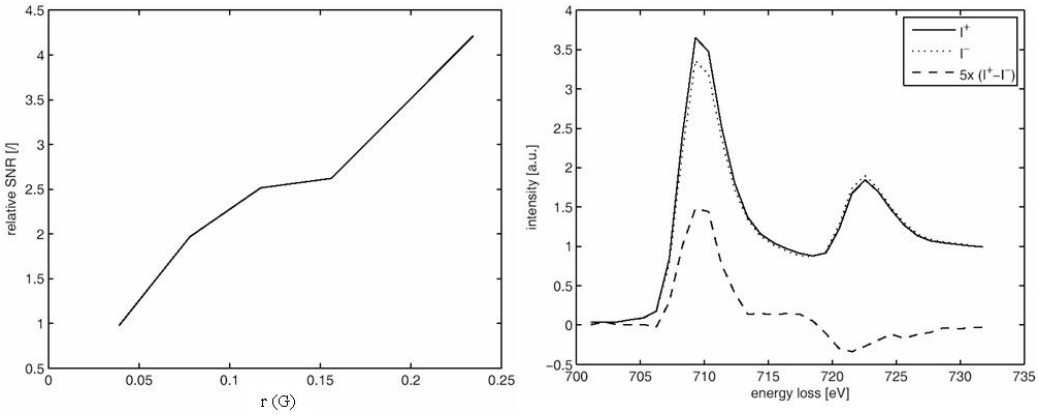

Figure 6.18: **Left**: estimated relative SNR of the absolute dichroic signal vs. aperture size, note the strong increase in SNR as the aperture radius increases. **Right**: experimentally obtained EELS spectra in two symmetrical positions I^+ and I^- and absolute EMCD signal $I^+ - I^-$ for the optimal aperture size and position. The EMCD signal is enhanced by a factor of 5 to make it better visible. From Ref. [88].

6.8 Monitoring magnetic phase transitions

In this paragraph a first practical application of the EMCD effect is detailed. Since EMCD depends on the magnetization of the sample, it is possible to detect changes in the magnetic properties of matter. Monitoring magnetic phase transitions of magnetic nanostructures opens fascinating perspectives for future spintronics applications. Such a phase transition could be demonstrated in a crystal of $Pr_{0.5}Sr_{0.5}MnO_3$ [95]. This compound is antiferromagnetic below 160 K, paramagnetic above 267 K and ferromagnetic in the remaining range (fig. 6.19). This was confirmed by temperature-dependent EMCD measurements at the Mn $L_{2,3}$ edge (640 eV). The O K edge (532 eV) was recorded as well to identify eventual artifacts in the acquisition and did not show any dichroic effect, as expected. The signal was obtained from a single crystalline region of 130 nm radius.

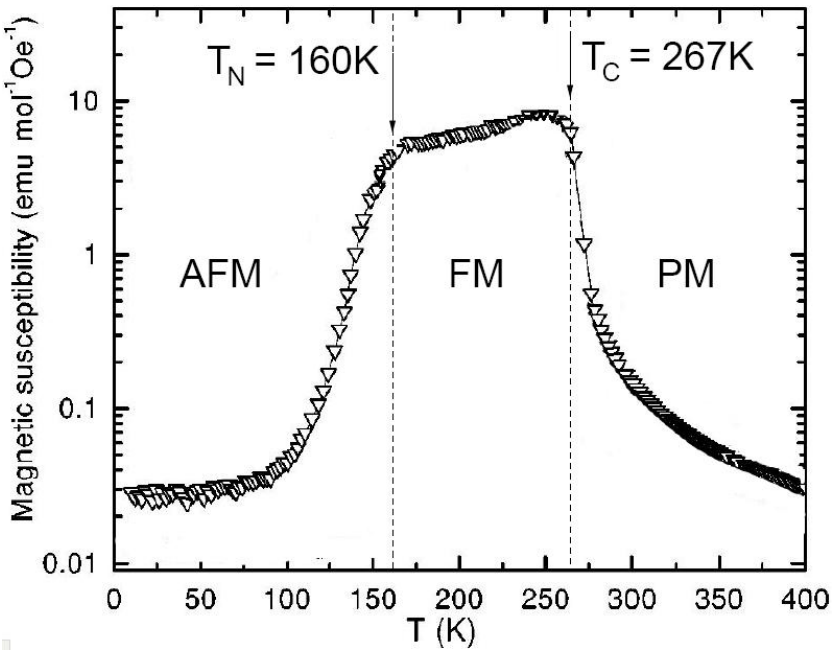

Figure 6.19: EMCD magnetic phase transition. $Pr_{0.5}Sr_{0.5}MnO_3$ is ferromagnetic only within a defined temperature range (figure modified from Ref. [95]).

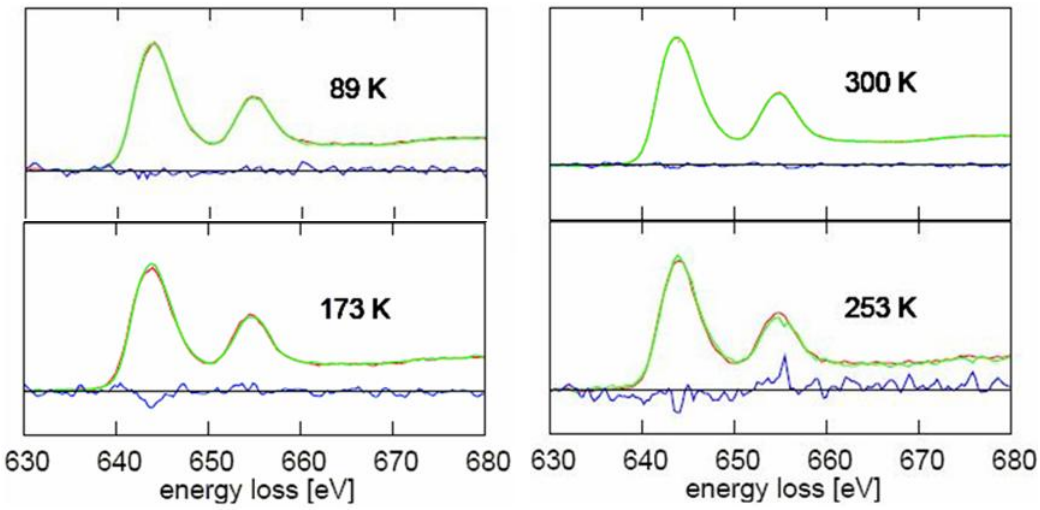

Figure 6.20: When EMCD measurements are performed with a temperature controlled cryoholder it is possible to detect the change in the magnetic character of the sample from its dichroic signature. For the sake of clarity the differences are enhanced by a factor of 5. Only the two spectra in the bottom of the figure are in the ferromagnetic range and thus show dichroic features rising above the noise level. Figure from Ref. [70].

6.9 Test with a non magnetic material

In order to ensure that the effects measured are really the TEM equivalent of the XMCD and not an artifact, EMCD measurements have been performed on non-magnetic materials such as metallic Titanium, Rutile (TiO_2) and Copper Oxide (CuO). Several different methods have been tested, with different values for the tilt angle and the specimen thickness. Some examples are reported in fig. 6.21. All measurements evidenced no difference in the ELNES of the spectra after variation of the chirality of the excitation.

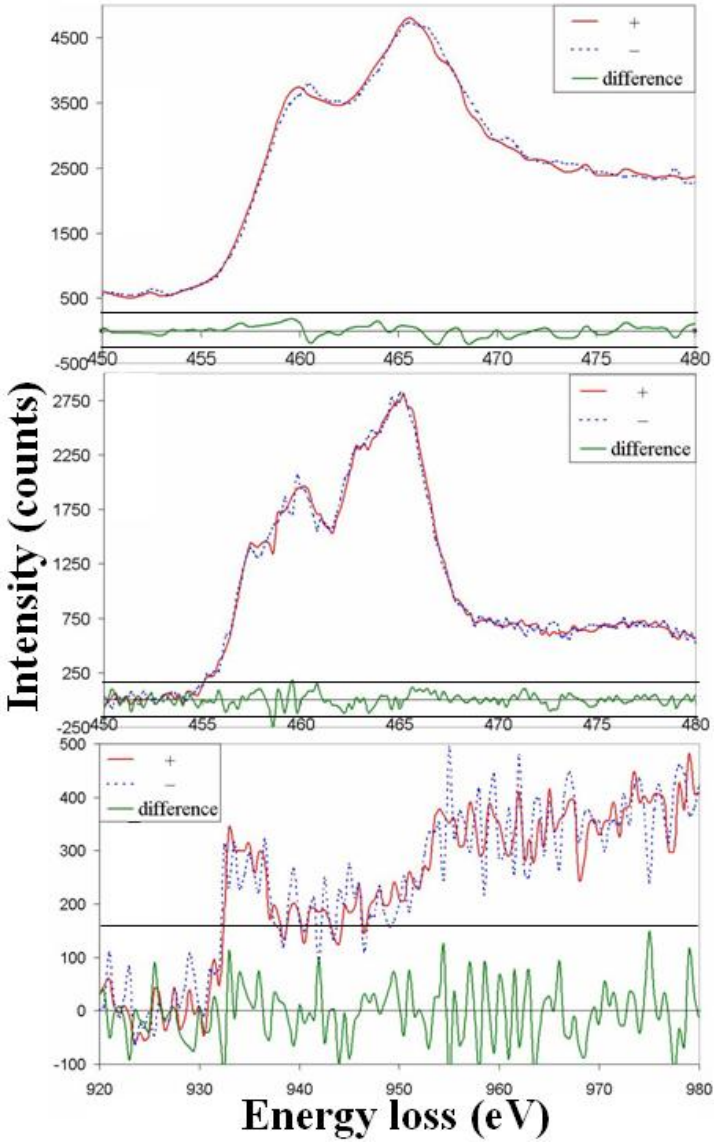

Figure 6.21: $L_{2,3}$ edges for non-magnetic materials taken with the detector shift technique. From top to bottom: metallic Titanium, Rutile (TiO_2) and CuO. The root mean square σ of the noise is 88, 67 and 57 respectively and the horizontal lines represent the $\pm 3\sigma$ limit. As expected, there is no significant difference in the intensity ratio of the edges. This excludes the possibility that detected dichroic measurements could have been artifacts.

Chapter 7

Alternative techniques and open questions

EMCD is a relatively new phenomenon whose study has just started spreading to labs worldwide. It still presents many aspects that are unclear or haven't been thoroughly observed and understood. It is comparable to 1492's America: a newly discovered continent that is being charted by this first expedition '*to boldly go where no one has gone before*'. The present dissertation leaves many open possibilities with respect to alternative techniques and setups or possible applications. They include: the possibility to use other methods to obtain a superposition of two coherent wave interfering to produce a chiral excitation (a biprism being one such mean); the option to develop new experimental conditions and improve existing ones, with the aim of pushing EMCD up to the theoretical limits of the TEM (in term of spatial and energy resolution, for example); a deeper and more systematic investigation of the many experimental parameters characteristic of an EELS measurement; the comparison with the quality and type of information that can be obtained by EMCD with respect to XMCD, underlining what features have to be the same and what have to be different.

In the following paragraph these issues will be addressed.

7.1 A note on sum rules

A complete set of ELNES sum rules [96] has been derived using methods presented in Ref. [45]. Independently a simplified form of EMCD spin and

orbital sum rules based on their XMCD counterparts [23, 49] was derived in Ref. [97]. The new EMCD sum rules can be written as

$$\frac{\int_{L_3}\left[\left(\frac{\partial^2\sigma}{\partial E\partial\Omega}\right)_{pos2}-\left(\frac{\partial^2\sigma}{\partial E\partial\Omega}\right)_{pos1}\right]dE-2\int_{L_2}\left[\left(\frac{\partial^2\sigma}{\partial E\partial\Omega}\right)_{pos2}-\left(\frac{\partial^2\sigma}{\partial E\partial\Omega}\right)_{pos1}\right]dE}{\int_{L_3+L_2}\left[\left(\frac{\partial^2\sigma}{\partial E\partial\Omega}\right)_{pos2}+\left(\frac{\partial^2\sigma}{\partial E\partial\Omega}\right)_{pos1}\right]dE}=$$

$$K\left(\frac{2}{3}\frac{\langle S_z\rangle}{N_h}+\frac{7}{3}\frac{\langle T_z\rangle}{N_h}\right) \tag{7.1}$$

and

$$\frac{\int_{L_3+L_2}\left[\left(\frac{\partial^2\sigma}{\partial E\partial\Omega}\right)_{pos2}-\left(\frac{\partial^2\sigma}{\partial E\partial\Omega}\right)_{pos1}\right]dE}{\int_{L_3+L_2}\left[\left(\frac{\partial^2\sigma}{\partial E\partial\Omega}\right)_{pos2}+\left(\frac{\partial^2\sigma}{\partial E\partial\Omega}\right)_{pos1}\right]dE}=K\frac{1}{2}\frac{\langle L_z\rangle}{N_h} \tag{7.2}$$

where $\langle S_z\rangle/N_h$, $\langle L_z\rangle/N_h$ and $\langle T_z\rangle/N_h$ are respectively the ground state expectation values of spin momentum, orbital momentum, and magnetic dipole operators per hole in the d bands. The coefficient K contains all the information related to the dynamical effects. The ratio of spin to orbital moments can be obtained without knowledge of the prefactor K.

For Fe, neglecting the contribution of the magnetic dipole operator, this measurement has given $\langle L_z\rangle / \langle S_z\rangle = 0.18 \pm 0.05$ [97]. This result is higher (but with the same order of magnitude) than the values 0.124 [98], 0.088 [99], 0.133 [49] and 0.086 [24] which have been obtained from neutron scattering data, gyromagnetic ratio methods or XMCD spectra.

A very strong dichroic signal was detected for Co, for which the ratio orbit/spin moments is $\langle L_z\rangle / \langle S_z\rangle = 0.28 \pm 0.05$ as compared to an XMCD value of 0.19 [24]. It is not quite clear if these higher values signify a systematic tendency or if the noise in the experiment, which is especially significant for the fainter L_2 edge, is responsible for these discrepancies. Longer exposure times with very stable specimens are needed to clarify this point.

7.2 Unexplained features of EMCD

In fig. 6.4 a double step arc tangent function f_{bckg} was fitted to the measured EELS spectra to remove the background. Its analytical expression is

$$f_{bckg} = h\left[\frac{2}{3}\left(\frac{1}{2}+\frac{1}{\pi}\arctan\frac{E-L_3}{\delta_E}\right)+\frac{1}{3}\left(\frac{1}{2}+\frac{1}{\pi}\arctan\frac{E-L_2}{\delta_E}\right)\right] \tag{7.3}$$

with L_3 and L_2 being the energies of the respective edges, δ_E the experimental energy resolution and h a fit parameter corresponding to the baseline after the edges (which is expected to be an horizontal line, otherwise the measurement should be discarded and repeated). This background fitting function is widely used in the XMCD community and it is generally attributed to the spectral contributions of the free s-DoS above the Fermi energy (transitions $p \rightarrow s$ are not dipole forbidden). This background is present also in EELS measurements (after proper removal of the multiple scattering background AE^r) but it appears to be missing in the simulated spectra (compare with fig. 6.5). An examination of the formulas involved in the calculation reveals that indeed the transitions $p \rightarrow s$ are properly taken into account and that their contribution is not visible in the simulated spectra because the free s-DoS is negligible with respect to the d-DoS. A comparison with simulated XMCD spectra would clarify if this is a fault of the calculation (if the increased background is present in XMCD simulations) or if it is a flaw of the theory (if also in XMCD simulations the double step background is much lower than in experiments).

Another anomaly of EMCD has been detected at the L_2 edge, which often shows very small dichroic effect. The ratio of the intensity of the L_3 with respect to the L_2 edge in case of unpolarized excitation is 2:1. Therefore, if one assumes complete quenching of the angular momentum, from the selection rules [23, 49, 96, 97], the expected absolute variation of the integral intensity for the two edges should be the same. Even allowing for a more important broadening of the L_2 and a SNR lower by a factor $\approx \sqrt{2}$, in several EMCD measurements the dichroic effect at the L_2 was not detectable whereas the effect at the L_3 edge was quite strong (see for example fig. 7.1).

Multiple scattering may in part explain this behavior: part of the L_3 signal is mixed with the L_2 signal and, considering the expected symmetry between the L_3 and the L_2 excitations, this mixing will cancel out part of the expected EMCD signal. However multiple scattering should not affect so heavily spectra taken from thin specimens (which is usually the case in EMCD) and even then, multiple scattering effects can in principle be removed by deconvolution with a low loss spectrum, but the angular dependence of the scattering must be taken into account in the deconvolution. Another possible explanation is that the assumption of complete quenching of the orbital angular momentum $\mathbf{L}$ is wrong. The origin of the quenching is usually attributed [100] to the non-centrality of the crystal electric field, which in turn makes $\mathbf{L}$ a bad quantum number (as angular momentum is conserved only

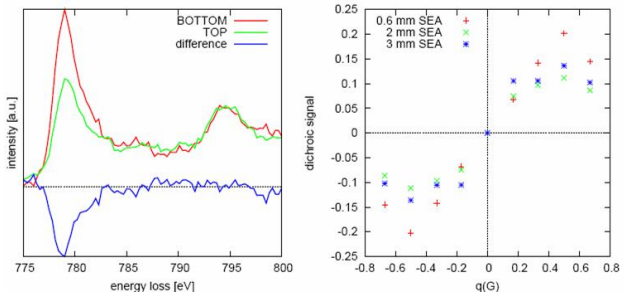

Figure 7.1: **Left**: EMCD spectra taken at the Co $L_{2,3}$ edge in a two-beam case ($\vec{G} = (1, 1, 0)$) with LACDIF illumination and q-E diagram, similarly to fig 6.11. The asymmetry at the L_3 edge is $\approx 20\%$ yet no effect is visible at the L_2 edge. **Right**: a $\Delta\sigma$ vs. q plot (analogous to fig. 6.12 for different values of the SEA (and thus of the integration range in q_x) shows for the L_3 the expected behavior as function of q_y. Courtesy of Michael Stöger-Pollach.

in a central potential). In the case of $3d$ transition metals the states $p_{\pm 1,0}$ are not a good basis, whereas the states p_x, p_y and p_z form a good basis. It can be easily verified that the matrix elements of L_z for these orbitals are zero. However this does not hold true if the target atom is not in a perfect crystal and the effects of the crystal field are reduced. This could be the case if there is significant strain in the area of measurements (due for example to deformations or proximity to an interface) or the atom is on the surface. In this case the quenching is not complete and this translates into an important contribution of the angular momentum to the total magnetization, which in turn means a change in the expected ratio of the asymmetries at L_3 and L_2. XMCD measurements [101] on two-dimensional, one-dimensional crystals and isolated atoms have confirmed this trend.

Another anomaly which may or may not be related to the one detailed above is illustrated in fig. 7.2. The figure is obtained from a q-E diagram (such as in figs. 6.11 and 6.12) by subtracting from every spectrum (obtained as a line profile for a certain q_y) the average of all spectra. In this way the plot is not forced to be antisymmetric with respect to q_y as it was the case in fig. 6.12 and, indeed, it is not antisymmetric even if one would expect so (*i.e.* $\sigma(q_y) \neq -\sigma(-q_y)$) from eq. 5.30. There it is clearly visible that when one simply changes $q_y \rightarrow -q_y$ (and correspondingly $q'_y \rightarrow -q'_y$) only the imaginary part of the MDFF changes (and only in sign) and therefore

the contribution to the asymmetry should be identical in modulus for q_y and $-q_y$.

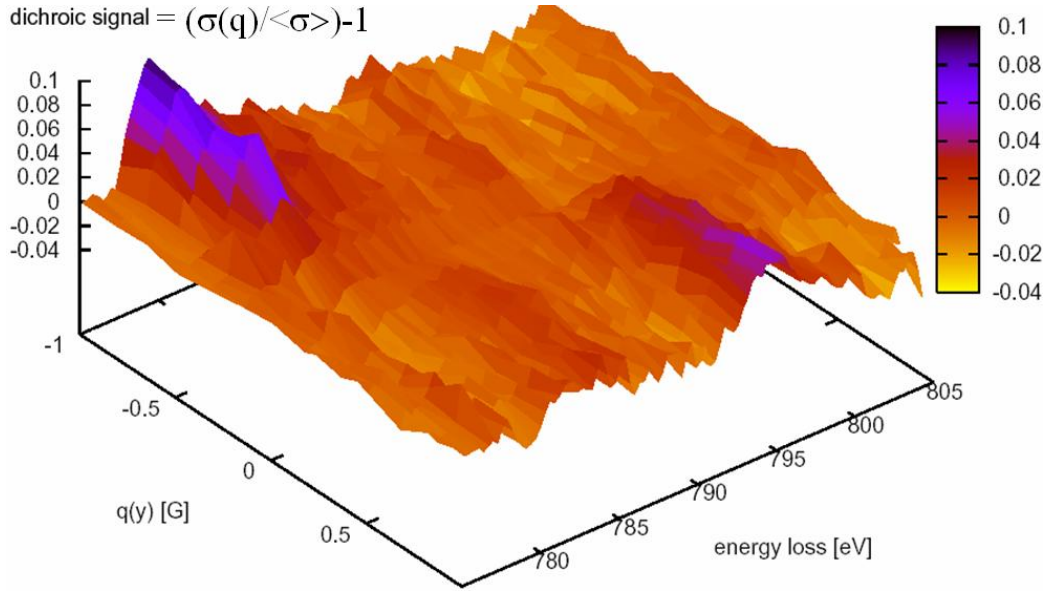

Figure 7.2: Dichroic signal at the Co $L_{2,3}$ edge defined as deviation of $\sigma(q)$ from the average spectrum. The lack of antisymmetry at L_3 and L_2 is obvious when compared with fig. 6.12, which can be obtained by subtracting each $\sigma(q)$ from $\sigma(-q)$ and integrating over the same q_x and E (5.1 eV range around the L_3 edge). Courtesy of Michael Stöger-Pollach.

However eq. 5.30 does not take into account that there are more than just two beams in the crystal. When a more general calculation of the edges is performed including 8-10 beams the results in fig. 7.3 are obtained. From these simulations it can be seen that the spectrum obtained from the DFF contributions only is always different from $< \sigma >$. This is not unexpected, as the real part of the MDFF also contributes to $< \sigma >$. Even when q_z is negligible, the real part of the MDFF at the symmetric (+ and -) positions on the Thales circle does not go to zero because the wave vector transfers associated to the other reflections are not perpendicular to each other (for example the $\vec{q}_{2G}$ corresponding to the $2\vec{G}$ reflection is not perpendicular to any other $\vec{q}_{nG}$). This might explain the behavior observed in fig. 7.2, but requires a more detailed study.

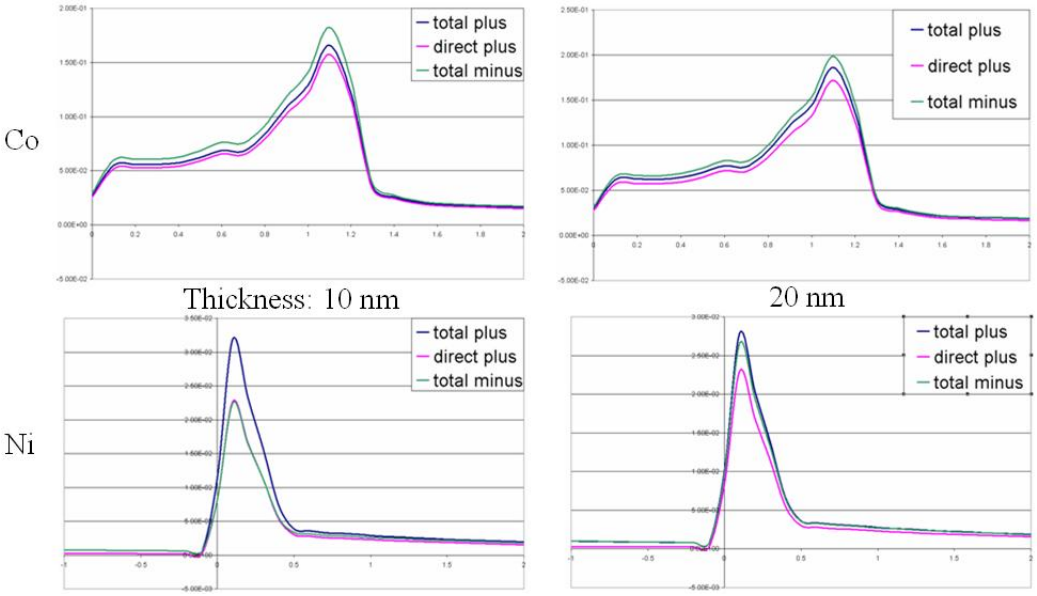

Figure 7.3: Simulation of the Co (above) and Ni (below) L_3 edges for two different values of the thickness: 10 nm (left) and 20 nm (right). The code developed as extension of WIEN2k and described in chapter 5 is able to perform a separate calculation of the contributions to the DDSCS coming from all terms (here labeled total plus for σ^+ and total minus for σ^-) or only from the DFF (labeled direct plus, which is equal to direct minus).

The ESD technique is quite sensitive to the experimental conditions due to the long acquisition time involved. Besides the usual problem related to specimen drift (which in principle should not affect the diffraction pattern but could change the LCC during the measurement if the specimen is bent, thus changing the helicity of the excitation) and beam drift (if the beam tilt drifts, so will the spots in the diffraction pattern), particular care has to be taken in correcting the isochromaticity of the CCD camera. The normal post-acquisition correction procedure of using the cross-correlation to shift every image of the series so that, for example, the maxima of intensity have the same x,y coordinates, may be actually partially removing the dichroic effect: this can be understood if one realizes that the dichroic effect is antisymmetric in q_y and has opposite signs for L_2 and L_3. In the diffraction pattern, the maxima of intensity correspond to the Bragg spot, which have a Lorentzian shape, symmetric with respect to q_y. When the antisymmetric dichroic signature at L_3 is superimposed to the Lorentzian, the resulting function has a maximum for a certain $\tilde{q_{y,3}} \neq 0$. When the same is done at L_2 the dichroic signature will have a different sign and the maxima will now move in the opposite direction, occurring at a $\tilde{q_{y,2}} \approx -\tilde{q_{y,3}}$. An isochromaticity correction script that does not take this into account will most likely overcompensate and reduce the dichroic signal. Also, in the post acquisition data analysis, the positioning of the mirror line defined by the systematic row can have a large influence on the results (this holds true also when acquiring a q-E diagram). In this case the difficulty comes from the fact that the Bragg spots are not point-like thus causing a certain indetermination in their exact position.

7.3 Energy spectroscopic imaging

For ESI it is an image of the sample that is projected onto the SEA and then an energy filtered series is started. It should be noted that in this case the OA is needed to select k_f (fig. 7.4). By using the sum rules (see paragraph 7.1) it can be shown that when the orbital contribution to the total magnetization is negligible with respect to the spin contribution, then the difference of the spectral intensity integrated over the L_3 edge is the opposite of the difference of spectral intensity integrated over the L_2 edge (from eq. 7.2 by assuming $< L_z >= 0$), that is:

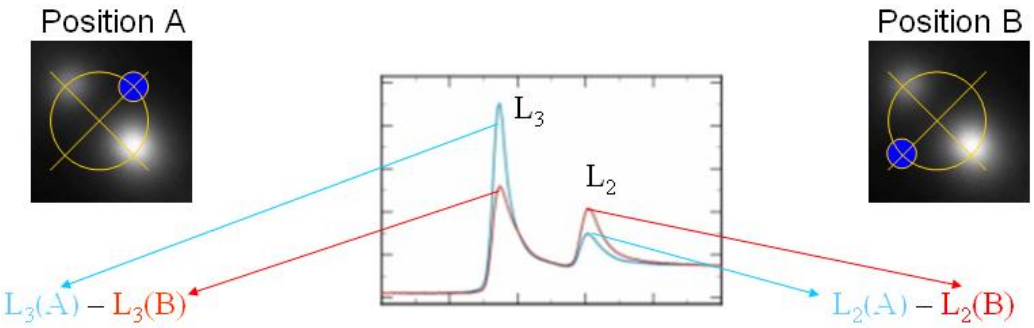

Figure 7.4: Scheme of ESI measurements: the OA is placed on the A position on the Thales circle, the TEM is switched to image mode and an EFS is acquired scanning the $L_{2,3}$ of the element of interest. The OA is then shifted to the B position and another EFS is taken over the same energy range. Under particular conditions (see text) the difference between the integrated spectral intensity at L_3 should be the opposite than at L_2.

$$\int L_3(A) - \int L_3(B) = -\left\{ \int L_2(A) - \int L_2(B) \right\}. \tag{7.4}$$

If the illuminated area is uniform in thickness and is not bend, then the two difference images should have the same value for every pixel. If the illuminated area has, for example, a variation in thickness, thickness fringes will appear in the dark field image and in the difference images (one difference image being like a negative for the other difference image).

Of the techniques that have been ideated so far by use of the intrinsic way, only ESI has failed to yield any significant EMCD effect. The several attempts made have been successful only in proving that a CCD camera with improved dark count reduction might have enough sensitivity to detect spatial changes in the L_3 to L_2 ratio induced by EMCD. The signal is very faint and acquisition times in the order of the minutes are required. The dark count of the CCD camera decrease exponentially with a characteristic half time of the order of tens of minutes. One ESI series lasts long enough for the dark count correction to become significantly larger than the dark count, leaving a characteristic image on the CCD, superimposed to the measurements.

7.4 *In situ* inversion of the magnetization

In the beginning of the previous chapter it was said that in order to reverse the magnetization of the sample it would be necessary to reverse the magnetic field of the lens itself. According to the theory of magnetic electron lenses, the focusing effect of the lens is due to the gradient of the magnetic field generated, therefore the focal distance of the lens will not change if the direction of the magnetic field is reversed. However, every magnetic lens rotates the image by an amount that depends on the direction and strength of the lens current. A current reversal will therefore lead to a rotation of the image with respect to the case of normal current flow. In addition to this, the magnetic field of the objective lens system affects, and is affected by, the other lenses in the TEM by mean of their stray fields. This results in the need for a separate alignment of the TEM in reversed mode. Parameters like eucentric height, illumination, focus and specimen area are likely to change, even if only slightly, if the current is reversed without realigning the TEM. However in most cases it is possible to save the two alignments in the TEM registry and recall them at will.

A special switching unit was built [102] and inserted on the power line to the objective lens, between the TEM power supply and the column, as it is otherwise not possible to reverse the lens current in most of the commercially available TEMs. The unit allows for the safe reversal of the current in the lens, changing only its sign. To ensure that the current commutation is fully reversible and to make sure that no unwanted hysteresis effects can influence the measurements, the magnetic field at the specimen's location was measured. A special holder with a Hall sensor was used to monitor the magnetic field from an objective lens excitation of 100% to -100% and back to 100%. Within the metering precision of the Hall sensor, no hysteresis was detectable. Therefore, no deterioration of imaging performance is expected after a commutation cycle. High-resolution images of a graphite lattice have confirmed [102] the effectiveness of the unit and, above all, that the performance of the TEM in reversed mode is not affected.

Once the unit was installed in Vienna, an EMCD measurement was performed (fig. 7.5). A first spectrum is taken; then the current in the objective lens is reversed, causing a realignment of the magnetic moments along the opposite direction. A second spectrum is taken without otherwise altering any other parameter (within the limits of precision of the TEM alignments in the normal and reverse mode). The MDFF-containing term would thus

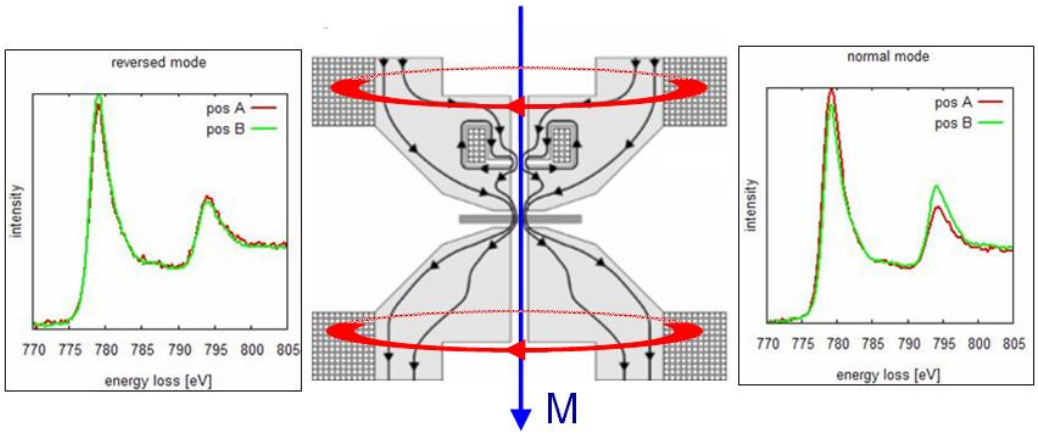

Figure 7.5: Cross section through the objective lens system of a FEI microscope showing how the lens current (red) produces a strong magnetic field that forces the sample magnetization $\vec{M}$ along the TEM optical axis. EMCD measurements taken when the current is reversed (left) shown an opposite sign for the dichroic signal in the normal mode (right). The difference in the intensity of the dichroism (smaller in the reversed mode) can be attributed to imperfections in the alignment which, in turn, may induce a small change in the chirality of the excitation if, for example, the LCC is changed to a less favorable value. Figure from Ref. [102].

change sign (eqs. 5.30 and 5.31) and the difference of the two EELS spectra so obtained is the dichroic signal for opposite helicities. This is a direct experimental proof of the magnetic origin of EMCD.

7.5 Biprism

When the specimen does not have sufficiently big crystal grains, all the previously described methods for EMCD measurements cannot be used. An alternative would be to use another device, such as an electron biprism, as beam splitter. The electron biprism is a thin conductor wire (typically < 1 μm in cross section) placed in the optical axis, perpendicular to the electron beam. When charged, the electric field around the filament deflects the electron waves, so that they interfere below the biprism in a region of width w. The spacing s of the interference fringes depends on the biprism voltage and commonly ranges from 1 to 100 nm. The fringes can be projected on the sample if the biprism is mounted, for example, in the condenser aperture (fig. 7.6. The areas illuminated by white (black) fringes correspond to a phase shift between the two plane waves of zero (π). In the condenser mounting the biprism appears to be thinning rapidly with use, probably because of the high intensity of the electron beam; moreover charging effects are enhanced, with consequent instability of the fringes.

The effect in the diffraction plane introduced by the biprism is to create a superposition of the electron scattering angular distribution of the two plane waves. For example in a crystalline specimen this will result in the appearance of two diffraction patterns superimposed on top of each other and shifted by an angular distance equal to s^{-1}. In any case, the two plane waves created by the biprism will produce two 000 spots in the diffraction plane. An aperture (either the OA or the SEA) can be used to select $\vec{q} \perp \vec{q'}$ and any of the configurations previously described can be adapted. Change of chirality can be obtained by either shift of the k_f-selecting aperture in the diffraction plane or by shifting the projection of the fringes with respect to the sample by half the fringe spacing.

Two possible configurations could be used. In the first one, the fringes have the same spacing s than the atoms in the sample (fig 7.7), so that the phase shift between the two incident waves is the same for every atom. However this is possible only in crystalline specimens and, in such case, the Bragg spots could interfere with the detection of EMCD by producing a

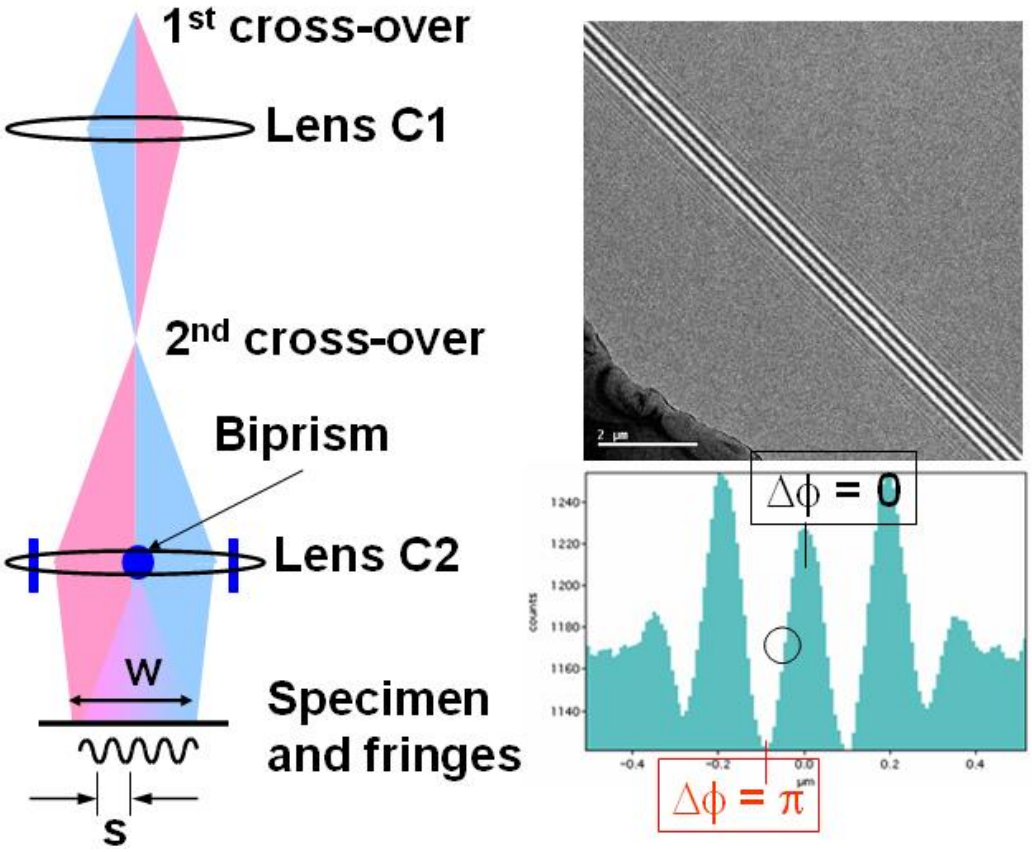

Figure 7.6: **Left**: schematic representation of a condenser mounting of the electron biprism. When the biprism is charged, the electron wave is split into two halves which interfere on the image plane constructively (white fringes) or destructively, according to the difference in the optical path. **Right**: micrograph of fringes (above) and their line profile (below), showing the phase relation between the two incident waves. The circle indicates where the phase shift is $\pi/2$ (repeated for every fringe).

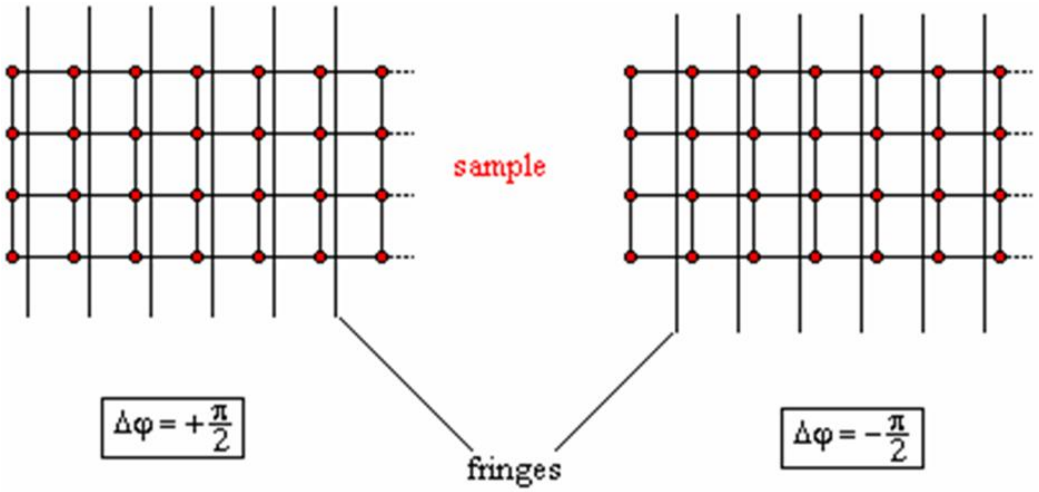

Figure 7.7: Possible EMCD biprism setup. If the fringe spacing is the same as the atomic distance the phase shift between the incident waves will be the same for every atom (red dots). Shifting the fringes provides an alternative way to change the phase shift (besides moving the k_f-selecting aperture).

chiral effect in much the same way described in the intrinsic method.

Another possibility is to use a very large fringe spacing (fig 7.8) and then select a region on the specimen using the SAA, so that the phase shift within the selected area does not change by more than $\pi/2$. But since the smallest SAAs have a projected radius of 50-100 nm, this requires that the fringe spacing $s \geq 500$ nm because if the diameter of the SAA is bigger than a quarter of the s the phase in the area selected changes by more than $\pi/2$. Such big fringe spacings have not yet been achieved. Moreover, even if it were possible to obtain them, the wave vector transfer $\vec{q_\perp}$ in the diffraction plane that could be obtained would be of the order of s^{-1} which, in this case, would be much smaller than the q_z due to the energy lost by the electron because of the ionization process (see fig. 7.9). This means that the non-dichroic term in eq. 5.30 is much bigger than the one responsible for the EMCD. It is very likely that in this case the difference induced by the dichroism would be submerged by the Poissonian noise of the non-dichroic term.

The use of convergent beam techniques is not possible with a biprism, as deviations from parallel illumination greatly reduce the fringe contrast (but an elliptical illumination, with a major axis perpendicular to the biprism can

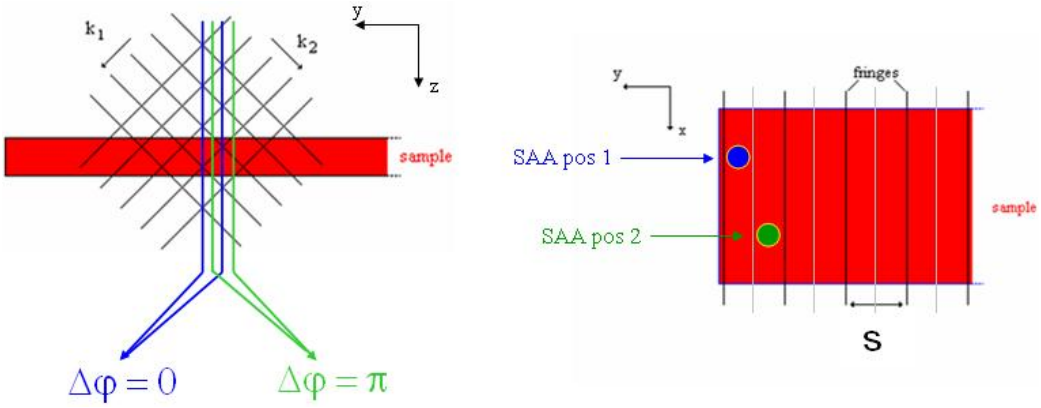

Figure 7.8: **Left**: the two incident plane waves interfere forming (virtual) planes with the same phase difference (blue for $\Delta\phi = 0$, *i.e.* constructive interference and green for $\Delta\phi = \pi$, *i.e.* destructive interference. **Right**: a SAA with radius $r \leq \frac{s}{8}$ can be used to select an area on the sample where the two incident plane waves have a phase difference of $\approx \pi/2$. Again, an alternative way to change the helicity is to move the fringes with respect to the sample by, for example, tilting the incoming beam or moving the SAA.

be used and is routinely used in electron holography).

To conclude this paragraph, the EMCD biprism way seems flawed both theoretically and technically, however it is too much of an unexplored field to hold this statement as the final word on the subject.

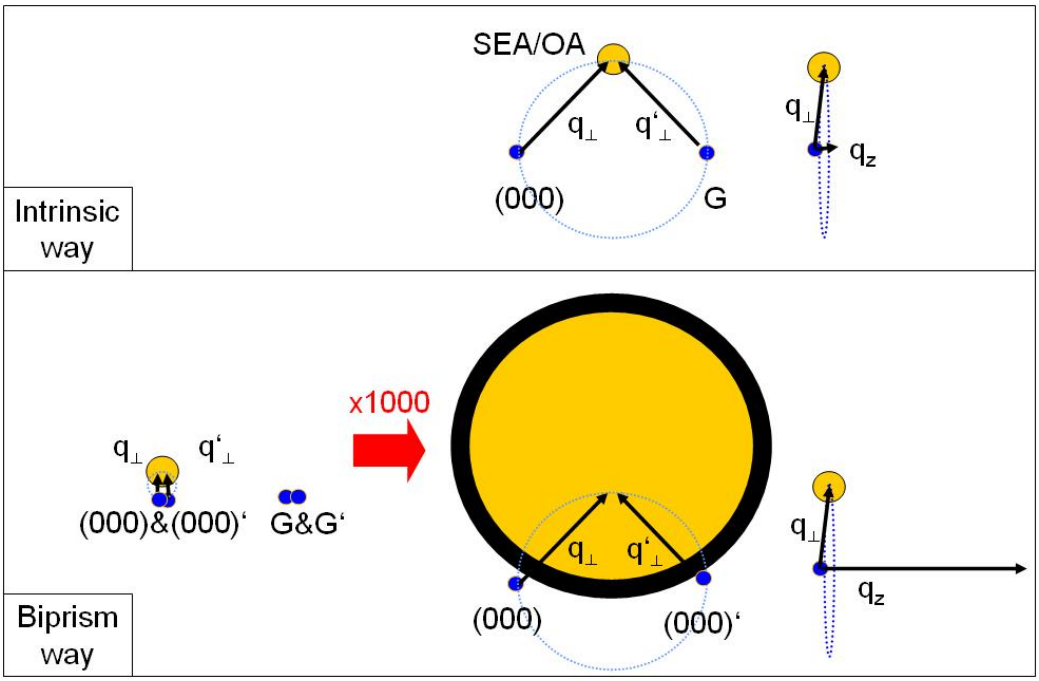

Figure 7.9: Comparison between the wave vector transfers ($\vec{q}$ and $\vec{q'}$) in the intrinsic way and in the biprism way with an hypothetic $s = 500$ nm. In both cases $q_\perp$ is of the same order of magnitude than the angular distance between the incident plane waves, whereas q_z is determined by the energy lost because of the ionization process (for $L_{2,3}$ of $3d$ metals, this is 0.01-0.02 nm^{-1}). For simple crystal $q_\perp$ is then ≈ 0.1 nm^{-1}, which means that for the intrinsic way q_z is one order of magnitude smaller than $q_\perp$ and can be neglected (see also paragraph 5.5 and fig. 5.6); for fringe spacings of 500 nm $q_\perp \approx 0.002$ nm^{-1}.

Chapter 8

Conclusions

In this thesis a detailed presentation of the novel phenomenon called Energy-loss Magnetic Chiral Dichroism is given. The origins from its x-ray counterpart were described, the theoretical framework was derived from the first principles of quantum mechanics and dynamical diffraction theory and an overview of several methods and procedures was illustrated together with experimental results and applications.

It could be helpful also to compare the timetable of the development of XMCD and EMCD up to now (see table 8). The theoretical prediction that circular magnetic dichroism could be observed by using circularly polarized x-ray photons was made by Erskine and Stern in 1975 [103]. The first experimental observation of the predicted effect was reported twelve years later by G. Schütz [5] studying the XMCD effect on K edge of Fe. The sum rules, necessary to extract the information about the magnetic moment of the specimen, were derived about five years later [23, 49]. The experimental confirmation of the validity of the sum rules followed shortly thereafter [24]. In the case of the EMCD the theoretical prediction was published in 2003 [1], followed the same year by the first chiral TEM measurement [2] and the definitive experimental confirmation of the effect was made known less than three years later [3]. The sum rules for EMCD [96, 97] were then presented in 2007.

It has been demonstrated how all methods have advantages and disadvantages such that it is not possible to dismiss *a priori* one or the other, but the choice should be made depending on the kind of specimen investigated.

The detector shift method is easy to set up but has a limited lateral resolution and part of the signal is lost due to the SAA, unless the CBED

Table 8.1: Chronology of the milestones in XMCD and EMCD.

Milestone	Year	Author(s)
Theory of XMCD	1975	Erskine, Stern
Simulation of XMLD	1985	Thole, van der Laan, Sawatzky
First experiment of XMLD	1986	van der Laan
First experiment of XMCD	1987	Schütz *et al.*
Large XMCD effect	1990	Chen
Sum rules for $< S >$	1992	Thole *et al.*
Sum rules for $< L >$	1993	Carra *et al.*
Experiment on sum rules	1995	Chen *et al.*

Milestone	Year	Author(s)
Equivalence XMLD-EMLD	1993	Hitchcock
Exp. equivalence XMLD-EMLD	1997	Yuan, Menon
Proposal of EMCD	2003	Hébert, Schattschneider
First experiment of XMCD	2003	Rubino *et al.*
Exp. equivalence XMCD-EMCD	2006	Schattschneider *et al.*
Large EMCD effect	2007	Schattschneider *et al.*
Sum rules for EMCD	2007	Rusz *et al.*, Calmels *et al.*

configuration is used. The OA shift method has a better lateral resolution but again part of the signal is lost and the momentum transfer selection lacks precision. The LACDIF method has a better collection efficiency as none of the electrons which hit the sample are filtered out in the image plane, but it is more difficult to configure. The q-E diagram allows parallel measurements of opposite helicities in a single acquisition, but limits to particular values the position and size of the SEA, which may hinder the optimization of the signal-to-noise ratio. Energy filtering techniques such as ESD may be used to record an EELS data cube. The advantage of this method lies in the possibility of recording all the information and post processing it to obtain the best SNR. This makes it easy to use even non-standard, virtual SEAs to integrate the dichroic signal with a numerical post processing [88]. The effect of non-isochromaticity, beam and specimen drift are however enhanced as this method disperses the available signal over many more pixels than the spectroscopic method. For this reason a detector with low noise and low and stable dark count rates is a necessity. Filtered imaging can be envisaged in image mode, using an objective aperture (similarly to the OA shift method) to select the correct momentum transfer in the diffraction pattern and obtaining a chirally active illumination. Again, drift, detector background and non-isochromaticity makes this method difficult to set up, but the possible attainable lateral resolution is promising.

The techniques illustrated here show that it is possible to routinely measure MCD in the TEM with a spatial resolution of 10 nm or better using several complementary methods. Recently it was also demonstrated [96, 97] that EMCD sum rules can be applied to derive the spin and orbital contributions to the magnetization of the sample, or at least their ratio, since absolute values are difficult to obtain due to the EMCD dependence on the tilt and thickness of the crystal (see paragraph 7.1).

The two main limitations of the intrinsic EMCD experiments are:

a) the area of interest needs to be a single crystal (with a radius as small as a few nm) which can be oriented in a two- or three-beam configuration; however a scan across an interface or a border of a magnetic nanoparticle would still provide valuable information, at least up to a region where the crystal lattice is not too distorted;

b) the magnetic field of the TEM lenses at the specimen location (1-2 Tesla) is high enough to saturate most of the magnetic samples along the TEM optical axis. Saturation could be avoided by developing a Lorentz-like mode for EMCD, where the objective lens is deactivated. This could be

useful in, for example, the study of magnetic domains.

With C_s correctors EMCD could in principle be applied with nm or sub-nm resolution. Contrary to PEEM, it will not be restricted to the study of ultrathin surface layers. Thus it will be possible to study the magnetic properties at interfaces, a question of utmost importance for spintronic devices. With the additional capacity of the electron microscope for chemical, electronic, morphological and crystallographic investigations, EMCD in the TEM can become a powerful complement or competitor of traditional or new [30] XMCD techniques. Applications are still hampered by technical problems related to beam and specimen drift, to the ultimate accuracy of tuning the phase shift, and to a more complicated interpretation of results than is possible with XMCD.

With better spatial resolution and depth sensitivity than XMCD, EMCD can be a very powerful investigation tool. The need for high spatial resolution is evident in view of the small dimensions of electronic devices. Examples come also from organic chemistry and zoology. They range from magnetic read-write heads based on the giant magnetoresistance effect, over perpendicular magnetic recording, spin valve or magnetic tunneling transistors, magnetic nanoparticles, enzymes containing Ni to magnetotactic bacteria.

Actual questions in spintronics relate to the existence of magnetic dead layers at interfaces posing a barrier for successful spin injection in spin transistors, interlayer coupling in magnetic multilayers, FM-AFM pinning, the determination and localization of magnetic moments in dilute magnetic semiconductors or Heusler alloys, or phase separation in highly correlated electron system.

For the simulation of the EMCD effect in EELS a computer code package was developed by including the theory of dynamical Bragg diffraction in a pre-existing band structure code (WIEN2k). This extension was used to successfully predict the behavior of EMCD in different TEM setups and to demonstrate the relation of the dichroic peak shape to the difference of d-projections of the spin-resolved density of states in analogy with similar observation for XMCD.

Using this code the validity of the dipole approximation, often assumed, was tested. It was found that for the $3d$ ferromagnetic systems studied it is a reasonable approximation, however with wrong asymptotic properties - it overestimates the contributions from larger $\vec{q}$-vectors. A very accurate approximation for the studied systems is the $\lambda = \lambda' = 1$ approximation, which treats appropriately the dominant $p \rightarrow d$ dipole transitions and remains very

accurate also for large q, q'.

In order to provide guidance to the experiments the dichroic signal was simulated as a function of the sample thickness, LCC, acceleration voltage and detector placement. While the dichroic signal strength is rather robust with respect to the precision of the detector placement, the thickness of the specimen influences the signal considerably. Therefore it might be a challenge to produce samples with optimum thickness and selecting the best systematic row Bragg spot.

Using this program the experimental conditions have been optimized with respect to the position and size of the $\vec{q}$-selecting aperture. As a general trend, increasing the circular aperture radius for EMCD experiments leads to a strong increase in SNR. More optimal aperture shapes are possible but impractical since they depend on the exact conditions of the sample and have far too complex shapes. The suboptimal circular aperture however still performs quite well and is readily available in any microscope. As a rule of thumb, the aperture can be put near a strongly excited diffraction spot avoiding the crossing of the line connecting that diffraction spot with the (0,0,0) spot. Dynamical simulations can help optimize the position and size further for specific cases. It should be noted that an increase of SNR of a factor f_N would require an increase in current or exposure time by approximately a factor f_N^2. Larger aperture size might even give stronger improvements and the dynamic simulations showed that radii of about one reciprocal distance G are close to optimal. This size is larger than what was previously used in experiments and shows that significant improvements are possible. Based on the indication given, simple experiments recording two EELS spectra in symmetric positions in the diffraction pattern with a rather large collection angle are far more easy and sufficient.

Moreover the utility of this code is not restricted to EMCD: any TEM technique were dynamical diffraction effects could influence the ELNES (for example ELCE) can benefit greatly from its predicting powers.

Table 8.2: Overview of MCD techniques and their most important attributes (best or typical values are given). The EMCD ones marked by * refer to values obtained by the CEMES group in Toulouse with a better spectrometer coupled with a C_s corrector. The values for the q-E diagram depend on the illumination technique, but the acquisition time is halved and the intensity is lower because different helicities are acquired simultaneously.

Technique	Spatial resolution	Energy resolution	Collection time	Intensity (S/N)
EMCD (tilt series)	200 nm	1-2 eV	1-5 min	low
EMCD (det. shift)	200 nm	1-2 eV	1-5 min	accept.
EMCD (OA shift)	50 nm	1-2 eV	1-5 min	low
EMCD (q-E diagram)	depends	depends	half	lower
EMCD (LACDIF)	5-10 nm	0.7 eV	10 sec	good
EMCD (CBED)	1-5 nm	0.7 eV	10 sec	accept.
EMCD (ESD*)	50 nm	1 eV	30 min	accept.
XMCD (PEEM)	50 nm	0.1 eV	15 min	high
XMCD (XAS)	15 nm	0.1 eV	30 min	high

Chapter 9

Appendix: script for detector shift

The following is the code of the script used in diffraction mode for the exact positioning of the SEA with respect to the diffraction pattern in a FEI TEM. It was originally developed by Nestor J. Zaluzec and further tested and modified by Jo Verbeeck and Cécile Hébert.

Nestor J. Zaluzec, Argonne National Laboratory, Electron Microscopy Center, Argonne, Illinois 60439 USA. Email: Zaluzec@aaem.amc.anl.gov

Johan Verbeeck, University of Antwerp, EMAT (Electron microscopy for materials science), Groenenborgerlaan 171, B-2020 Antwerp, Belgium. Email: jo.verbeeck@ua.ac.be

Cécile Hébert, Ecole Polytechnique Fédérale de Lausanne, SB CIME-GE, MXC 132 (Bâtiment MXC) Station 12, CH-1015 Lausanne. Email: cecile.hebert@epfl.ch

```
<html>

<title>HARECES Chiral SHIFT Experiment 20070403</title>

<body bgcolor="#fff8dc">

<form name="form1">
<center>
<B><FONT SIZE=4>HARECES-Chiral Diffraction SHIFT </B></FONT><br>
Version NJZ 20070403_jo_ch by Nestor J. Zaluzec, Jo Verbeeck,
```

```
Cecile Hebert<hr>
Must be using MSIE to run on the TecnaiF20 System<br>

<hr>

<table border=1>

<tr>
<td valign=top>
<center>
<B><FONT SIZE=4>DP Location</B></FONT><br>
<hr>

<table>
<tr><td colspan=2 bgcolor=lightblue><center>
Current Beam Location</td></tr>
<tr><td><center>
<hr>
X Position  = <input type="text" size=20 name="currentx" ><br>
Y Position  = <input type="text" size=20 name="currenty" >
<hr>
Target X(g) = <input type="text" size=20 name="Targetx" ><br>
Target Y(g) = <input type="text" size=20 name="Targety" >

</td>
</tr>
</table>
<br>
</form>




</td>
<td valign=top>
<form name="form2">
<center>
<B><FONT SIZE=4>Calibration Points</B></FONT><br>
```

```
<hr>



<table>
<tr><td colspan=2 bgcolor=lightblue><center>
Define the Calibration Points</td></tr>
<tr><td><000> DP Shift X (deg):
</td><td><input type="text" size=5 name="initialx"  ></td></tr>
<tr><td><000> DP Shift Y (deg):
</td><td> <input type="text" size=5 name="initialy" ></td></tr>
<tr><td>< g > DP Shift X (deg):
</td><td><input type="text" size=5 name="finalx" ></td></tr>
<tr><td>< g > DP ShiftY (deg):
</td><td><input type="text" size=5 name="finaly" ></td></tr>
</table>
</center>



</td>
</tr>
<tr><td colspan=3>
<center>
Move to Calibration Points<br>
<hr>
<input type="button" value="<Chiral
+> " onclick="MovetoChiral1()" >   <br><br>
<input type="button" value="<000>"
onclick="MovetoStart()" >   
<input type="button" value="<g/2>"
onclick="MovetoMid()" >   
<input type="button" value="< g >"
onclick="MovetoEnd()" >   <br><br>
<input type="button" value="<Chiral -> "
onclick="MovetoChiral2()" >   
<hr>
<input type="button" value="get <000>"
```

```
onclick="GetStart()" >   
<input type="button" value="get < g >"
onclick="GetEnd()" >   <br><br>
<hr>
<input type="button" value="Zero "
onclick="MovetoZero()" >   
<input type="button" value="To Target "
onclick="MovetoTarget()" ><br>
</center>
</td></tr>
</table>
</form>

<table><tr><td>
<ul>
<li>Shifting is in degrees. To get approximate values Use
 DF Tilts (a nominal correction internal is made)<br>
<li>Remember to set the Series Size = TotalPts
in ESVision Acquire Series Size EDX Menu<br>

<li> Use Gatan Software to Collect Individual Spectra.
 NOT ESVision
<li>Last Updated: Dec 20 2006
</ul>
</td></tr></table>

<hr>

<center>
</center>
</center>



<script language="javascript">

<!--
```

```
var i=0;
var j=0;
var timerID;

// these are Tecnai objects

var mytecnai=new ActiveXObject("Tecnai.Instrument");
var myilum=mytecnai.illumination;
var mytilt=myilum.tilt;
var myblank=myilum.BeamBlanked;
var myproj=mytecnai.projection;
var myshift=myproj.DiffractionShift;



function MovetoStart(){

//  Move to 000

// degrees to radians

var ix=document.form2.initialx.value/(57.29583);
var iy=document.form2.initialy.value/(57.29583);
var fxx=document.form2.finalx.value/(57.29583);
var fyy=document.form2.finaly.value/(57.29583);
var x,y,xx,yy,xc, yc, Lx, Ly, Px, Py;

// scan center point in microscope coordinates

xc= ix + (fxx-ix)/2;
yc= iy + (fyy-iy)/2;
```

```
//

x = ix;
y = iy;
xx= fxx;
yy= fyy;



myshift.X = x;
myshift.Y = y;
myproj.DiffractionShift=myshift;

document.form1.currentx.value=x*(57.29583);
  document.form1.currenty.value=y*(57.29583);

}

function MovetoMid(){

//  Move to the mid position between 000 and G

// degrees to radians

var ix=document.form2.initialx.value/(57.29583);
var iy=document.form2.initialy.value/(57.29583);
var fxx=document.form2.finalx.value/(57.29583);
var fyy=document.form2.finaly.value/(57.29583);
var x,y,xx,yy,xc, yc, Lx, Ly, Px, Py;


// scan center point in microscope coordinates

xc= (ix + (fxx-ix)/2);
yc= (iy + (fyy-iy)/2);
```

```
myshift.X = xc;
myshift.Y = yc;
myproj.DiffractionShift=myshift;

document.form1.currentx.value=xc*(57.29583);
document.form1.currenty.value=yc*(57.29583);

}

function MovetoEnd(){

// Move to G

// degrees to radians

var ix=document.form2.initialx.value/(57.29583);
var iy=document.form2.initialy.value/(57.29583);
var fxx=document.form2.finalx.value/(57.29583);
var fyy=document.form2.finaly.value/(57.29583);
var x,y,xx,yy,xc, yc, Lx, Ly, Px, Py;


// scan center point in microscope coordinates

xc= ix + (fxx-ix)/2;
yc= iy + (fyy-iy)/2;



x = ix;
y = iy;
xx= fxx;
yy= fyy;
```

```
myshift.X = xx;
myshift.Y = yy;
myproj.DiffractionShift=myshift;

document.form1.currentx.value=xx*(57.29583);
document.form1.currenty.value=yy*(57.29583);
}

function GetEnd(){
myshift=myproj.DiffractionShift;
document.form2.finalx.value=myshift.X*(57.29583);
document.form2.finaly.value=myshift.Y*(57.29583);
document.form1.currentx.value=myshift.X*(57.29583);
document.form1.currenty.value=myshift.Y*(57.29583);

}

function GetStart(){
myshift=myproj.DiffractionShift;
document.form2.initialx.value=myshift.X*(57.29583);
document.form2.initialy.value=myshift.Y*(57.29583);
document.form1.currentx.value=myshift.X*(57.29583);
document.form1.currenty.value=myshift.Y*(57.29583);
}




function MovetoChiral1(){

// Move to the Chiral + position as defined in Vienna
//
//  X C+
//
//
//
// X 000 X G
```

```
// degrees to radians

var ix=document.form2.initialx.value/(57.29583);
var iy=document.form2.initialy.value/(57.29583);
var fxx=document.form2.finalx.value/(57.29583);
var fyy=document.form2.finaly.value/(57.29583);
var Mx=0.5;
var My=0.5;
var x,y,xx,yy,xc1,yc1, Theta,  L,dx,dy;



dx = fxx-ix;
dy = fyy-iy;


L = Math.sqrt( dx*dx + dy*dy );

if (dy >= 0) { Theta=Math.acos(dx/L);}
else {Theta=6.283-Math.acos(dx/L);}


//document.write ("<br>  dx= ", dx ," dy= ",
dy,"<br>", "  Theta=", Theta, "<br>");


//Rotation and translation

xc1= ix + L*(Mx*Math.cos(Theta)-My*Math.sin(Theta));
yc1= iy + L*(Mx*Math.sin(Theta)+My*Math.cos(Theta));


x = ix;
y = iy;
xx= fxx;
yy= fyy;
```

```
myshift.X = xc1;
myshift.Y = yc1;
myproj.DiffractionShift=myshift;

document.form1.currentx.value=xc1*(57.29583);
document.form1.currenty.value=yc1*(57.29583);
}


function MovetoTarget(){

// Move the beam to a position given by
"Target Position" in units of G

// degrees to radians

var ix=document.form2.initialx.value/(57.29583);
var iy=document.form2.initialy.value/(57.29583);
var fxx=document.form2.finalx.value/(57.29583);
var fyy=document.form2.finaly.value/(57.29583);
var Mx=document.form1.Targetx.value;
var My=document.form1.Targety.value;
var x,y,xx,yy,xc1,yc1, Theta,  L,dx,dy;



dx = fxx-ix;
dy = fyy-iy;


L = Math.sqrt( dx*dx + dy*dy );

if (dy >= 0) { Theta=Math.acos(dx/L);}
else {Theta=6.283-Math.acos(dx/L);}
```

```
//document.write ("<br>  dx= ", dx ," dy= ",
dy,"<br>", "  Theta=", Theta, "<br>");


//Rotation and translation

xc1= ix + L*(Mx*Math.cos(Theta)-My*Math.sin(Theta));
yc1= iy + L*(Mx*Math.sin(Theta)+My*Math.cos(Theta));


x = ix;
y = iy;
xx= fxx;
yy= fyy;


myshift.X = xc1;
myshift.Y = yc1;
myproj.DiffractionShift=myshift;

document.form1.currentx.value=xc1*(57.29583);
document.form1.currenty.value=yc1*(57.29583);
}

function MovetoChiral2(){

// Move the beam to Chiral minus position

// degrees to radians

var ix=document.form2.initialx.value/(57.29583);
var iy=document.form2.initialy.value/(57.29583);
var fxx=document.form2.finalx.value/(57.29583);
var fyy=document.form2.finaly.value/(57.29583);
var Mx=0.5;
var My=-0.5;
var x,y,xx,yy,xc1,yc1, Theta,  L,dx,dy;
```

```
dx = fxx-ix;
dy = fyy-iy;


L = Math.sqrt( dx*dx + dy*dy );

if (dy >= 0) { Theta=Math.acos(dx/L);} else {Theta=6.283-Math.acos(dx/L);}


//document.write ("<br>  dx= ", dx ," dy= ",
dy,"<br>", "  Theta=", Theta, "<br>");


//Rotation and translation

xc1= ix + L*(Mx*Math.cos(Theta)-My*Math.sin(Theta));
yc1= iy + L*(Mx*Math.sin(Theta)+My*Math.cos(Theta));


x = ix;
y = iy;
xx= fxx;
yy= fyy;


myshift.X = xc1;
myshift.Y = yc1;
myproj.DiffractionShift=myshift;

document.form1.currentx.value=xc1*(57.29583);
document.form1.currenty.value=yc1*(57.29583);
}
```

```
function MovetoZero(){

// this function scans the beam in angle
//  at each point it stops and acquires a spectrum
//  which is stored in ESVision memory

// degrees to radians

var ix=document.form2.initialx.value/(57.29583);
var iy=document.form2.initialy.value/(57.29583);
var fxx=document.form2.finalx.value/(57.29583);
var fyy=document.form2.finaly.value/(57.29583);
var x,y,xx,yy,xc,yc;


//reset to zero tilts at the end of the 2D scan


{
myshift.X=0;
myshift.Y=0;
myproj.DiffractionShift=myshift;

document.form1.currentx.value=0;
document.form1.currenty.value=0;
}


}



function stop(){
clearTimeout(timerID);
}
```

```
//-->
</script>

</body>

</html>
```

Acknowledgments

I am grateful to my supervisor, Prof. Peter Schattschneider, for giving me the great opportunity to be part of such an exciting, novel and groundbreaking research, whose results will hopefully grow in number and importance in the years to come. My thanks go to the people with which I have been working closely in the last five years: Aude Montgermont, Eva Karl-Rückert, Vanda Peter, Johannes Bernardi, Peter Pongratz, Tomasz Galek, Dominique Eyidi, Henri Franco, Charlotte Kitzhofer, Jo Verbeeck, Anita Laister and, above all, to Michael Stöger-Pollach and Cécile Hébert.

A special thank to Sabine and Bernhard Schwarz for their help in the making of this thesis and to Nestor J. Zaluzec, Jo Verbeeck and Cécile Hébert for the detector shift script, a very useful tool.

I would like to thank the European Union for funding this new and exciting project (contract nr. 508971 FP6-2003-NEST-A) and the partners that have contributed to the results obtained and have made them possible with their work, their suggestions and their enthusiasm: Ján Rusz, Pavel Novák, Laura Felisari, Francesco Maccherozzi, Elvio Carlino, Giorgio Rossi, Christian Hurm, Josef Zweck, Petr Formanek and Hannes Lichte.

The city of Vienna should also receive my gratitude, for the years of hospitality it had offered to me, the many friends I have been able to meet and that will be sorely missed and for its greatest gift: my wife Lois. She has my thanks, my love and my life, none of them enough to repay the joy she has brought me.

Un ringraziamento particolare va ai miei genitori e a tutti i miei amici e parenti in Italia: voi siete le mie radici, non sarete dimenticati! Dovunque andró sarete sempre con me.

Bibliography

[1] C. Hébert and P. Schattschneider, *A proposal for dichroic experiments in the electron microscope*, Ultramicroscopy **96** (2003) 463.

[2] S. Rubino, C. Hébert and P. Schattschneider, Microscopy Conference Dresden September 07-12 (2003) Late Breaking Poster.

[3] P. Schattschneider, S. Rubino, C. Hébert, J. Rusz, J. Kuneš, P. Novak, E. Carlino, M. Fabrizioli, G. Panaccione and G. Rossi, *Experimental proof of circular magnetic dichroism in the electron microscope*, Nature **441** (2006) 486.

[4] J. Rusz, S. Rubino and P. Schattschneider, *First principles theory of chiral dichroism in electron microscopy applied to 3d ferromagnets*, Physical Review B **75** (2007) 214425.

[5] G. Schütz, W. Wagner, W. Wilhelm, P. Kienle, R. Zeller, R. Frahm and G. Materlik, *Absorption of circularly polarized X-rays in iron*, Physical Review Letters **58** (1987) 737.

[6] E. Abbe, *Beiträge zur Theorie des Mikroskops und der mikroskopischen Wahrnehmung*, Arch. mikrosk. Anat. Entwichlungsmech. **9** (1873) 413.

[7] L. Rayleigh, *On the diffraction of object glasses*, Monthly Notes of the Royal Astronomical Society **33** (1872) 59.

[8] P. Kirkpatrick and A. V. Baez, *Formation of optical images by x-rays*, J. Opt. Soc. Am. **38** (1948) 766.

[9] D. H. Kim, P. Fischer, W. Chao, E. Anderson, M. Y. Im, S. C. Shin and S. B. Choe, *Magnetic soft x-ray microscopy at 15 nm resolution probing nanoscale local magnetic hysteresis*, Journal of Applied Physics **99** (2006) 08H303.

[10] M. Knoll and E. Ruska, *Das Elektronenmikroskop*, Zeitschrift für Physik **78** (1932) 318.

[11] C. Davisson and L. H. Germer, *Diffraction of Electrons by a Crystal of Nickel*, Physical Review **30** (1929) 705.

[12] L. V. P. R. de Broglie, Recherches sur la théorie des quanta, Ph.D. thesis, Paris University, Paris (1924).

[13] O. Scherzer, *Über einige Fehler von Elektronenlinsen*, Zeitschrift für Physik **101** (1936) 593.

[14] H. Rose, *Abbildungseigenschaften sphärisch korrigierter elektronenoptischer Achromate*, Optik **33** (1971) 1.

[15] D. B. Williams and C. B. Carter, Transmission electron microscopy: a textbook for materials science (Plenum Press, New York, 1996).

[16] M. van der Stam, M. Stekelenburg, B. Freitag, D. Hubert and J. Ringnalda, *A new aberration-corrected transmission electron microscope for a new era*, Microscopy and Analysis **19(4)** (2005) 9.

[17] C. Bai, Scanning tunneling microscopy and its applications (Springer Verlag, New York, 1999).

[18] P. Schattschneider, C. Hébert and S. Rubino, *Circular Dichroism in the Transmission Electron Microscope*, in *Encyclopedia of Materials: Science and Technology*, edited by K. H. J. Buschow, R. W. Cahn, M. Flemings, P. Veyssiere, E. Kramer and S. Mahajan (Elsevier doi:10.1016/B978-008043152-9/02173-4, Oxford, 2001) 1–11.

[19] L. Pasteur, Ann. Chim. Phys. III **24** (1848) 442.

[20] T. Verbiest, M. Kauranen, Y. V. Rompaey and A. Persoons, *Optical Activity of Anisotropic Achiral Surfaces*, Physical Review Letters **77** (1996) 1456.

[21] L. D. Landau and E. M. Lifschitz, Course of Theoretical Physics, vol. 8, Electrodynamics of Continuous Media (Akademie Verlag, Berlin, 1985).

[22] C. T. Chen, F. Sette, Y. Ma and S. Modesti, *Soft-x-ray magnetic circular dichroism at the $L_{2,3}$ edges of nickel*, Physical Review B **42** (1990) 7262.

[23] B. T. Thole, P. Carra, F. Sette and G. vander Laan, *X-ray circular dichroism as a probe of orbital magnetization*, Physical Review Letters **68** (1992) 1943.

[24] C. T. Chen, Y. U. Idzerda, H.-J. Lin, N. V. Smith, G. Meigs, E. Chaban, G. H. Ho, E. Pellegrin and F. Sette, *Experimental Confirmation of the X-Ray Magnetic Circular Dichroism Sum Rules for Iron and Cobalt*, Physical Review Letters **75** (1995) 152.

[25] S. W. Lovesey and S. P. Collins, X-Ray Scattering and Absorption by magnetic Materials (Clarendon Press, Oxford, UK, 1996).

[26] J. Goulon, C. Goulon-Ginet, A. Rogalev, V. Gotte, C. Malgrange, C. Brouder and C. R. Natoli, *X-ray natural circular dichroism in a uniaxial gyrotropic single crystal of $LiIO_3$*, Journal of Chemical Physics **108(15)** (1998) 6394.

[27] G. Schütz, R. Wienke, W. Wilhelm, W. Wagner, P. Kienle, R. Zeller and R. Frahm, *Strong spin-dependent absorption at the $L_{2,3}$-edges of 5d-impurities in iron*, Zeitschrift für Physik B **75** (1989) 495.

[28] U. Fano, *Spin Orientation of Photoelectrons Ejected by Circularly Polarized Light*, Physical Review **178** (1969) 131.

[29] S. Flügge, Practical Quantum Mechanics (Springer Verlag, New York, 1974).

[30] S. Eisebitt, J. Lüning, W. F. Schlotter, M. Lörgen, O. Hellwig, W. Eberhardt and J. Stöhr, *Lensless imaging of magnetic nanostructures by X-ray spectro-holography*, Nature **432** (2004) 885.

[31] J. Hillier, *On microanalysis by electrons*, Physical Review **64** (1943) 318.

[32] J. Hillier and R. F. Baker, *Microanalysis by means of electrons*, Journal of Applied Physics **15** (1944) 663.

[33] P. A. Cherenkov, *Visible Emission of Clean Liquids by Action of γ Radiation*, Doklady Akad. Nauk SSSR **2** (1934) 451.

[34] M. Stöger-Pollach, H. Franco, P. Schattschneider, S. Lazar, B. Schaffer, W. Grogger and H. Zandbergen, *Čerenkov losses: A limit for bandgap determination and KramersKronig analysis*, Micron **37** (2006) 396.

[35] P. Schattschneider, Fundamentals of inelastic electron scattering (Springer Verlag, Vienna, 1986).

[36] R. F. Egerton, Electron energy-loss spectroscopy in the electron microscope, 2nd Ed. (Plenum press, New York, 1996).

[37] M. Varela, S. D. Findlay, A. R. Lupini, H. M. Christen, A. Y. Borisevich, N. Dellby, O. L. Krivanek, P. D. Nellist, M. P. Oxley, L. J. Allen and S. J. Pennycook, *Spectroscopic Imaging of Single Atoms Within a Bulk Solid*, Physical Review Letters **92** (2004) 095502.

[38] J. L. Lavergne, J. M. Martin and M. Belin, *Interactive electron energy-loss elemental mapping by the 'Imaging-Spectrum' method*, Microscopy Microanalysis Microstructures **3** (1992) 517.

[39] C. Jeanguillaume and C. Colliex, *Spectrum-image: The next step in EELS digital acquisition and processing*, Ultramicroscopy **28** (1989) 252.

[40] O. L. Krivanek, M. M. Disko, J. Taftøand J. C. H. Spence, *Electron Energy Loss Spectroscopy as a probe of the local atomic environment*, Ultramicroscopy **9** (1982) 249.

[41] J. Spence and J. Taftø, *Alchemi: a new technique for locating atoms in small crystals*, Journal of Microscopy **130(2)** (1983) 147.

[42] J. B. Goedkoop, B. T. Thole, G. vander Laan, G. A. Sawatzky, F. M. F. de Groot and J. C. Fuggle, *Calculation of magnetic X-ray dichroism in the 3d absorption spectra of rare-earth compounds*, Physical Review B **37** (1988) 2086.

[43] F. M. F. de Groot, *X-Ray absorption and dichroism of transition metals an their compounds*, Journal of electron spectroscopy and related phenomena **67** (1994) 529.

[44] C. Brouder, M. Alouani and K. H. Bennemann, *Multiple scattering theory of X-ray magnetic circular dichroism: implementation and results for the iron K edge*, Physical Review B **54** (1996) 7334.

[45] A. Ankudinov and J. J. Rehr, *Calculation of X-ray magnetic circular dichroism in Gd*, Physical Review B **52** (1995) 10214.

[46] M. Kucera, J. Kuneš, A. Kolomiets, M. Divis, A. V. Andreev, V. Sechovsky, J.-P. Kappler and A. Rogalev, *X-ray magnetic circular dichroism studies of 5f magnetism in UCoAl and UPtAl*, Physical Review B **66** (2002) 144405.

[47] J. Kuneš, P. M. Oppeneer, H.-C. Mertins, F. Schafers, A. Gaupp, W. Gudat and P. Novk, *X-ray Faraday effect at the $L_{2,3}$ edges of Fe, Co, and Ni: Theory and experiment*, Physical Review B **64** (2001) 174417.

[48] H.-C. Mertins, P. M. Oppeneer, J. Kunes, A. Gaupp, D. Abramsohn and F. Schafers, *Observation of the X-ray magneto-optical Voigt effect*, Physical Review Letters **87** (2001) 047401.

[49] P. Carra, B. T. Thole, M. Altarelli and X. Wang, *X-ray circular dichroism and local magnetic fields*, Physical Review Letters **70** (1993) 694.

[50] J. Stöhr, *Exploring the microscopic origin of magnetic anisotropies with X-ray magnetic circular dichroism (XMCD) spectroscopy*, Journal of Magnetism and Magnetic Materials **200** (1999) 470.

[51] M. Nelhiebel, P.-H. Louf, P. Schattschneider, P. Blaha, K. Schwarz and B. Jouffrey, *Theory of orientation sensitive near-edge fine structure core-level spectroscopy*, Physical Review B **59** (1999) 12807.

[52] M. Nelhiebel, Effects of crystal orientation and interferometry in electron energy loss spectroscopy, Ph.D. thesis, Ecole Centrale Paris, Châtenay-Malabry (1999).

[53] P. Schattschneider, C. Hébert, H. Franco and B. Jouffrey, *Anisotropic relativistic cross sections for inelastic electron scattering and the magic angle*, Physical Review B **72** (2005) 045142.

[54] H. Kohl and H. Rose, *Theory of Image Formation by inelastically scattered electrons in the electron microscope*, Advances in electronics and electron optics **65** (1985) 173.

[55] C. Hébert, P. Schattschneider, S. Rubino, P. Novák, J. Rusz and M. Stöger-Pollach, *Magnetic circular dichroism in electron energy loss spectrometry*, Ultramicroscopy doi:10.1016/j.ultramic.2007.07.011 **in print** (2007).

[56] C. Hébert Souche, P.-H. Louf, P. Blaha, M. Nelhiebel, J. Luitz, P. Schattschneider, K. Schwarz and B. Jouffrey, *The orientation dependent simulation of ELNES*, Ultramicroscopy **83** (2000) 9.

[57] R. D. Leapman, P. L. Fejes and J. Silcox, *Orientation dependance of core edges from anisotropic materials determined by inelastic scattering of fast electrons*, Physical Review B **28** (1983) 2361.

[58] C. Souche, B. Jouffrey, G. Hug and M. Nelhiebel, *Orientation sensitive EELS-analysis of boron nitride nanometric hollow spheres*, Micron **29** (1998) 419.

[59] K. Lie, R. Hier and R. Brydson, *Theoretical site- and symmetry-resolved density of states and experimental EELS near-edge spectra of AlB_2 and TiB_2*, Physical Review B **61** (2000) 1786.

[60] D. Su, C. Hébert, M. Willinger and R. Schlögl, *Anisotropy and collection angle dependence of the oxygen K ELNES in V_2O_5: a band-structure calculation study*, Micron **34** (2003) 227.

[61] J. Yuan and N. K. Menon, *Magnetic linear dichroism in electron energy loss spectroscopy*, Journal of Applied Physics **81** (1997) 5087.

[62] P. van Aken and S. Lauterbach, *Strong magnetic linear dichroism in Fe L_{23} and O K electron energy-loss near-edge spectra of antiferromagnetic hematite α-Fe_2O_3*, Physics and Chemistry of Minerals **30** (2003) 469.

[63] P. Schattschneider, M. Nelhiebel, H. Souchay and B. Jouffrey, *The physical significance of the mixed dynamic form factor*, Micron **31** (2000) 333.

[64] M. Nelhiebel, N. Luchier, P. Schorsch, P. Schattschneider and B. Jouffrey, *The mixed dynamic form factor for atomic core-level excitation in interferometric electron-energy-loss experiments*, Philosophical Magazine B **79** (1999) 941.

[65] P. Schattschneider, M. Nelhiebel and B. Jouffrey, *The density matrix of inelastically scattered fast electrons*, Physical Review B **59** (1999) 10959.

[66] P. Schattschneider, C. Hébert and B. Jouffrey, *Orientation dependence of ionization edges in EELS*, Ultramicroscopy **86** (2001) 343.

[67] M. Nelhiebel, P. Schattschneider and B. Jouffrey, *Observation of Ionization in a crystal interferometer*, Physical Review Letters **85** (2000) 1847.

[68] P. Schattschneider and B. Jouffrey, *Channeling, localisation and the density matrix in inelastic electron scattering*, Ultramicroscopy **96** (2003) 453.

[69] H. Kohl, *A simple procedure for evaluating effective scattering cross-sections in stem*, Ultramicroscopy **16** (1985) 265.

[70] S. Rubino, P. Schattschneider, M. Stöger-Pollach, C. Hébert, J. Rusz, L. Calmels, B. Warot-Fonrose, F. Houdellier, V. Serin and P. Novák, *EMCD: Magnetic Chiral Dichroism in the Electron Microscope*, Journal of Materials Research **submitted**.

[71] A. J. F. Metherell, *Diffraction of electrons by perfect crystals*, in *Electron Microscopy in Materials Science vol. II*, edited by U. Valdré and E. Ruedl (Commission of the European Communities, Luxembourg, 1975) 397–552.

[72] L.-M. Peng and M. J. Whelan, Proc. R. Soc. London Ser. A **431** (1990) 111.

[73] A. Weickenmeier and H. Kohl, Acta Cryst. A **47** (1991) 590.

[74] P. A. Doyle and P. S. Turner, Acta Cryst. A **24** (1968) 390.

[75] P. Blaha, K. Schwarz, G. Madsen, D. Kvasicka and J. Luitz, WIEN2k, An Augmented Plane Wave + Local Orbital Program for Calculating Crystal Properties (Karlheinz Schwarz, Techn. Universität Wien, Austria, 2001).

[76] A. L. Lewis, R. E. Villagrana and A. J. F. Metherell, Acta Cryst. A **34** (1978) 138.

[77] Y. Kainuma, Acta Cryst. **8** (1955) 247.

[78] P. Schattschneider and W. S. M. Werner, *Coherence in electron Energy Loss Spectrometry*, J. Electron Spectrosc. rel. Phenom. **143** (2005) 83.

[79] J. Kuneš, P. Novák, R. Schmid, P. Blaha and K. Schwarz, *Electronic structure of fcc Th: Spin-orbit calculation with* $6p_{1/2}$ *local orbital extension*, Physical Review B **64** (2001) 153102.

[80] D. J. Singh, Plane waves, pseudopotentials and the LAPW method (Kluwer Academic Publishers, London, 1994).

[81] P. Hohenberg and W. Kohn, *Inhomogeneous Electron Gas*, Physical Review **136** (1964) B864.

[82] W. Kohn and L. J. Sham, *Self-Consistent Equations Including Exchange and Correlation Effects*, Physical Review **140** (1965) A1133.

[83] J. P. Perdew and Y. Wang, *Accurate and simple analytic representation of the electron-gas correlation energy*, Physical Review B **45** (1992) 13244.

[84] F. de Groot, Coord. Chem. Rev. **249** (2005) 31.

[85] A. P. Hitchcock, *Near Edge Electron Energy Loss Spectroscopy: Comparison to X-ray Absorption*, Jpn. J. Appl. Phys. **32(2)** (1993) 176.

[86] J. Kuneš and P. M. Oppeneer, Physical Review B **67** (2003) 024431.

[87] J. Rusz, P. Novák, S. Rubino, C. Hébert and P. Schattschneider, *Magnetic circular dichroism in electron microscopy*, Acta Physica Polonica B **in print** (2007).

[88] J. Verbeeck, C. Hébert, P. Schattschneider, S. Rubino, P. Novák, J. Rusz, F. Houdellier and C. Gatel, *Optimizing signal to noise ratio in EMCD experiments*, Ultramicroscopy **submitted**.

[89] M. Tanaka, R. Saito, K. Ueno and Y. Harada, *Large-Angle Convergent-Beam Electron Diffraction*, Journal of Electron Microscopy **29** (1980) 408.

[90] P. A. Midgley, *A simple new method to obtain high angular resolution ω-q patterns*, Ultramicroscopy **79** (1999) 91.

[91] P. Schattschneider, C. Hébert, S. Rubino, M. Stöger-Pollach, J. Rusz and P. Novák, *Magnetic circular dichroism in EELS: Towards 10 nm resolution*, Ultramicroscopy doi:10.1016/j.ultramic.2007.07.002 **in print** (2007).

[92] A. Rose, *A unified approach to the performance of photographic film, television pickup tubes and the human eye*, J. Soc. Motion Pict. Eng. **47** (1946) 273.

[93] P. Schattschneider, M. Stöger-Pollach, S. Rubino, M. Sperl, C. Hurm, J. Zweck and J. Rusz, *Pushing the detection limit of Magnetic Circular Dichroism to 2 nm* **submitted**.

[94] B. Warot-Fonrose, F. Houdellier, M. J. Hÿtch, L. Calmels, V. Serin and E. Snoeck, *Mapping inelastic intensities in diffraction patterns of magnetic samples using the energy spectrum imaging technique*, Ultramicroscopy doi 10:1016/j.ultramic.2007.05.013 **in print** (2007).

[95] J. Hejtmánek, E. Pollert, Z. Jirák, D. Sedmidubský, A. Strejc, A. Maignan, C. Martin, V. Hardy, R. Kužel and Y. Tomioka, *Magnetism and transport in Pr1-xSrxMnO3 single crystals (0.48¡x¡0.57)*, Physical Review B **66** (2002) 014426.

[96] J. Rusz, O. Eriksson, P. Novák and P. M. Oppeneer, *Sum-rules for electron energy-loss near-edge spectra*, Physical Review B **76** (2007) 060408(R).

[97] L. Calmels, F. Houdellier, B. Warot-Fonrose, C. Gatel, M. J. Hÿtch, V. Serin, E. Snoeck and P. Schattschneider, *Experimental application of*

sum rules for electron energy loss magnetic chiral dichroism, Physical Review B **76** (2007) 060409(R).

[98] M. B. Stearns, *Landolt-Börnstein Numerical Data and Functional Relationships in Science and Technology, Group 3, Vol. 19, Pt. a* (Springer-Verlag, Berlin, 1986) .

[99] D. Bonnenberg, K. A. Hempel and H. P. J. Wijn, in *Magnetic Properties of 3d, 4d and 5d Elements, Alloys and Compounds Vol. III/19a, p. 178*, edited by K.-H. Hellwege and O. Madelung , Landolt-Börnstein, New Series (Springer-Verlag, Berlin, 1986) .

[100] C. Kittel, Introduction to solid state physics, 3rd edition (John Wiley and sons, New York, 1966).

[101] P. Gambardella, A. Dallmeyer, K. Maiti, M. C. Malagoli, W. Eberhardt, K. Kern and C. Carbone, *Ferromagnetism in one-dimensional monatomic metal chains*, Nature (2002) 301.

[102] C. Hurm, M. Stöger-Pollach, S. Rubino, C. Hébert, P. Schattschneider and J. Zweck, *In-situ magnetisation reversal in a Tecnai TEM for EMCD experiments* **in preparation**.

[103] J. L. Erskine and E. A. Stern, *Calculation of the M_{23} magneto-optical absorption spectrum of ferromagnetic nickel*, Physical Review B **12(11)** (1975) 5016.